

American Journal of Science

DECEMBER 2014

HEMATITE AND Mn OXIDE (U-Th)/He DATES FROM THE BUCKSKIN-RAWHIDE DETACHMENT SYSTEM, WESTERN ARIZONA: GAINING INSIGHTS INTO HEMATITE (U-Th)/He SYSTEMATICS

NATHAN S. EVENSON*, PETER W. REINERS^{*,†}, JON E. SPENCER^{**}, and DAVID L. SHUSTER^{***,§}

ABSTRACT. In this paper, we use several analytical methods in an effort to better understand the systematics of the (U-Th)/He chronometer in hematite and manganese oxides. ^4He diffusion data from a polycrystalline hematite sample is consistent with diffusion from hematite crystals with a range of sizes similar to those directly observed in sample material. Combined with a compilation of hematite He diffusion data from previous studies, this supports the interpretation that in general crystal size is a primary control on He retentivity in hematite. $^4\text{He}/^3\text{He}$ diffusion data from a single fragment of a larger hematite crystal imply the presence of multiple diffusion domains smaller than the observed size of the crystal fragment, which may be related to cracks, inclusions, or other internal features, as well as higher concentrations of ^4He in smaller domains. We use kinetic values determined in this and other studies and measurements of hematite crystal size in each dated sample to estimate approximate closure temperatures for each sample, most of which range from 140 to 240 °C. Relationships between minor element and parent nuclide concentrations and (U-Th)/He dates measured in aliquots of some analyzed hematite samples suggest that, in some cases, U and Th are concentrated in interstitial phases other than hematite. We identify two processes responsible for much of the dispersion in hematite dates from single samples. Removal of U- and Th-rich interstitial phases from analyzed material during sample preparation or analysis leaves behind unsupported ^4He implanted in hematite crystals. This removal results in apparent (U-Th)/He dates artificially older than the time of hematite He closure. A smaller source of dispersion that is likely to still be significant in some samples can be attributed to the high He diffusivities of observed interstitial phases, which do not retain implanted He. (U-Th)/He dating of hematite from upper and lower-plate rocks in the Buckskin and Rawhide detachment fault system of western Arizona yields ages that coincide with the timing of rapid extension along the detachment fault. Comparisons of estimated hematite closure temperatures and hematite sample ages to data from other studies of the Buckskin-Rawhide detachment system lead us to conclude that hematite dates record rapid cooling that followed detachment zone mineralization. Mn oxide (U-Th)/He dates are interpreted as formation ages of minerals formed by hydrothermal fluids that circulated through upper-plate rocks after cessation of extension along the detachment fault. Overall, we find that (U-Th)/He dating of hematite and Mn oxide minerals are promising methods for obtaining temporal information about the formation and cooling of these common secondary phases.

* Department of Geosciences, University of Arizona, 1040 E. 4th Street, Tucson, Arizona 85721, USA

** Arizona Geological Survey, 416 W. Congress Street, Suite 100, Tucson, Arizona 85701, USA

*** Department of Earth and Planetary Science, University of California-Berkeley, 307 McCone Hall, Berkeley, California 94720, USA

§ Also at: Berkeley Geochronology Center, 2455 Ridge Road, Berkeley, California 94709, USA

† Corresponding author: Peter Reiners (reiners@email.arizona.edu, tel. 520-621-6000).

Keywords: (U-Th)/He dating, He diffusion, hematite, manganese oxide, Buckskin-Rawhide Mountains, detachment-related mineralization

INTRODUCTION

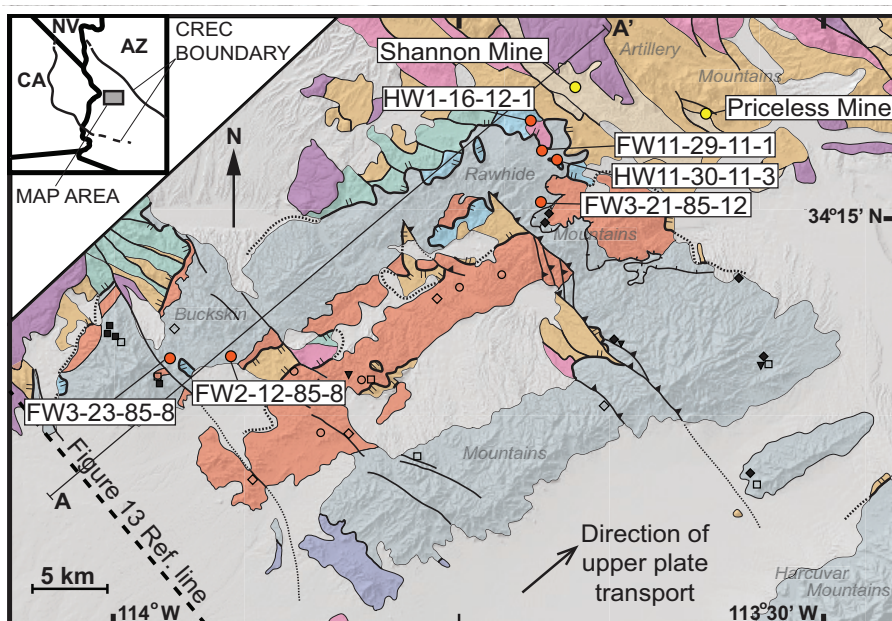
The ability to use radioisotopic dating to quantify the formation or thermal history of hematite holds potential for a number of applications. Hematite is a common primary mineral in sedimentary iron deposits and iron oxide-copper-gold (IOCG) deposits (Hitzman and others, 1992; Barton and Johnson, 1996). Samples from such deposits have been the target of previous (U-Th)/He dating efforts (Wernicke and Lippolt, 1997a, 1997b). Secondary hematite is also ubiquitous in veins, faults, and fractures in bedrock. Dating these deposits could provide information about the timing of fluid flow and structure formation/activity (Ault and others, 2013).

Several studies have used the (U-Th)/He method to obtain dates from hematite. The first geologically reasonable hematite (U-Th)/He date was obtained by Strutt (1908). Wernicke, Lippolt, and others published several studies with dates from samples of pure specular and botryoidal hematite that were reproducible and consistent with other geologic evidence (Wernicke and Lippolt, 1993; Wernicke and Lippolt, 1994a, 1994b; Lippolt and others, 1995; Wernicke and Lippolt, 1997a, 1997b). Others have used hematite (U-Th)/He dates to estimate the timing of weathering processes (Pidgeon and others, 2004). Most recently, Farley and Flowers (2012) used $^4\text{He}/^3\text{He}$ experiments to quantify parameters of helium diffusion in a polycrystalline hematite sample. Combined with (U-Th)/Ne dates on the same sample, they used these data to infer both formation age and thermal history of the sample.

$^{40}\text{Ar}/^{39}\text{Ar}$ chronometry of Mn oxide minerals has been widely applied in studies of low-temperature processes such as weathering (Vasconcelos and others, 1992; Vasconcelos, 1999; Hautmann and Lippolt, 2000; Dill and others, 2010; Waltenberg, *ms*, 2012), but Mn oxide (U-Th)/He chronometry has received much less attention in published studies. Lippolt and Hautmann (1995) and Reiners and others (2014) performed ^4He diffusion experiments on cryptomelane-hollandite, the results of which suggest that these phases can retain large fractions of their radiogenic He in at least some cases. Development of (U-Th)/He chronometry in Mn oxides that commonly occur in supergene environments (Vasconcelos, 1999) will provide another radioisotopic method that may enhance the understanding of results from the $^{40}\text{Ar}/^{39}\text{Ar}$ dating of Mn oxides and (U-Th)/He dating of goethite (Shuster and others, 2005; Heim and others, 2006; Yapp and Shuster, 2011; Danišik and others, 2013; and Vasconcelos and others, 2013).

The Buckskin-Rawhide detachment system of western Arizona, which is part of the Colorado River extensional corridor (Howard and John, 1987), was active during late Oligocene to Miocene time (Spencer and others, 1995). During this period of extension, a large area of mylonitic rocks in the footwall of the detachment system was tectonically exhumed from depths of 12 to 15 km, and is now exposed at the surface in the Buckskin and Rawhide Mountains (fig. 1; Spencer and Reynolds, 1989). Hematite is abundant in the voluminous Fe, Cu, Au, and Mn-bearing mineral deposits in upper- and lower-plate rocks of the Buckskin-Rawhide detachment system (Spencer and Welty, 1986, 1989).

In this study, we combine data from our own hematite He diffusion experiments with those of previous studies in an effort to estimate the kinetic parameters that control this process. Using minor- and trace-element chemistry of dated samples, we also gain insights into the effects that aliquot pre-treatments (for example, ultrasonic cleaning) and He extraction techniques may have on hematite (U-Th)/He dates. We consider potential sources of dispersion in the dates that we obtain, concluding that most scatter is the result of parent nuclide loss during sample pre-treatment or analysis, or diffusive loss of radiogenic ^4He from phases other than hematite present in analyzed



MAP UNITS

Upper plate and post-detachment units

- Surficial deposits (Late Cenozoic)
- Volcanic rocks (middle-late Miocene)
- Conglomerate and sandstone, including Sandtrap Wash Conglomerate (middle-late Miocene)
- Sedimentary and volcanic rocks, including Artillery and Chapin Wash Formations and equivalents (Oligocene-middle Miocene)
- Metavolcanic and metasedimentary rocks (Mesozoic)
- Metasedimentary rocks (Paleozoic)
- Crystalline rocks (Proterozoic)

Lower plate units

- Mylonitic crystalline rocks of the Swansea Plutonic Suite
- Mylonitic metasedimentary rocks (Mesozoic and Paleozoic)
- Mylonitic crystalline rocks (Proterozoic)

MAP SYMBOLS

Sample locations

- Hematite (U-Th)/He, this study
- Mn oxide (U-Th)/He, this study
- Apatite (U-Th)/He, Brady (2002)
- ◇ Apatite FT, Foster and others (1993)
- ◆ Zircon FT, Bryant and others (1991)
- ▼ Biotite K-Ar, Spencer and others (1989) Bryant (1995)
- Biotite Ar-Ar, Scott and others (1998)
- K-feldspar Ar-Ar, Richard and others (1990)

Structural features

- ~ Buckskin-Rawhide detachment fault
- ~ Low angle normal fault in lower plate
- ~ Normal fault
- ~ Thrust or reverse fault
- ~ Concealed fault trace

Fig. 1. Map of study area, with key to symbols and unit colors. Inset map in upper left portion of the figure shows location of study area within the Colorado River extensional corridor. Dates from the samples shown in this map are plotted against distance in direction of upper-plate transport from the dashed bold line in figure 13. A-A': Approximate location of schematic cross sections shown in figures 13 and 14, parallel to direction of upper-plate transport. Map modified from Spencer and Reynolds (1991), Bryant (1995), and Scott and others (1998).

sample material. Accounting for the effects of these processes, hematite and Mn oxide sample dates are consistent with rapid cooling of samples following mineralization.

GEOLOGIC SETTING

The Buckskin-Rawhide detachment fault is one of six major extensional faults of the Colorado River extensional corridor that were active during late Oligocene-Miocene time (Howard and John, 1987; Scott and others, 1998; Foster and John, 1999). The Buckskin-Rawhide detachment system is host to voluminous Fe-Cu oxide mineral deposits and sedimentary Mn oxide deposits (Lasky and Webber, 1944, 1949; Spencer and Welty, 1986, 1989; Spencer, 1991). A number of previous studies suggest that footwall rocks exposed in the Buckskin and Rawhide Mountains were rapidly cooled during Miocene extension, and were not reheated by burial or other heat sources (Bryant and others, 1991; Foster and others, 1993; Scott and others, 1998; Brady, 2002). This simple thermal history, combined with widespread occurrence of suitable sample material, makes the Buckskin-Rawhide detachment system an ideal locality in which to test hematite and Mn oxide (U-Th)/He dating.

Lower Plate Rocks

Rocks of Proterozoic to Oligocene-Miocene age compose the lower-plate of the Buckskin-Rawhide detachment fault. Proterozoic crystalline rocks, which display mylonitic fabrics in most localities, make up most exposures of the lower-plate (Bryant, 1995; Bryant and Wooden, 2008). The Swansea Plutonic Suite (SPS) makes up much of the remainder of lower-plate exposures (fig. 1). U-Pb LA-ICPMS analysis of zircon from two samples of SPS granodiorite yields Miocene age populations, with mean dates of 21.5 and 21.3 Ma, which are interpreted as the crystallization age of this unit (Singleton and Mosher, 2012). $^{40}\text{Ar}/^{39}\text{Ar}$ analyses of hornblende from mafic intrusions that compose a small fraction of the exposures of the SPS yield cooling dates of 30 to 26 Ma (Richard and others, 1990; Scott and others, 1998). These dates may be affected by excess argon (Bryant and Wooden, 2008).

$^{40}\text{Ar}/^{39}\text{Ar}$, fission-track, and (U-Th)/He thermochronology show that the footwall of the Buckskin-Rawhide detachment fault underwent rapid exhumation and cooling beginning at ~ 20 Ma. K-feldspar $^{40}\text{Ar}/^{39}\text{Ar}$ step-heating analyses from the western Buckskin Mountains reflect an increase in cooling rates experienced by lower-plate rocks in the Buckskin-Rawhide detachment system at 20 to 19 Ma (Scott and others, 1998). Dates from thermochronometers with lower closure temperatures range from 18 to 10 Ma (Spencer and others, 1989a; Bryant and others, 1991; Foster and others, 1993; Brady, 2002). Scott and others (1998) review these data and reach the conclusion that footwall rocks were cooled from temperatures of ~ 350 °C to near-surface temperatures at rates of 80 to 280 °C/Myr, beginning at ~ 20 Ma in the western Buckskin Mountains, and at younger dates to the northeast. In several studies that utilize a single thermochronometer, dates from lower-plate rocks exposed in the southwest part of the field area are older than dates from samples to the northeast (Foster and others, 1993; Scott and others, 1998; Brady, 2002). This pattern reflects progressive, SW to NE exhumation of the footwall during top-to-the-northeast extension.

Upper Plate Rocks

Upper-plate rocks in the Buckskin-Rawhide detachment system consist primarily of Mesozoic sedimentary and volcanic rocks, though isolated exposures of Proterozoic-Mesozoic sedimentary and crystalline rocks are also observed (fig. 1).

The oldest Cenozoic unit is the Oligocene-Miocene Artillery Formation, (Spencer and others, 1989b; Yarnold, 1994). A tuff near the base of this unit exposed near the area shown in figure 1 is dated to 26.28 ± 0.01 Ma (sanidine $^{40}\text{Ar}/^{39}\text{Ar}$, Spencer and

others, 2013). This date is the oldest obtained from syn-extensional strata in the Buckskin-Rawhide detachment system. We consider it the maximum reasonable initiation age for detachment activity and the formation of related mineral deposits. The minimum age of Artillery Formation deposition is not as well-understood. K-Ar dates on basalts interbedded with breccia layers thought to be upper Artillery-equivalent range from ~20 to 18.5 Ma (Wilkins and Hedrick, 1982; Spencer and others 1989a). A younger 16.2 Ma $^{40}\text{K}/^{39}\text{Ar}$ date was obtained on a basaltic flow in the upper Artillery Formation northeast of the study area (Shackelford, 1980).

The Chapin Wash Formation, a sequence of mostly clastic sedimentary rocks, overlies Artillery-equivalent deposits throughout much of the study area (Lasky and Webber, 1949; Yarnold, 1994; Spencer and other, 2013). In contrast to the Artillery Formation, the presence of sparse mylonitic clasts in coarse-grained parts of the upper Chapin Wash Formation implies exposure of footwall rocks at the surface during Chapin Wash Formation time (Spencer and Reynolds, 1989). The maximum depositional age of the Chapin Wash Formation is poorly defined—as noted above, volcanic rocks in the underlying upper Artillery Formation are as young as 16.2 Ma (Shackelford, 1980). These constraints imply that the lower-plate of the detachment fault was exposed at the surface after ~16 Ma.

The youngest Cenozoic sedimentary and volcanic strata in the study area record cessation of activity on the Buckskin-Rawhide detachment system by ~9 to 8 Ma. Abundant mylonitic debris within the Sandtrap Conglomerate, which caps the Miocene section in and northeast of the Rawhide Mountains, is thought to be derived from widespread local exposures of footwall rocks (Spencer and Reynolds, 1989). In the Artillery Mountains, the upper portions of the Sandtrap Conglomerate are gently dipping (Spencer and others, 1989b; Spencer and others, 2013). This unit is interbedded with gently tilted flows of the Manganese Mesa Basalt (Spencer and others, 2013). Whole rock K-Ar analyses of this basalt yield dates of 9.6 to 9.5 Ma (Shafiqullah and others, 1980; Shackelford, 1980), a date similar to the 11 to 10 Ma K-Ar dates obtained on flat-lying basalts that lie near the top of the Tertiary stratigraphy throughout the Buckskin Mountains (Spencer and others, 1989a). These dates suggest that tilting related to activity on the detachment ended by ~10 Ma in the Buckskin Mountains, but persisted until shortly after 9 to 8 Ma in the eastern Rawhide Mountains and Artillery Mountains.

Ore Deposits

Alteration and mineralization in lower-plate rocks occurred in multiple stages. Upper plate rocks in the Buckskin-Rawhide detachment system and surrounding areas, particularly Cenozoic volcanic rocks, display the effects of pervasive K-metasomatism (Roddy and others, 1988; Spencer and others, 1989a; Beratan, 1999). This metasomatism occurred as meteoric fluids were drawn deeper into the detachment zone, and it produced metal-rich brines thought to be the parent fluids of detachment-related mineral deposits (Hollocher and others, 1994; Michalski and others, 2007). Alteration and mineralization of lower-plate rocks throughout the Buckskin-Rawhide detachment system followed a sequence that typically began with chloritization of brecciated lower-plate rocks in and below the detachment zone (accompanied in some localities by Cu- and Fe-sulfide mineralization; Spencer and Welty, 1986, 1989; Halfkenny and others, 1989). Following this, Cu- and Fe-sulfides were replaced, or reduced in abundance, in an oxidizing fluid environment that also produced a large volume of hematite and a lesser amount of quartz. Minerals that follow hematite mineralization vary between localities; chlorite, chrysocolla, and calcite are common, while barite, amorphous silica, and various Cu-carbonates are variably abundant (Lehmann and Spencer, 1989; Spencer and Welty, 1989). Homogenization temperatures from fluid inclusions in footwall and detachment zone samples in the western Buckskin moun-

tains suggest that quartz formed from high-salinity fluids (12–22 wt% NaCl-equivalent) at temperatures greater than 225 to 325 °C (Wilkins and others, 1986).

Deposits of Fe-Cu oxide minerals in upper-plate rocks were likely precipitated from the same saline fluids that are inferred to be the parent fluids of footwall and detachment-zone deposits. Large deposits of Fe and Cu oxides hosted in brittle faults within Paleozoic-Neogene upper-plate rocks display similar mineral assemblages and fluid-inclusion-homogenization temperatures to footwall and detachment-zone deposits (Spencer and Welty, 1986, 1989; Wilkins and others, 1986).

Mn oxide minerals are abundant in Miocene sedimentary rocks. The Chapin Wash Formation contains zones rich in Mn oxide, which is present as both detrital particles and cement (Lasky and Webber, 1944, 1949; Spencer and others, 1989b; Spencer, 1991; Derby, ms, 2012). More-concentrated deposits of Mn oxide are present as veins and fracture fillings that cross-cut the Chapin Wash Formation and Sandtrap Conglomerate (Spencer and others, 1989b; Spencer, 1991). Mn oxide samples examined in this study are taken from this latter type of deposit. The genesis of vein-type deposits is uncertain. Some veins may be a result of the emplacement of Miocene volcanic flows, which drove the circulation of surface-derived fluids that dissolved stratiform Mn and redeposited it in other settings (Derby, ms, 2012). Alternatively, Mn in these deposits may have been mobilized from upper-plate rocks during K-metasomatism and transported through deeper parts of the detachment zone prior to deposition at shallow depths (Spencer and Welty, 1986).

METHODS

(U-Th)/He Aliquot Selection and Pre-Treatment

Ultrasonic cleaning treatment.—We used ultrasonic cleaning to disaggregate sample material and separate hematite crystals from other phases present in many hematite samples (table 1) in an attempt to minimize the amount of non-hematite material in some analyzed aliquots. All hematite aliquots were selected from material prepared by removing centimeter-scale fragments of hematite-rich material from hand samples and crushing these fragments on a clean surface. Splits of crushed material were placed in clean vials filled with ultrapure water, and subjected to ultrasonic cleaning for 4.5 minutes at room temperature (20 °C). ICPMS analyses of ultrapure water from vials to which no sample material was added prior to ultrasonic treatment (“cleaning blanks”) contained no measurable U or Th, which indicates that the cleaning process does not add U or Th to cleaned sample material. Immediately after ultrasonic treatment, vials containing cleaned sample material were flushed with additional ultrapure water, removing most suspended particles of sample material. Cleaned and not cleaned splits of sample material were placed into clean sample storage dishes, and cleaned samples were allowed to dry. A high-power optical microscope was used to identify aliquots for analysis. To allow for laser heating, selected aliquots were placed in ethanol and packed into Nb tubes (tube dimensions: 1 mm long, 0.68 mm outer diameter, walls 0.07 mm thick).

Aliquot selection.—We used aliquot-selection techniques to minimize the amount of phases other than hematite that were included in some hematite aliquots. In hematite samples comprising aggregates of plate-shaped hematite crystals and other phases (herein called “plate aggregate” samples, including all hematite samples except FW2-12-85-8, fig. 2), two types of aliquot were selected. ‘Plate-only’ (PO) aliquots consisted of what appeared to be fragments of single, plate-shaped hematite crystals with little other material visible on their surfaces. In samples where no single crystal or crystal fragment would provide a sufficient amount of material for analysis, five to fifteen relatively clean, loose plate fragments were combined into a single PO aliquot. ‘Aggregate’ aliquots consisted of polycrystalline material that had not been broken up

TABLE 1
Descriptions of field setting, hematite crystal size and morphology, and interstitial phase assemblage and texture of hematite samples

Sample	FW2-12-85-8	FW3-23-85-8	FW3-21-85-12	FW11-29-11-1	HW1-16-12-1	HW11-30-11-3
Setting	Mylonitic rocks in the lower plate, western Buckskin mountains	Mylonitic rocks in the lower plate, western Buckskin mountains	Mylonitic rocks in the lower plate, Rawhide Mountains	Mylonitic rocks in the lower plate, Rawhide Mountains	Metamorphosed Paleozoic carbonate rocks in upper plate, <200 m above main detachment	Metamorphosed Paleozoic carbonate rocks in upper plate, ~1 m above main detachment
Hematite description	Euhedral, rhombohedral crystals, most 1-2 mm in diameter. Few inclusions present in crystals, little other internal structure observed (fig. 2A).	Plate-shaped crystals 1-120 µm in thickness (fig. 2B). Most crystals display through-going cracks every 500-800 µm along length.	Plate-shaped crystals 0.5-30 µm in thickness. Crystals densely packed. Few cracks in crystals (fig. 2C).	Plate-shaped crystals 1-30 µm in thickness. Void spaces visible between tightly-packed bundles of crystals (fig. 2D).	Plate-shaped crystals ~1-60 µm thick, most 1-30 µm thick. Packing of hematite crystals more open in this sample than in FW samples (fig. 2E).	Plate shaped crystals 0.5-80 µm thick. Larger masses of hematite have complex internal structure, may be multiple crystals (fig. 2F).
Other phases	Few inclusions of chl, ap, qtz. Minor chl on some crystal faces.	Few small ap inclusions. Interstitial phases mostly chy, some chl, minor ap. Chy appears to grow around other phases (fig. 2B, fig. A1).	Aps as large as 100 µm in diameter present as inclusions (fig. A2A,E), hem also appears to grow around aps. Chl is most voluminous interstitial phase, chy also present (fig. A2).	Euhedral qtz crystals present as inclusion in hem. Minor chl on some crystal faces. Among plate aggregate hem samples, this sample contains smallest volume of non-hem phase (fig. 2D)	Small aps and blocky, sub-to euhedral qtz crystals occur as inclusions. Hem appears to grow around blocky qtz. Cal and chl are dominant interstitial phases, chy absent (fig. 2E).	Chl and amorphous silica-qtz are main interstitial phases. Zones of microcrystalline Fe oxide are observed, and contain fragments of platy hematite crystals (fig. 2F).

Mineral abbreviations: hem = hematite, ap = apatite, chl = chlorite, chy = chrysocolla, cal = calcite, qtz = quartz.

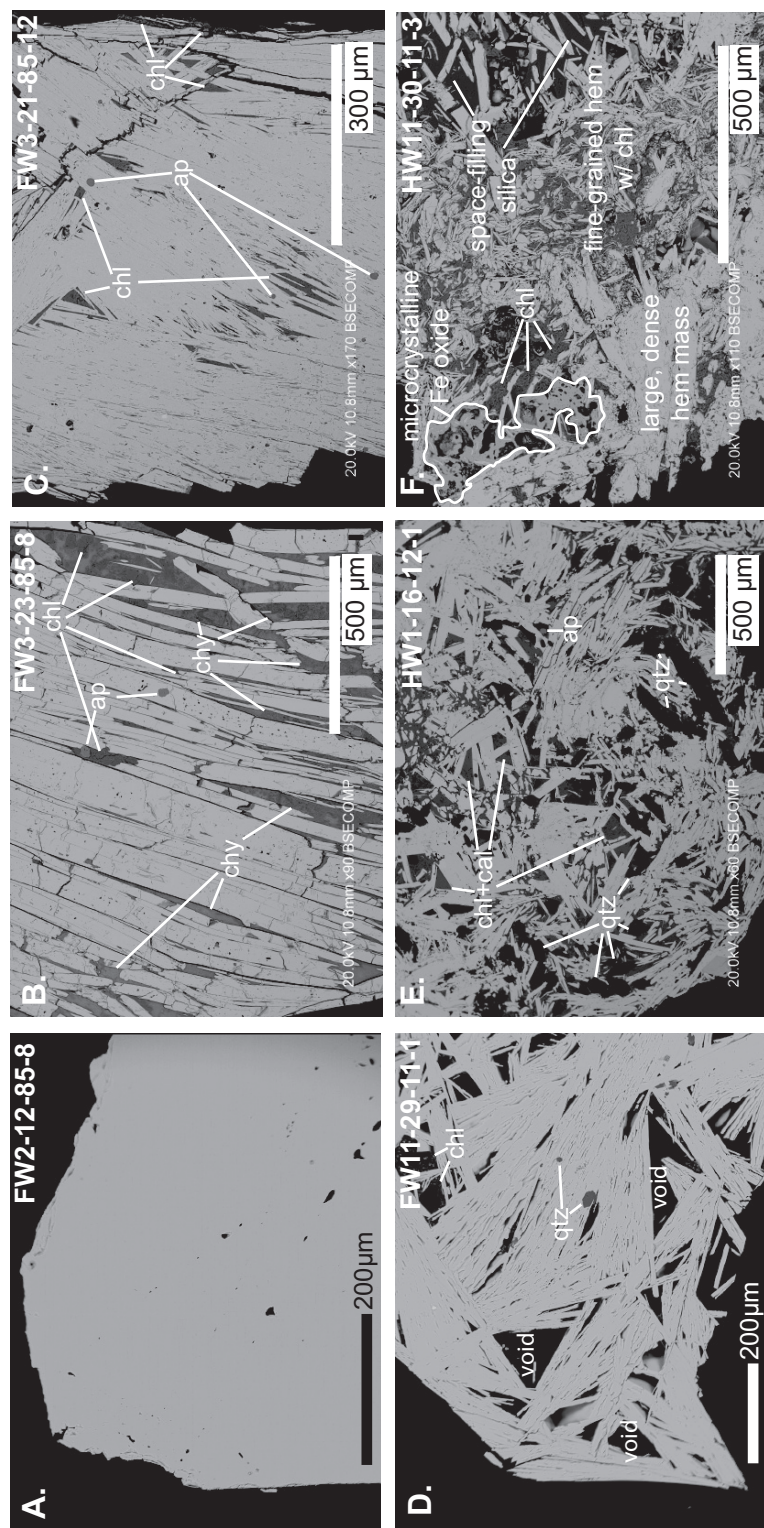


Fig. 2. Representative back-scattered electron images of hematite samples. Hematite crystals appear lighter than other phases, and are unlabeled. Apatite (ap), calcite (cal), chlorite (chl), chrysocolla (chy), and quartz (qtz), and other phases are labeled. These images are representative of the material in aliquots analyzed in this study, though we made an effort to select aliquots with minimal amounts of non-hematite phases. (A) FW2-12-85-8: Part of a single, euhedral crystal of hematite with small inclusions. (B) FW3-23-85-8: U-rich chy fills space around hematite, ap and chl crystals. Note that gaps between plates in this sample are larger than those observed in other samples. See figure A1. (C) FW3-21-85-12: Chl fills open space between hematite crystals; anhedral ap crystals are present as inclusions. Chy and cal also present in this sample, see figure A2. (D) FW11-29-11-1: Hematite crystals appear to grow around euhedral qtz crystals. Spaces between hematite crystals remain largely unfilled. (E) HW1-16-12-1: Hematite crystals appear to grow around large, blocky, subhedral-euhedral qtz crystals. Hematite and qtz are surrounded by a space-filling mixture of cal and chl. (F) HW11-30-11-3: Platy hematite crystals in this sample vary widely in size. Texture of iron oxide crystals in this sample is also somewhat varied: note the larger dense masses and fine-grained crystals labeled on image. Area outlined in white is microcrystalline Fe oxide phase, present in pockets throughout the sample.

during sample crushing and/or ultrasonic cleaning, and that therefore are likely to contain a larger volume fraction of non-hematite phases.

Mn oxide aliquots analyzed in this study were aggregates of microcrystalline material that had not been ultrasonically cleaned. Selected aliquots were packed into Nb tubes in the same manner as hematite aliquots.

We determined parent nuclide and minor/trace-element concentrations in undegassed aliquots of hematite and Mn oxide samples to control for the effects of heating aliquots to high temperatures during He extraction. Undegassed aliquots were selected from the same pool of aliquot material as dated aliquots. All undegassed aliquots were aggregate aliquots. These aliquots were packed into Nb tubes, but were not subjected to He extraction (described below) prior to dissolution.

We also analyzed aliquots of chrysocolla taken from crushed hematite sample material to provide a direct measure of the U and Th contents of this phase. Aliquots of chrysocolla were selected from cleaned and not cleaned splits of sample FW3-23-85-8. These aliquots were not extracted for He prior to dissolution.

Acid leaching.—Four aggregate (polycrystalline) aliquots of sample FW3-21-85-12 were leached in a pH 3 nitric acid solution in an attempt to remove or reduce the amount of U that may be adsorbed to the surface of hematite crystals. Two of these aliquots were packed in Nb tubes, the other two were not. Aliquots were placed into 4 mL Teflon vials that had been cleaned in aqua regia. Two mL of pH 3 HNO₃ prepared from a stock solution of concentrated ultrapure HNO₃ and ultrapure water were added to each vial. The vials were left undisturbed for one hour. After this rest period, the vials were swirled to homogenize the acid solution, and 1.5 mL of the leaching solution was transferred to a clean Teflon vial. The removed solution was replaced by 2 mL of fresh pH 3 solution. After this addition, the vials were left undisturbed for 72 hours. At the end of this 72-hour period, the vials were swirled, and 1.5 mL of solution was again transferred to an empty, clean Teflon vial. The remaining solution and the aliquot were flushed from the vial with 15 to 20 mL of ultrapure water. Aliquots were placed in ethanol, and, if not leached in an Nb tube, packed into one. The (U-Th)/He dates and chemical compositions of leached aliquots were determined using procedures described below. The pH values of the fractions of leaching solution removed from vials during the leaching process were adjusted by addition of ultrapure nitric acid solution. These solutions were then spiked with a ²³³U-²²⁹Th solution and analyzed for Th and U contents using an Element 2 ICPMS.

(U-Th)/He Analysis

⁴He extraction and measurement.—The ⁴He measurement process employed in this study is similar to the process described for zircon (U-Th)/He dating by Reiners (2005). Aliquots in Nb tubes were loaded into a UHV gas extraction line and heated to temperatures of 1000 to 1150 °C (temperatures estimated using a pyrometer) for 14 to 18 minutes using a Nd-YAG or diode laser. After this initial extraction, cryopurification of the evolved gas, and measurement of the abundance of ⁴He relative to a ³He spike by quadrupole mass spectrometry, each aliquot was subjected to a second laser heating period of equal or slightly greater duration than the first. Additional heating periods were performed until the ⁴He yield of the final heating was <1 percent of the total ⁴He yield. Analysis of a known quantity of ⁴He was performed after every 4 to 5 unknown analyses to monitor instrumental sensitivity drift.

Step heating experiments.—A ⁴He step heating experiment was performed on an aggregate of hematite crystals from sample FW11-29-11-1. The sample was held isothermally at temperatures of 145 to 486 °C for time periods of 60 to 1020 minutes using a projector bulb heating apparatus (Farley and others, 1999). Gas evolved during each heating step was measured in a process identical to that described in the previous paragraph. Multiple cycles of pro- and retrograde temperature steps were used, though

low gas yields prevented the use of temperatures below 300 °C during the second half of the experiment. Following step heating, the remaining ^4He was extracted from the sample in a manner similar to that described for aliquots that were subjected to bulk age analysis.

An aliquot of sample FW2-12-85-8 was analyzed in a $^4\text{He}/^3\text{He}$ experiment. An internal chip of a single large crystal from sample FW2-12-85-8 was irradiated with a beam of ~ 220 MeV protons at the Francis H. Burr Proton Therapy Center in Boston, Massachusetts in April 2013 over a 5 hour period and a total fluence of $\sim 8.5 \times 10^{15}$ protons/cm². The sample was then submitted to step heating at the Noble Gas Thermochemistry Lab at Berkeley Geochronology Center following procedures described in Shuster and Farley (2004, 2005a). The sample was held isothermally in a diode laser heating apparatus controlled using a PID feedback loop and a type-K thermocouple at temperatures between 125 and 1200 °C (Gourbet and others, 2012). Heating step times ranged from 30 to 180 minutes. ^4He and spallogenic (proton-induced) ^3He evolved during each heating step were each measured using a MAP-215 sector field mass spectrometer.

Measurement of U, Th, and other elements in dated aliquots.—U and Th contents of each dated and undegassed aliquot were measured by isotope dilution and solution ICPMS, as described by Reiners (2005). Our laboratory trials suggest that hematite and Mn oxides do not fully dissolve in nitric acid, hydrochloric acid, or aqua regia, thus requiring HF dissolution in a pressure digestion vessel (Parr bomb). Following addition of a ^{233}U - ^{229}Th spike, equilibration, and dissolution, U and Th isotopes were measured on an Element 2 ICPMS.

The same solutions used for U-Th isotope dilution measurements were also used to measure contents of several elements in the bulk samples by ICPMS. These solutions contained the dissolved sample aliquot of Fe- or Mn-oxide plus any other phases present as inclusions or interstitial material, the dissolved Nb-tubes used for lasing and transporting the aliquots, as well as ^{233}U and ^{229}Th spike used for measuring natural U and Th in the aliquots. The large dissolved load of the Nb tubes results in a significant matrix effect and large but variable sensitivity drift over minutes to hours during this type of analysis. To account for these effects, we used ^{229}Th as an internal sensitivity standard, and dissolved Nb tubes in working standard solutions. Fe was calibrated with 0.5 to 4 ppm standard solutions, and other, lower concentration elements were calibrated with 1 to 100 ppb solutions. These analyses can be represented as total contents of each element in an aliquot, but because each aliquot was not weighed prior to analysis and each is a heterogeneous mixture of phases, it is not possible to report a mass-based concentration of each element. Nonetheless, assuming that the majority of the matrix is hematite or Mn-oxide, the approximate molar concentration of an element in the oxide matrix can be estimated from the ratio of the abundance of this element to the sum of the abundance of Fe and Mn. We use this estimation of concentration for hematite samples. For Mn oxides, we calculate ratios of elements to Mn alone, to preserve the information that these concentrations might provide about the variable mineral composition of each aliquot. Herein, we refer to these values as “molar ratios.”

The molar ratios of minor and trace-elements are only representative of the actual geologic specimen if these elements (along with Fe and/or Mn) were not volatilized during laser heating or lost in another part of the analytical procedure. We address this in the Discussion, using the concentrations of relatively volatile elements in undegassed aliquots as one way to assess the possible effects of open system behavior during laser heating and analysis.

Assuming full dissolution and recovery of Fe in each sample, the estimated total mass of hematite or Mn oxide for most samples is between 20 to 150 μg . Based on

comparisons with standards, repeat measurements, and measurements at different mass resolutions, the uncertainties on the element contents are estimated to be 5 to 10 percent (1σ).

SEM and Electron Probe Analysis

Polished, carbon-coated mounts of hematite and Mn oxide sample fragments were examined using a Hitachi 3400N SEM equipped with an Oxford EDS/EBSD system. We used the SEM to acquire back-scattered electron (BSE) and secondary electron (SE) images of sample fragments, along with energy-dispersive X-ray (EDS) maps. These sample fragments were also analyzed using a Cameca SX100 Electron Probe Micro Analyzer (EPMA). During each analysis, the peak, high background, and low background wavelength ranges were each measured for the given counting time. All elements in hematite crystals were measured using an accelerating voltage (AV) of 25 keV, an elevated beam current of 600 nA, and a 30 s counting time, except for Fe and Si, which were measured using a 20 nA current and a 20 s counting time. Mn oxide analyses were performed using an AV of 25 keV, a 20 nA current, and a 10 s counting time. Chlorite analyses were performed using an AV of 15 keV, a 20 nA current, and a 10 s counting time. Chrysocolla is water-rich and has an amorphous structure (Frost and Yi, 2013). To avoid melting target material, chrysocolla analyses were performed using an AV of 15 keV, a reduced beam current of 2 nA, and a 10 s counting time. The beam diameter was set at the minimum ($\sim 0.1 \mu\text{m}$) for chlorite and Mn oxide analyses. High current settings used during hematite analysis yielded a 6 to 8 μm beam diameter. In an effort to spread the effects of beam heating over a larger area, chrysocolla was analyzed using a 20 μm beam diameter.

RESULTS

Hematite Samples

SEM imaging and textural analysis.—With the exception of sample FW2-12-85-8 (which comprises large, rhombohedral crystals), all hematite samples examined in this study are aggregates of plate-shaped hematite crystals (table 1, figs. 2, A1, A2). Spaces between hematite crystals in these plate aggregate samples are filled with a variety of minerals herein referred to collectively as interstitial phases. The most common interstitial phases are chlorite, chrysocolla, and quartz; calcite and amorphous silica are less abundant. Following textural relationships described in table 1 (and previous descriptions of detachment-related mineralization), we suggest that hematite precipitated from parent fluids before most other minerals observed in analyzed samples. Quartz and apatite, both of which are often present as inclusions in hematite crystals, likely formed prior to or at the same time as hematite in most samples. Other phases formed later, filling spaces between euhedral crystals of these three minerals.

Electron probe micro-analyzer (EPMA) analyses.—Several elements that are abundant in common interstitial phases are present at only minor- or trace-element levels in hematite (table 2, table A1). The high concentration of Mg in chlorite relative to hematite (tables 2 and 3) suggests that most of the Mg measured in dated aliquots of hematite samples is present in chlorite. Following this, it is likely that the Mg molar ratio measured in a given aliquot is closely related to the chlorite volume fraction. Chlorite may have the same effect on Mn and Ca molar ratios of hematite aliquots. The molar ratios of Mg and Ca relative to Fe (table 3) measured in chrysocolla [a phase that is abundant in sample FW3-23-85-8 (fig. A1) and uncommon in sample FW3-21-85-12 (fig. A2)] suggest that this phase also contributes to higher molar ratios of Mg and Ca in hematite aliquots.

(U-Th)/He analyses.—With the exception of six aliquots, all dates obtained from hematite samples fall within the window of possible active extension in the Buckskin-

TABLE 2
Electron probe-measured abundances of minor elements in hematite crystals

Sample	Mg			Mn			Ca		
	Mean	Minimum	Fraction <DL	Mean	Minimum	Fraction <DL	Mean	Minimum	Fraction <DL
FW3-23-85-8	125	108	0.78	97	69	0	98	67	0.67
FW2-12-85-8	---	(87)*	1	96	67	0	92	48	0.50
FW3-21-85-12	608	294	0.10	208	142	0	603	321	0
FW11-29-11-1	93	93	0.92	157	105	0	81	30	0.62
HW1-16-12-1	87	87	0.92	124	89	0	607	44	0.42
HW11-30-11-3	---	(87)*	1	142	117	0	154	33	0.40

All element abundances expressed as $\mu\text{mol element}/(\text{mol Fe} + \text{mol Mn})$. Individual analyses provided in table A1.

* Where none of the EMPA analyses performed on hematite crystals in a given sample yielded a concentration above the detection limit, the average detection limit is listed in parentheses as the minimum abundance for that sample.

TABLE 3
Representative EPMA analyses of chlorite and chrysocolla from hematite samples

	CHLORITE				CHRYSOCOLLA			
	HW1-16-12-1	FW3-21-85-12	FW3-23-85-8	HW11-30-11-3	FW3-21-85-12	FW3-23-85-8 - 1	FW3-23-85-8 - 2	
	wt%							
Cu	<DL	0.15	1.48	0.12	0.10	28.58	29.88	26.14
Al	8.85	9.49	10.14	0.25	0.23	0.99	0.86	0.19
Si	14.08	12.43	13.21	0.15	0.15	16.33	18.57	14.49
Cr	0.03	<DL						
Fe	17.90	20.95	17.21	0.35	0.36	11.14	3.08	0.52
Mn	0.19	0.20	0.17	0.05	0.04	<DL	<DL	<DL
Mg	9.71	8.48	10.13	0.17	0.15	0.35	0.11	0.11
Ca	0.11	0.06	0.03	0.01	0.02	0.42	0.15	0.07
Na	<DL	0.04	<DL	0.02	0.02	<DL	<DL	<DL
K	0.11	0.02	<DL	0.61	0.03	<DL	<DL	<DL
Cl	0.02	0.01	<DL	0.02	0.01	<DL	<DL	0.18
O	35.59	34.33	36.13	34.39	30.33	30.52	30.52	23.47
Total	86.65	86.15	88.57	84.87	88.38	83.34	83.34	65.13
Abundances from above analyses, recalculated as $\mu\text{mol (element)}/(\text{mol Fe} + \text{Mn})$								
Mg	1.23×10^6	9.21×10^5	1.34×10^6	1.05×10^6	7.18×10^4	8.50×10^4	8.50×10^4	---
Mn	1.09×10^4	9.49×10^3	1.01×10^4	8.25×10^3	---	---	---	---
Ca	8.28×10^3	3.77×10^3	2.50×10^3	1.44×10^4	5.27×10^4	6.94×10^4	6.94×10^4	5.76×10^5

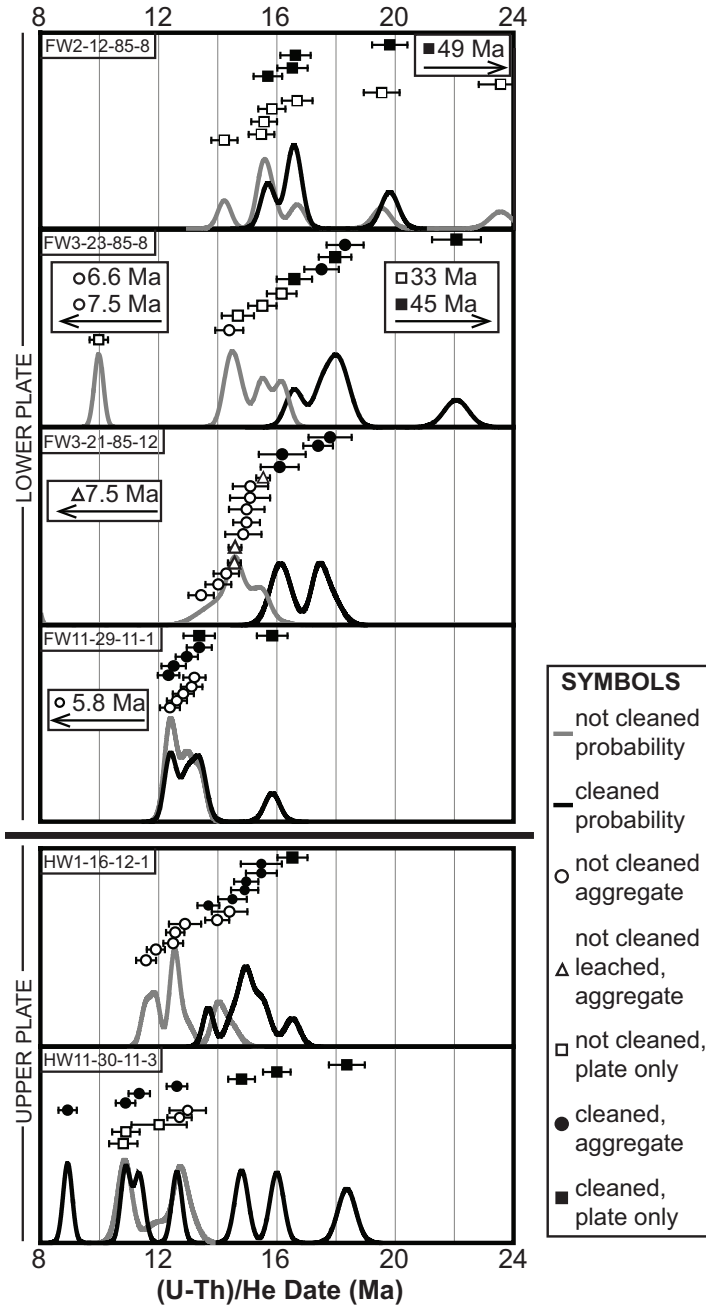


Fig. 3. Relative probability plots of hematite (U-Th)/He dates. Solid lines are probability curves generated from all cleaned and not cleaned aliquots in each sample. Error bars on data points represent 1σ uncertainty. Symbols explained on lower right. The ages of aliquots falling outside of the plotted 24 to 8 Ma range are shown in boxes as data points without error bars, with age labels to the right of each point.

Rawhide detachment system (26 to ~8 Ma, fig. 3, table 4). Eighty-seven percent of all hematite dates fall within a range that corresponds to a more restricted estimate of the

TABLE 4
Hematite and Mn oxide (U-Th)/He data

Aliquot [†]	Type*	Discarded? **	fml He	1σ ±	ng U	1σ ±	ng Th	1σ ±	Th/U	date (Ma)	1σ ± (Ma)	1σ ± %
FW2-12-85-8 - Hematite												
NC1	PO	N	18.02	0.042	0.213	0.0031	0.0060	0.00014	0.028	15.57	0.22	1.39
NC2	PO	N	6.38	0.019	0.073	0.0011	0.0057	0.00015	0.078	15.83	0.23	1.45
NC3	PO	N	9.51	0.022	0.112	0.0016	0.0065	0.00012	0.058	15.48	0.22	1.40
NC4	PO	Y	9.16	0.077	0.069	0.0010	0.0132	0.00020	0.192	23.56	0.37	1.57
NC5	PO	N	9.88	0.069	0.109	0.0016	0.0027	0.00009	0.025	16.69	0.26	1.55
NC6	PO	N	12.04	0.072	0.154	0.0023	0.0142	0.00021	0.092	14.23	0.22	1.56
NC7	PO	N	27.01	0.169	0.250	0.0038	0.0281	0.00041	0.112	19.54	0.30	1.55
C1	PO	N	8.59	0.057	0.095	0.0014	0.0052	0.00010	0.055	16.63	0.25	1.53
C2	PO	N	20.38	0.131	0.189	0.0027	0.0049	0.00009	0.026	19.82	0.30	1.50
C3	PO	N	2.95	0.022	0.033	0.0005	0.0066	0.00016	0.197	15.70	0.24	1.54
C4	PO	N	22.75	0.152	0.253	0.0037	0.0078	0.00015	0.031	16.53	0.26	1.54
C5	PO	Y	3.63	0.037	0.012	0.0002	0.0060	0.00013	0.492	49.19	0.93	1.89
UD1	PO	---	---	---	0.156	0.0023	0.0065	0.00020	0.042	---	---	---
UD2	PO	---	---	---	0.088	0.0013	0.0054	0.00014	0.061	---	---	---
UD3	PO	---	---	---	0.036	0.0005	0.0039	0.00009	0.108	---	---	---
FW3-23-85-8 - Hematite												
NC1	PO	N	35.04	0.436	0.441	0.0063	0.0052	0.00010	0.012	14.68	0.27	1.85
NC2	PO	N	16.86	0.120	0.313	0.0045	0.0023	0.00008	0.007	9.98	0.15	1.55
NC3	PO	N	158.10	1.099	1.885	0.0269	0.0245	0.00039	0.013	15.51	0.24	1.54
NC4	PO	Y	60.30	0.436	0.329	0.0047	0.0079	0.00019	0.024	33.77	0.52	1.55
NC5	PO	N	65.28	0.468	0.746	0.0107	0.0114	0.00022	0.015	16.16	0.25	1.55
NC6	A	Y	110.65	1.747	3.120	0.1336	0.0048	0.00007	0.002	6.60	0.29	4.43
NC7	A	Y	326.67	1.227	8.105	1.6251	0.0132	0.00019	0.002	7.50	1.45	19.37
NC8	A	N	80.51	0.374	1.040	0.0170	0.0042	0.00006	0.004	14.39	0.24	1.64
C1	PO	N	113.11	0.772	1.155	0.0165	0.0055	0.00075	0.045	17.97	0.27	1.52
C2	PO	N	42.50	0.481	0.473	0.0069	0.0072	0.00014	0.015	16.59	0.30	1.80
C3	PO	N	7.38	0.092	0.061	0.0009	0.0032	0.00015	0.053	22.07	0.41	1.87
C4	PO	Y	12.88	0.085	0.051	0.0008	0.0029	0.00010	0.057	45.76	0.71	1.55
C5	A	N	134.68	1.267	1.425	0.0203	0.0054	0.00026	0.004	17.51	0.29	1.66
C6	A	N	88.04	0.893	0.890	0.0127	0.0062	0.00012	0.007	18.31	0.31	1.71

TABLE 4
(continued)

Aliquot [†]	Type*	Discarded? **	fmol He	1 σ ±	ng U	1 σ ±	ng Th	1 σ ±	Th/U	date (Ma)	1 σ ± (Ma)	1 σ ± %
FW3-23-85-8 - Hematite												
UD1	A	---	---	---	0.092	0.0013	0.0095	0.00016	0.104	---	---	---
UD2	A	---	---	---	0.168	0.0024	0.0068	0.00018	0.040	---	---	---
UD3	A	---	---	---	0.143	0.0021	0.0042	0.00010	0.029	---	---	---
FW3-21-85-12 - Hematite												
NC1	A	N	41.20	0.599	0.503	0.0073	0.0309	0.00046	0.061	14.98	0.30	2.00
NC2	A	N	43.18	0.672	0.532	0.0075	0.0300	0.00044	0.056	14.87	0.31	2.06
NC3	A	N	27.31	0.396	0.327	0.0046	0.0366	0.00053	0.112	15.11	0.30	1.97
NC4	A	N	22.24	0.157	0.263	0.0038	0.0518	0.00075	0.197	14.97	0.23	1.51
NC5	A	N	56.67	0.367	0.722	0.0103	0.0581	0.00085	0.081	14.29	0.21	1.50
NC6	A	N	35.25	0.165	0.453	0.0072	0.0614	0.00090	0.136	14.02	0.22	1.55
NC7	A	N	73.68	0.351	0.888	0.0206	0.0839	0.00123	0.094	15.09	0.34	2.24
NC8	A	N	18.47	0.124	0.251	0.0038	0.0187	0.00027	0.075	13.44	0.21	1.59
C1	A	N	21.48	0.310	0.244	0.0035	0.0131	0.00020	0.054	16.10	0.32	1.99
C2	A	N	12.81	0.260	0.145	0.0021	0.0090	0.00015	0.062	16.18	0.40	2.44
C3	A	N	29.47	0.467	0.290	0.0041	0.0725	0.00103	0.250	17.80	0.36	2.05
C4	A	N	35.48	0.224	0.354	0.0051	0.1017	0.00151	0.287	17.40	0.25	1.44
L-NC1	A	N	14.21	0.086	0.164	0.0023	0.0235	0.00036	0.143	15.54	0.23	1.50
L-NC2	A	N	25.74	0.196	0.320	0.0046	0.0332	0.00054	0.104	14.56	0.22	1.50
L-NC3	A	Y	13.01	0.097	0.302	0.0043	0.0228	0.00035	0.076	7.86	0.12	1.50
L-NC4	A	N	32.81	0.169	0.410	0.0059	0.0309	0.00046	0.075	14.58	0.22	1.48
UD1	A	---	---	---	0.424	0.0060	0.0440	0.00065	0.104	---	---	---
UD2	A	---	---	---	0.440	0.0063	0.0262	0.00041	0.060	---	---	---
UD3	A	---	---	---	0.246	0.0035	0.0178	0.00029	0.072	---	---	---
FW11-29-11-1 - Hematite												
NC1	A	Y	27.94	0.051	0.865	0.0124	0.1004	0.00147	0.116	5.84	0.08	1.35
NC2	A	N	2.86	0.011	0.039	0.0006	0.0113	0.00021	0.292	12.84	0.18	1.39
NC3	A	N	8.19	0.022	0.113	0.0016	0.0307	0.00047	0.271	12.62	0.17	1.34
NC4	A	N	19.53	0.040	0.273	0.0040	0.0072	0.00013	0.027	13.21	0.19	1.42
NC5	A	N	9.97	0.026	0.140	0.0021	0.0387	0.00056	0.276	12.39	0.17	1.35
NC6	A	N	10.09	0.021	0.140	0.0020	0.0094	0.00016	0.067	13.12	0.18	1.38

TABLE 4
(continued)

Aliquot [†]	Type* [‡]	Discarded?***	fmol He	1σ ±	ng U	1σ ±	ng Th	1σ ±	Th/U	date (Ma)	1σ ± (Ma)	1σ ± %
FW11-29-11-1 - Hematite												
C1	A	N	4.97	0.039	0.068	0.0010	0.0039	0.00014	0.057	13.38	0.21	1.58
C2	A	N	9.32	0.054	0.133	0.0020	0.0284	0.00045	0.213	12.34	0.18	1.48
C3	A	N	15.87	0.085	0.222	0.0032	0.0222	0.00034	0.100	12.96	0.19	1.45
C4	A	N	9.94	0.091	0.145	0.0021	0.0114	0.00039	0.079	12.51	0.21	1.64
C5	PO	Y	5.93	0.046	0.067	0.0010	0.0113	0.00020	0.169	15.84	0.26	1.63
C6	PO	N	8.19	0.119	0.111	0.0016	0.0123	0.00027	0.111	13.38	0.26	1.98
HW1-16-12-1 - Hematite												
NC1	A	N	8.62	0.144	0.114	0.0017	0.0443	0.00065	0.390	12.89	0.27	2.11
NC2	A	N	6.38	0.019	0.077	0.0012	0.0315	0.00052	0.408	13.98	0.20	1.45
NC3	A	N	4.23	0.023	0.054	0.0008	0.0365	0.00059	0.674	12.49	0.17	1.33
NC4	A	N	13.21	0.033	0.182	0.0027	0.0992	0.00143	0.544	11.91	0.15	1.28
NC5	A	N	13.21	0.222	0.147	0.0021	0.0963	0.00140	0.653	14.40	0.30	2.08
NC6	A	N	24.48	0.190	0.348	0.0050	0.1860	0.00267	0.534	11.57	0.17	1.46
NC7	A	N	16.22	0.036	0.207	0.0030	0.1358	0.00195	0.655	12.56	0.16	1.24
C1	A	N	8.06	0.148	0.087	0.0013	0.0393	0.00065	0.450	15.47	0.35	2.24
C2	A	N	8.06	0.047	0.091	0.0013	0.0769	0.00120	0.845	13.68	0.18	1.35
C3	A	N	20.05	0.107	0.239	0.0037	0.0424	0.00121	0.177	14.91	0.23	1.54
C4	A	N	18.57	0.091	0.212	0.0030	0.0789	0.00062	0.373	14.96	0.20	1.36
C5	A	N	5.22	0.053	0.061	0.0009	0.0257	0.00038	0.423	14.49	0.24	1.67
C6	A	N	3.05	0.032	0.033	0.0005	0.0147	0.00022	0.444	15.47	0.26	1.69
C7	PO	N	5.06	0.041	0.053	0.0008	0.0173	0.00030	0.327	16.52	0.25	1.53
NC-UD1	A	---	---	---	0.144	0.0021	0.0720	0.00105	0.501	---	---	---
HW1-16-12-1 - Hematite												
NC-UD2	A	---	---	---	0.017	0.0003	0.0131	0.00021	0.750	---	---	---
NC-UD3	A	---	---	---	0.025	0.0004	0.0169	0.00029	0.683	---	---	---
C-UD1	A	---	---	---	0.196	0.0028	0.0473	0.00069	0.241	---	---	---
C-UD2	A	---	---	---	0.028	0.0004	0.0117	0.00021	0.421	---	---	---
HW11-30-11-3 - Hematite												
NC1	A	N	18.10	0.162	0.254	0.0037	0.0416	0.00061	0.163	12.71	0.21	1.62
NC2	PO	N	0.52	0.008	0.007	0.0001	0.0069	0.00019	0.941	10.89	0.23	2.13

TABLE 4
(continued)

Aliquot [†]	Type*	Discarded?,**	fmol He	1σ ±	ng U	1σ ±	ng Th	1σ ±	Th/U	date (Ma)	1σ ± (Ma)	1σ ± %
HW11-30-11-3 - Hematite												
NC3	PO	N	0.65	0.010	0.009	0.0004	0.0061	0.00021	0.709	12.02	0.47	3.88
NC4	PO	N	0.47	0.007	0.007	0.0001	0.0038	0.00010	0.528	10.80	0.24	2.21
NC5	A	N	0.71	0.012	0.009	0.0002	0.0046	0.00011	0.506	12.98	0.31	2.37
C1	A	N	23.16	0.116	0.315	0.0045	0.1077	0.00154	0.342	12.62	0.17	1.37
C2	A	N	11.13	0.105	0.168	0.0024	0.0600	0.00101	0.358	11.35	0.18	1.59
C3	A	N	12.00	0.109	0.178	0.0025	0.1139	0.00179	0.642	10.88	0.17	1.52
C4	A	N	2.84	0.028	0.055	0.0009	0.0149	0.00033	0.269	8.92	0.15	1.73
C5	PO	N	6.66	0.044	0.070	0.0012	0.0570	0.00099	0.816	14.80	0.23	1.53
C6	PO	N	6.89	0.051	0.063	0.0011	0.0288	0.00042	0.459	18.36	0.30	1.65
C7	PO	N	12.84	0.093	0.134	0.0019	0.0624	0.00110	0.466	16.00	0.23	1.46
Priceless Mine – Mn Oxide												
NC1	---	N	20.50	0.071	0.244	0.0036	0.0026	0.00009	0.011	15.57	0.23	1.45
NC2	---	N	21.99	0.073	0.293	0.0042	0.0020	0.00008	0.007	13.91	0.20	1.42
NC3	---	N	19.37	0.066	0.305	0.0044	0.0029	0.00008	0.009	11.74	0.17	1.44
NC4	---	N	12.63	0.032	0.167	0.0024	0.0032	0.00010	0.019	13.96	0.20	1.41
UD1	---	---	---	---	0.097	0.0014	0.0060	0.00014	0.061	---	---	---
UD2	---	---	---	---	0.121	0.0017	0.0045	0.00011	0.037	---	---	---
UD3	---	---	---	---	0.083	0.0012	0.0057	0.00011	0.068	---	---	---
Shannon Mine – Mn Oxide												
NC1	---	N	23.13	0.048	0.504	0.0073	0.0065	0.00032	0.013	8.48	0.12	1.40
NC2	---	N	31.02	0.054	0.736	0.0106	0.0027	0.00006	0.004	7.82	0.11	1.39
NC3	---	N	25.11	0.043	0.610	0.0088	0.0069	0.00012	0.011	7.62	0.11	1.39

* "Aliquot" provides information about aliquot treatment: C is ultrasonically cleaned, NC is not cleaned, UD is undegassed (not heated with laser), L is leached. Unless otherwise specified in this column, UD aliquots are not cleaned.
 ** "Discarded?" indicates whether the aliquot was excluded from consideration based on factors covered in the Discussion section; data from discarded NC aliquots are shown in all figures but are not included in calculation of mean dates in table 12, which are plotted in figure 13.

timing of rapid lower-plate cooling (20–9 Ma, based on Scott and others, 1998; Singleton and Stockli, 2013; Spencer and others, 2013). Among most plate aggregate samples, cleaned aliquots yield older dates than NC aliquots, although some overlap is observed between these two treatments (fig. 3). Such a difference is not apparent in samples FW11-29-11-1, FW2-12-85-8, or HW11-30-11-3.

Chemical compositions of dated and un-degassed aliquots.—We express the abundance of parent nuclides in hematite aliquots as the ratio of $\mu\text{moles eU}$ (effective uranium, a measure that encompasses both U and Th, $\text{eU} = \text{mol U} + 0.235 \times \text{mol Th}$; Flowers and others, 2009) to moles Fe + Mn measured in each aliquot (table A2). We follow the same standard for expressing the molar ratios of other elements in Fe oxide aliquots. In all plate aggregate samples except FW11-29-11-1 and HW11-30-11-3, cleaned aliquots typically display lower eU molar ratios than NC aliquots. Weak inverse relationships between date and eU (figs. 4C–4E) are also observed in these samples. Aliquots with the highest measured eU contents are observed in plate aggregate samples that contain chrysocolla (figs. 4C–4D). This is consistent with the very high concentrations of U measured in aliquots of chrysocolla from sample FW3-23-85-8 (table 5). Th/U ratios measured in chrysocolla fall below the Th/U ratios observed in all dated and undegassed hematite aliquots (table 4).

The few dated aliquots that yield dates greater than the age of activity on the detachment (>26 Ma) also yield low eU molar ratios and high Th/U ratios relative to other dated and undegassed aliquots from their respective samples. Examples of this can be observed in samples FW2-12-85-8 and FW3-23-85-8 (figs. 4B and 4C, table 4).

Aliquots from sample FW3-21-85-12 subjected to pH 3 nitric acid pre-treatment yield dates similar to other NC aliquots from this sample, with the exception of one 7.9-Ma aliquot. Less than 2.5 percent of the total U in leached aliquots was removed by the end of the leaching process, although a greater fraction of U was removed from aliquots that were not leached in Nb tubes (table 6). No Th was measured in leaching solutions. Several previous studies indicate that in fluid environments with $\text{pH} < 4$, very little U is adsorbed on the surfaces of iron oxides (Giblin and others, 1981; Hsi and Langmuir, 1985; Shuibo and others, 2009) or chlorite and other sheet silicates (Arnold and others, 1998; Arnold and others, 2001; Singer and others, 2009). Therefore, we suggest that only a small amount of the total U (and none of the Th) in this sample is present in an adsorbed form. Additional experiments that test this assertion in this and other samples may be warranted. Leached aliquots yield eU, Mg, and Mn molar ratios similar to those measured in other NC aliquots (triangle-shaped data points, figs. 4D, 5B, and 5D). In figure 3, and in subsequent sections of the paper, these aliquots are grouped with other NC aliquots from this sample.

We observe inverse relationships between (U-Th)/He date and Mg and Mn molar ratios in data obtained from several plate aggregate samples (fig. 5). Among aliquots from a given sample, NC aliquots typically yield higher Mg and Mn molar ratios than cleaned aliquots. Mg molar ratios measured in most dated and undegassed aliquots exceed those measured by EPMA in hematite crystals of each sample (table 2, minimum EPMA-measured molar ratios are vertical lines in figs. 5A and 5B). The same is true of Ca molar ratios measured in dated and undegassed aliquots (table A2). This indicates that some of the Mg and Ca in these aliquots is present in phases other than hematite (a finding consistent with relatively high Mg and Ca molar ratios measured in interstitial phases, table 3). A fraction of dated aliquots from each hematite sample (often cleaned or plate-only aliquots) yield Mn molar ratios lower than the lowest molar ratio measured in undegassed aliquots and by EPMA in hematite crystals alone (figs. 5C and 5D, table 2). This may indicate that a fraction of the total Mn present in hematite aliquots may be removed from both hematite crystals and other phases in these aliquots during the (U-Th)/He analytical process.

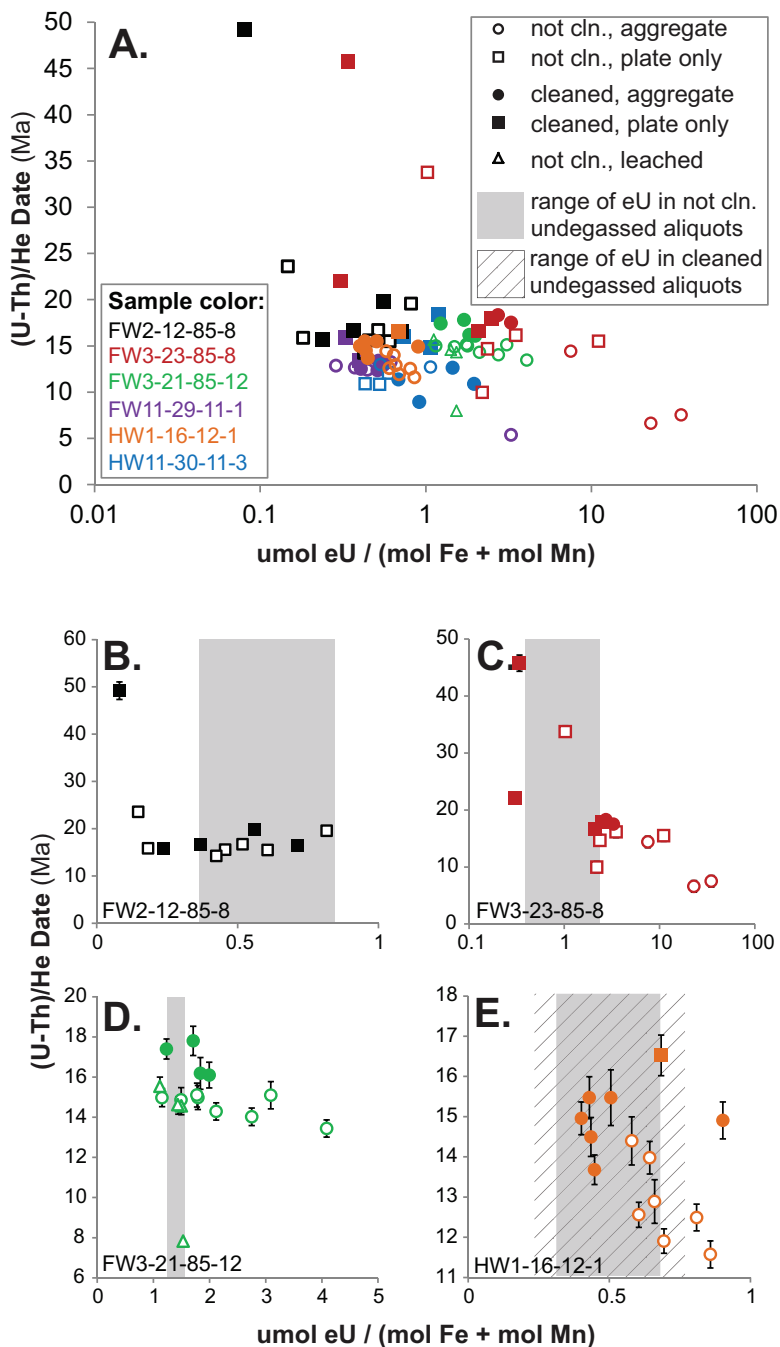


Fig. 4. Plots of hematite (U-Th)/He date versus eU molar ratio. eU molar ratio in (A) and (C) are plotted on a log scale. (A) Plot of all data. Symbols explained in legend in upper right. (B)–(E) Plots of data from individual samples. Error bars are 2σ date uncertainty. Shaded/cross-hatched regions represent ranges of eU molar ratios in undegassed aliquots of each sample. Note that cleaned (filled) aliquots tend to yield older dates and lower eU molar ratios than not cleaned (NC, open) aliquots.

TABLE 5
U and Th concentrations in chrysocolla from sample FW3-23-85-8

Pre-treatment	ng U	± 1σ ng U	ng Th	± 1σ ng Th	Aliquot mass (mg)	ppm U	ppm Th	Th/U	umol eU/mol Fe in aliquot given Fe abundance*: 3 wt% Fe	0.5 wt% Fe	25104
Cleaned	55.00	0.79	0.0083	0.0003	0.1028	535	0.08	0.00015	4184		
Cleaned	3.79	0.05	0.0062	0.0001	0.01475	257.1	0.42	0.00164	2011		12066
Not Cleaned	20.14	0.29	0.0087	0.0002	0.03555	566.7	0.24	0.00043	4432		26590
Not Cleaned	10.53	0.15	0.0067	0.0005	0.0408	258.2	0.16	0.00063	2019		12115

* eU contents expressed with respect to Fe content of chrysocolla in this sample (Mn not detected in chrysocolla, see table 3). Two estimates of μmol eU/(mol Fe) are provided, one using the highest Fe concentration in chrysocolla listed in table 3, and one using a lower Fe concentration.

TABLE 6
Parent nuclide abundances in aliquot leaching solutions, hematite sample FW3-21-85-12

Aliquot no.*	Packed in Nb?	ng U in dated aliquot	ng U in 1 hr leach sol.**	ng U in 72 hr leach sol.**	total ng U leached	% U leached
L-NC1	N	0.1640	0.0011	0.0026	0.0037	2.256
L-NC2	N	0.3200	0.0001	0.0060	0.0061	1.872
L-NC3	Y	0.3016	0.0000	0.0022	0.0022	0.719
L-NC4	Y	0.4099	0.0000	0.0008	0.0008	0.190

* Aliquot number refers to tables 4 and A2.

** Values account for the amount of each element that was left in the leaching vial after solution was removed at one and 72 hours.

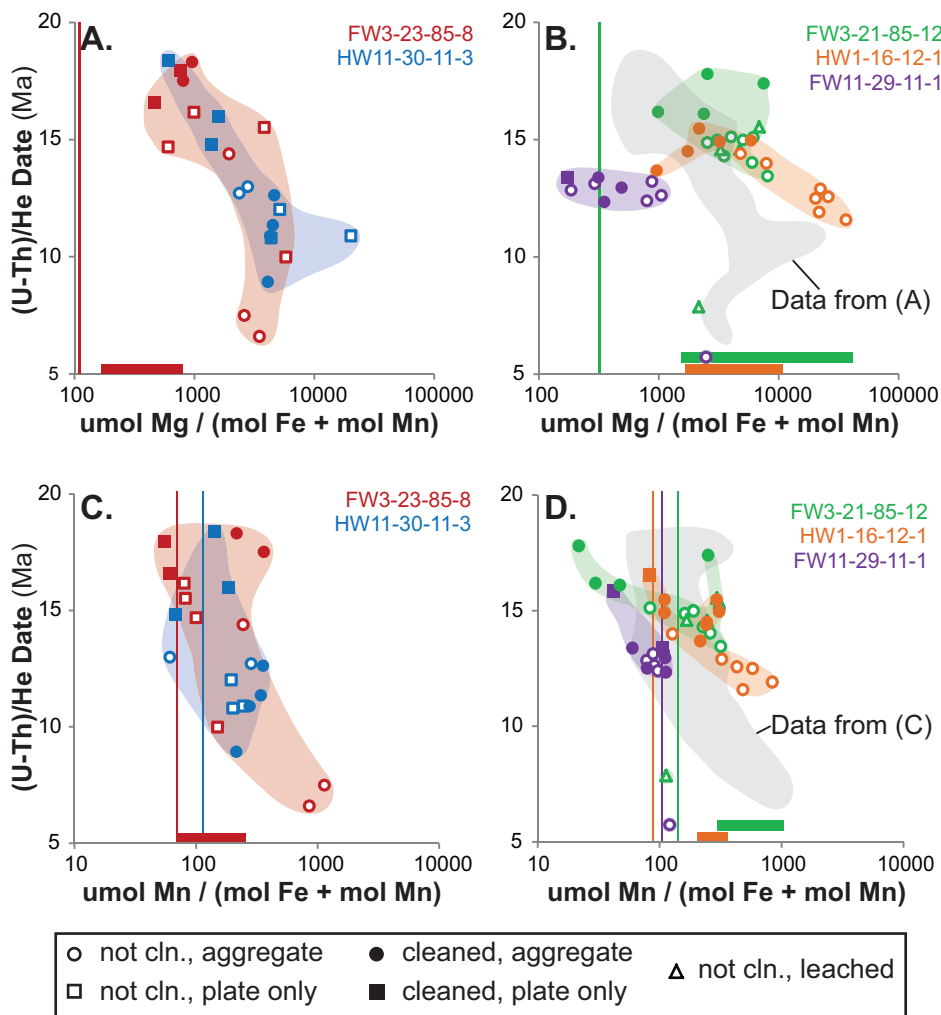


Fig. 5. (A) and (B) Plots of hematite (U-Th)/He date versus Mg molar ratio for all plate aggregate hematite samples (sample FW2-12-85-8 not shown). Vertical lines represent the minimum Mg molar ratio measured by EPMA in hematite crystals in each sample (table 2). If a line for a sample is not shown, the minimum Mg molar ratio for this sample is $<100 \mu\text{mol Mg}/(\text{mol Fe} + \text{mol Mn})$. Horizontal bars above the x-axis represent the range of Mg molar ratios measured in undegassed aliquots from each sample. Aliquots from samples FW3-23-85-8 and 11-29-11-1 with low Mg molar ratios are not shown. Note that Mg molar ratios are higher among NC aliquots in most samples. (C) and (D) Plots of (U-Th)/He date versus Mn molar ratio, with minimum EPMA abundances and undegassed aliquot compositions shown in the same manner as in (A) and (B). Three aliquots from sample FW 3-23-85-8 (dates 22–45 Ma), each with Mn molar ratios $<30 \mu\text{mol/mol}$, are not shown.

Pb and Cu molar ratios measured in undegassed aliquots are greater than the molar ratios of these elements measured in dated aliquots. Figure 6 shows Pb molar ratio plotted versus Cu molar ratio for all aliquots taken from samples from which undegassed aliquots were also analyzed. Undegassed aliquots form a field that is distinct from that formed by dated aliquots, with little overlap between the two populations.

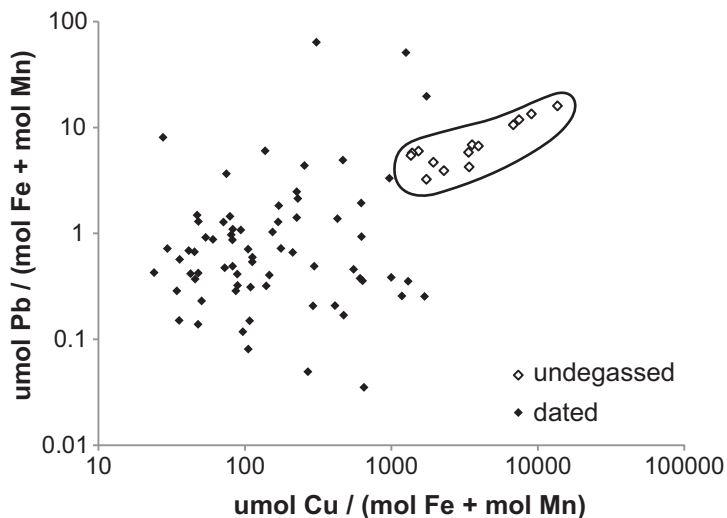


Fig. 6. Plot of Pb versus Cu molar ratios of all hematite aliquots from samples from which undegassed aliquots were analyzed. Note that undegassed aliquots yield higher molar ratios of both elements, with little overlap between the two populations. All undegassed hematite aliquot compositions fall within the field bordered by the solid black line.

⁴He step heating experiment—sample FW11-29-11-1.—A ⁴He step heating experiment on a polycrystalline aliquot from sample FW11-29-11-1 yielded an Arrhenius trend consistent with diffusion of ⁴He from multiple domains. We used the fractional loss equations for diffusion from a sphere (fig. 7A, table 7) and from a plane sheet (fig. 7B) to calculate D_0/a^2 values for each heating step (Fechtig and Kalbitzer, 1966). Retrograde and prograde portions of the heating schedule produced data that do not overlap on an Arrhenius plot (fig. 7). This pattern is consistent with sequential degassing of progressively larger diffusion domains through the course of the heating schedule. Data from two sets of prograde steps in the low-temperature part of the Arrhenius trend form linear arrays (P1 and P2 in fig. 7). Lines fit to these two prograde segments yield a small difference in D_0/a^2 (~ 0.25 natural log units). The slopes of these lines correspond to activation energies of 147 to 148 kJ/mol. Assuming an elevated cooling rate appropriate for the lower-plate setting of this sample (80 °C/Myr, Scott and others, 1998), these lines correspond to a closure temperature of 164 °C, while lines of the same slope (but a lower D_0/a^2 value) that intersect with higher-temperature points (from larger domains) correspond to a closure temperature of 209 °C.

⁴He/³He step-heating experiment—sample FW2-12-85-8.—Results of a ⁴He/³He step-heating experiment performed on an aliquot from sample FW2-12-85-8 are listed in table 8, and plotted in figure 8A. The analyzed aliquot is an internal fragment of a larger crystal with no obvious sign of internal structures that might divide the aliquot into smaller domains. The smallest half-width of this fragment is ~ 80 μm ; its maximum aspect ratio is ~ 3 . Most ($\sim 99\%$) of the ³He in this aliquot was extracted in prograde and retrograde steps that form two sub-linear segments on an Arrhenius plot (fig. 8A). Linear regressions of these segments imply E_a values ranging from 160 to 180 kJ/mol, and closure temperatures of 210 to 270 °C (assuming an 80 °C/Myr cooling rate). The ⁴He Arrhenius trend falls above the ³He Arrhenius trend in all but the last several steps of the experiment (fig. 8A). Prograde and retrograde segments of the ⁴He and ³He

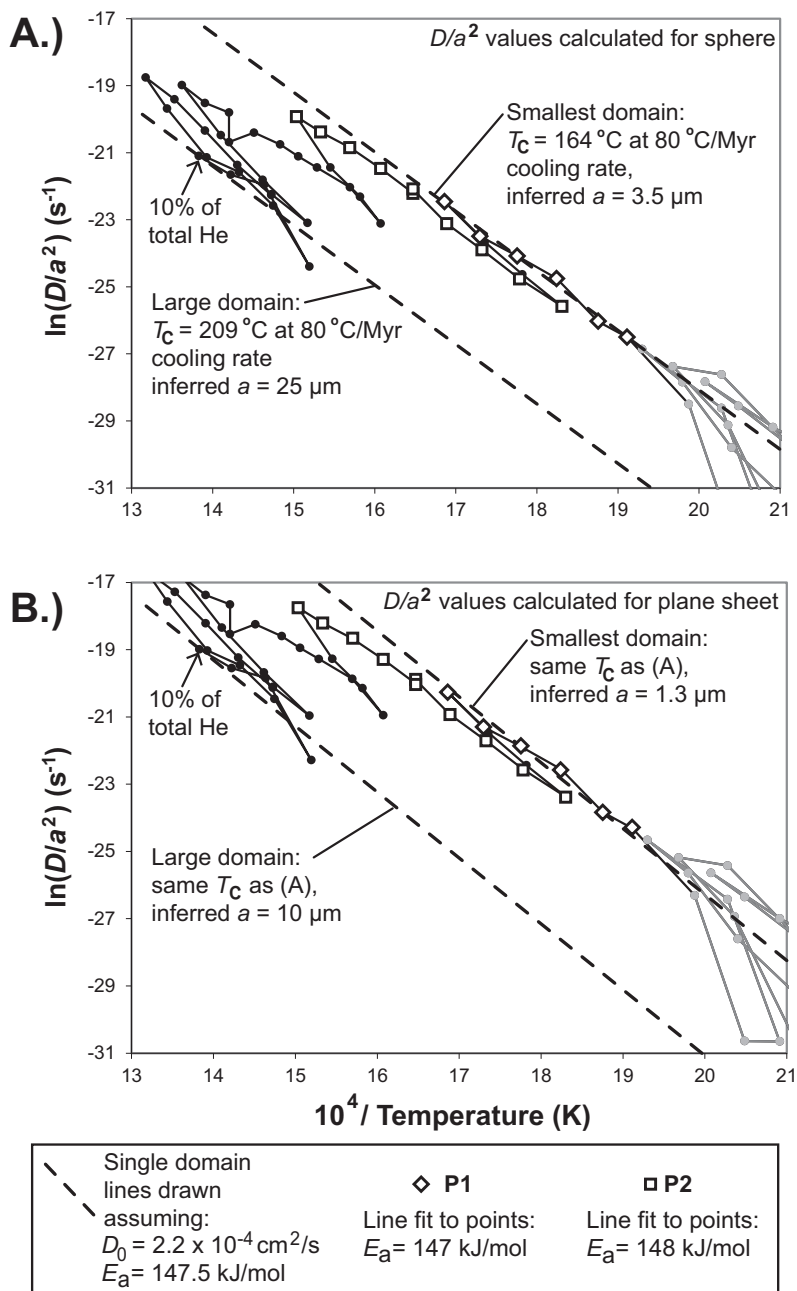


Fig. 7. (A) Arrhenius plot of diffusion data from polycrystalline hematite sample FW11-29-11-1 plotted assuming spherical diffusion domain geometry. Low temperature (T) steps (gray data points) are affected by low ^4He yields and do not yield a linear Arrhenius trend. Sub-linear segments (P1 and P2, open symbols) imply E_a values of 147–148 kJ/mol. Dashed lines representing single diffusion domains fit to lowest-T sub-linear segment and highest-T part of the dataset were plotted assuming $E_a = 147.5$ kJ/mol, the mean value of the P1 and P2 segments. Listed diffusion domain sizes (a values) were calculated from these domain lines assuming $D_0 = 2.2 \times 10^{-4} \text{ cm}^2/\text{s}$ (see Discussion for derivation of this value). Closure temperatures (T_c , calculated assuming $80^\circ \text{C}/\text{Myr}$ cooling rate from Scott and others, 1998) are listed for these domains. (B) Arrhenius plot of diffusion data shown in (A) calculated assuming plane sheet diffusion domain geometry. All other assumptions, symbols, and calculated values are the same as in (A). Domain lines that parallel low-T and high-T portions of the data correspond to domains with $a = 1.3\text{--}10 \mu\text{m}$, a better match to the $0.5\text{--}15 \mu\text{m}$ range of crystal half-widths observed in this sample than those obtained in (A) (table 1). This observation supports the use of plane sheet domain geometry in interpretation of data from other plate aggregate samples.

TABLE 7

⁴He diffusion data from hematite sample FW11-29-11-1 step heating experiment

Step	T (°C)	time (sec)	⁴ He (Matom)	f _{cumulative}	ln(D/a ²)*
1	145	7200	52.52	0.0000	-31.305
2	165	10800	32.63	0.0001	-31.223
3	185	14400	60.26	0.0001	-30.381
4	205	14400	113.25	0.0002	-29.189
5	225	14400	236.14	0.0004	-27.831
6	215	21900	118.48	0.0005	-28.554
7 ⁺	200	38820	54.13	0.0006	-29.765
8	220	14520	149.82	0.0007	-27.616
9	235	23400	242.36	0.0009	-27.377
10	218	48000	74.00	0.0010	-29.126
11 ⁺	198	47880	0.97	0.0010	-33.430
12 ⁺	173	46440	9.37	0.0010	-31.122
13 ⁺	197	55080	5.58	0.0010	-31.805
14 ⁺	217	41880	31.11	0.0010	-29.796
15	232	51660	242.29	0.0012	-27.842
16	245	29400	304.78	0.0015	-26.858
17	220	53580	85.18	0.0016	-28.616
18 ⁺	205	43560	0.98	0.0016	-32.847
19 ⁺	215	43200	0.99	0.0016	-32.835
20	230	52200	88.60	0.0017	-28.502
21	250	19800	227.76	0.0019	-26.506
22	260	24240	386.69	0.0022	-26.037
23	275	14400	677.08	0.0028	-24.750
24	290	14400	1017.93	0.0037	-24.082
25	305	14400	1388.17	0.0049	-23.490
26	320	14400	2746.09	0.0073	-22.454
27	303	48300	2046.09	0.0091	-23.662
28	288	28920	412.40	0.0094	-24.627
29	273	54180	288.65	0.0097	-25.578
30	289	46200	535.15	0.0101	-24.765
31	304	29400	764.72	0.0108	-23.900
32	319	23100	1212.45	0.0119	-23.118
33	334	3600	496.45	0.0123	-22.087
34	334	22740	2521.36	0.0145	-22.201
35	349	14400	2815.71	0.0169	-21.472
36	364	18300	5416.22	0.0217	-20.849
37	379	14400	5423.12	0.0264	-20.385
38	392	14040	6832.22	0.0323	-19.924
39	374	61200	5488.63	0.0371	-21.443
40	359	35340	1225.03	0.0382	-22.310
41	349	43200	655.42	0.0388	-23.114
42	364	33000	1443.38	0.0400	-22.031
43	381	44220	3308.25	0.0429	-21.442
44	391	28800	2815.90	0.0454	-21.109
45	401	52320	6645.64	0.0511	-20.755
46	416	27900	4567.80	0.0551	-20.401

TABLE 7
(continued)

Step	T (°C)	time (sec)	⁴ He (Matom)	f _{cumulative}	ln(D/a ²)*
47	431	50400	5715.19	0.0601	-20.683
48	431	25200	6292.70	0.0656	-19.803
49	446	15300	4704.29	0.0697	-19.517
50	461	14400	7003.78	0.0758	-18.981
51	436	32520	3324.06	0.0787	-20.477
52	411	29700	783.15	0.0794	-21.808
53	386	49320	356.67	0.0797	-23.095
54	406	39540	669.62	0.0803	-22.238
55	406	45000	735.36	0.0809	-22.266
56	426	29280	1164.17	0.0819	-21.366
57	446	37020	3975.46	0.0854	-20.343
58	466	19860	5167.68	0.0899	-19.408
59	486	18000	8399.17	0.0972	-18.753
60	471	33420	5724.99	0.1022	-19.687
61	445	29580	1149.23	0.1032	-21.138
62	425	48240	1198.50	0.1042	-21.574
63	405	36600	331.58	0.1045	-22.576
64	385	48600	71.29	0.1046	-24.395
65	410	40800	686.43	0.1052	-21.952
66	430	42300	949.08	0.1060	-21.657
67	450	37620	1461.12	0.1073	-21.097
Final	---	---	1024565.11	1	---

* D/a^2 values provided were calculated with equation for fractional loss from a spherical diffusion domain from Fechtig and Kalbitzer (1966).

[†] Rows in italic text represent heating steps with a ${}^4\text{He}_{\text{step}}/{}^4\text{He}_{\text{blank}}$ ratio of less than ~ 3 . Note that these data are confined to temperatures of $< 225^\circ\text{C}$.

Arrhenius trends are only partially overlapping, which, as discussed above, is interpreted as a sign of He diffusion from multiple domains. This characteristic is more pronounced in ${}^4\text{He}$ data; most ${}^3\text{He}$ is released from domains with $\ln(D_0/a^2)$ (y-intercept) values that vary by only 3 to 4 natural log units (assuming $E_a = 170$ kJ/mol). In contrast, single domain lines that intersect the lowest and highest-T points of the ${}^4\text{He}$ trend yield $\ln(D_0/a^2)$ values that differ by nearly 30 natural log units, with corresponding closure temperatures of ~ 50 to 300°C . If E_a is indeed constant among domains, this implies a large variation in D_0 , a , or both values among the domains that contain ${}^4\text{He}$.

Mn Oxide Samples

SEM imaging and textural analysis.—SEM analysis of Priceless Mine sample material indicates that it comprises microcrystalline material with compositional banding at a 1 to 100 micron scale (fig. 9A). The Shannon Mine sample displays a similar texture: it appears to be an aggregate of micron-scale, elongate, blade- or rod-shaped crystals. As seen in figure 9B, no compositional banding is visible in BSE images of this sample. Most crystals in this sample appear to be on the order of 0.1 to 1 μm in width (fig. 9C).

EPMA analyses.—Previous XRD characterizations of minerals from vein settings in the Priceless Mine deposit suggest that hollandite-group minerals, romanachite, and minor pyrolusite and ramsdellite are the Mn oxide phases present in this sample

TABLE 8

⁴He/³He data from hematite sample FW2-12-85-8 step-heating experiment

Step	T (°C)	time (sec)	⁴ He (Matom)	⁴ He - ln(D/a ²)*	³ He (Matom)	³ He - ln(D/a ²)*
1	175	1800	313.96	-19.00	<DL	---
2	120	10800	64.61	-21.58	0.035	-28.27
3	150	10800	158.32	-20.40	0.043	-26.89
4	180	7200	272.88	-19.07	0.023	-26.65
5	210	7200	510.14	-17.98	0.011	-27.22
6	240	7200	633.20	-17.34	0.043	-25.63
7	270	3600	492.06	-16.60	0.031	-25.02
8	300	3600	744.66	-15.86	0.037	-24.66
9	330	3600	912.38	-15.37	0.037	-24.49
10	360	3600	1023.76	-14.99	0.128	-22.96
11	320	3600	109.35	-17.09	0.033	-24.09
12	280	7200	47.89	-18.59	0.011	-25.83
13	240	7200	5.91	-20.68	0.013	-25.63
14	190	10800	0.59	-23.39	0.031	-25.12
15	370	3600	535.97	-15.42	0.084	-22.91
16	400	3600	817.66	-14.86	0.189	-21.86
17	430	3600	887.56	-14.62	0.350	-20.9
18	460	3600	878.85	-14.48	0.598	-19.95
19	420	3600	132.18	-16.30	0.068	-21.91
20	380	7200	58.28	-17.79	0.051	-22.86
21	410	3600	73.50	-16.86	0.051	-22.14
22	440	3600	176.81	-15.96	0.162	-20.93
23	470	3600	352.92	-15.23	0.437	-19.79
24	425	3600	78.47	-16.70	0.064	-21.61
25	385	7200	34.52	-18.21	0.033	-22.94
26	415	3600	48.77	-17.16	0.043	-21.97
27	445	3600	112.10	-16.32	0.112	-20.98
28	475	3600	253.89	-15.48	0.372	-19.7
29	500	1800	234.29	-14.83	0.370	-18.89
30	600	1800	1815.28	-12.64	5.850	-15.46
31	700	1800	3640.43	-11.59	17.255	-13.23
32	799	1800	4525.91	-10.86	21.572	-12.13
33	750	3600	1158.28	-12.56	4.050	-14.1
34	650	7200	160.91	-15.13	0.489	-16.85
35	550	10800	18.09	-17.71	0.047	-19.59
36	800	3600	1339.79	-12.2	6.548	-13.46
37	900	1800	1789.34	-10.94	12.343	-11.88
38	1000	3600	3027.73	-10.46	32.957	-10.95
39	1100	1800	1051.66	-9.82	22.571	-9.61
40	1100	1800	216.13	-10.69	3.482	-10.61
41	1150	1800	186.90	-10.36	5.190	-9.24
42	1150	3600	93.02	-11.22	1.131	---
43	1200	1800	58.62	-10.51	<DL	---
44	1250	1800	94.59	---	<DL	---

* D/a^2 values provided were calculated with equation for fractional loss from a spherical diffusion domain (Fechtig and Kalbitzer, 1966).

(Mouat, 1962). EPMA analyses of Priceless Mine sample material are consistent with these findings (table A3). EPMA-measured compositions from this sample fall near the

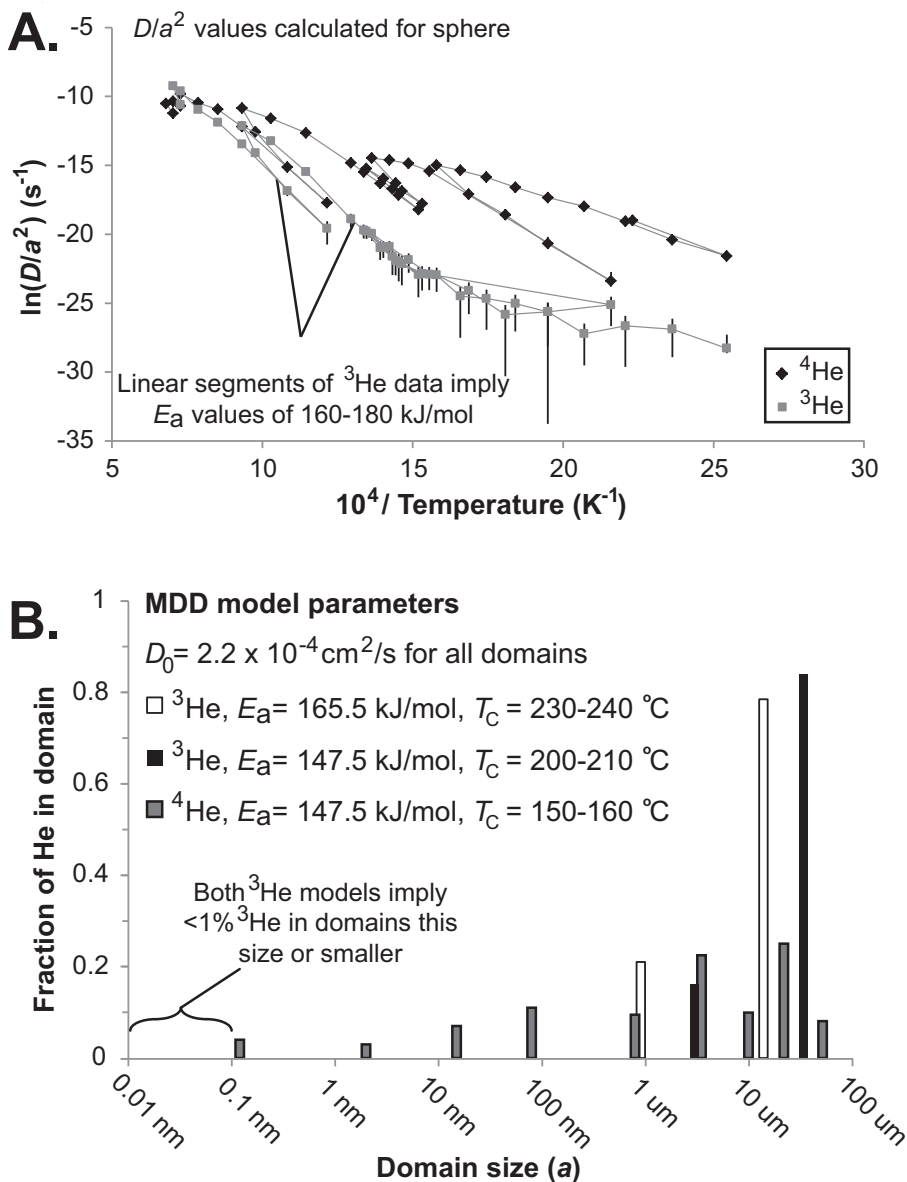


Fig. 8. (A) Arrhenius plot of ^4He and ^3He diffusion data from a single fragment of a hematite crystal from sample FW2-12-85-8. Error bars represent 2σ uncertainty. Sub-linear segments of the ^3He Arrhenius trend imply E_a values of 160–180 kJ/mol. ^4He data plot at higher apparent diffusivities [$\ln(D/a^2)$ values] than ^3He data at lower temperatures, but converge with ^3He data at higher temperatures. (B) Plot of the distribution of ^3He and ^4He among domains of different sizes implied by multiple domain diffusion (MDD) models of the data shown in (A). Each set of shaded bars represents the output of a MDD model fit to observed diffusion data (Arrhenius plots of each model are shown in figs. A3A–A3C). The lower E_a value used in these models is from data in figure 7, the higher value is from data in (A). The D_0 value is derived in the Discussion. Each bar represents a single modeled domain. The position of each bar along the x-axis represents the modeled domain size (a value), the bar height represents the fraction of total He contained in that domain. Models of ^3He data (white and black bars) suggest that most of the sample comprises domains with $a = 14\text{--}34\ \mu\text{m}$, with a very small volume of sub-nm scale domain. The model of ^4He data (gray bars) suggests that a large fraction of radiogenic He (35%) is held in domains with $a < 1\ \mu\text{m}$. This mismatch may be a result of heterogeneous distribution of ^4He throughout the sample. Listed T_c ranges are approximate bulk closure temperatures of a sample with the modeled distribution of ^4He (assuming $80\ \text{C}/\text{Myr}$ cooling rate, Scott and others, 1998).

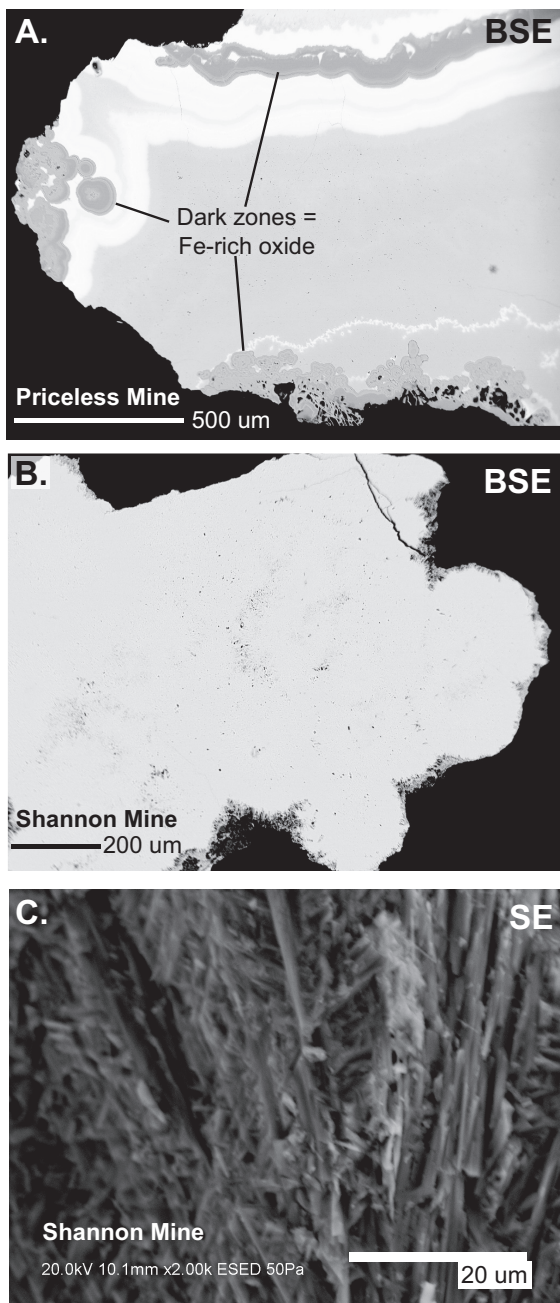


Fig. 9. SEM images of Mn oxide samples analyzed in this study. Material in images is representative of material in analyzed aliquots. (A) BSE image of polished Priceless Mine hollandite-coronadite, showing compositional banding. Dark gray material is a Fe-rich Mn oxide. Bright bands have a coronadite-rich composition (high Pb/Ba ratio). (B) BSE image of polished Shannon Mine hollandite. No compositional banding apparent. (C) Secondary electron, high-magnification (2000 \times) image of unpolished Shannon Mine hollandite, showing blade-shaped crystals $\sim 0.1\text{--}1\ \mu\text{m}$ thick.

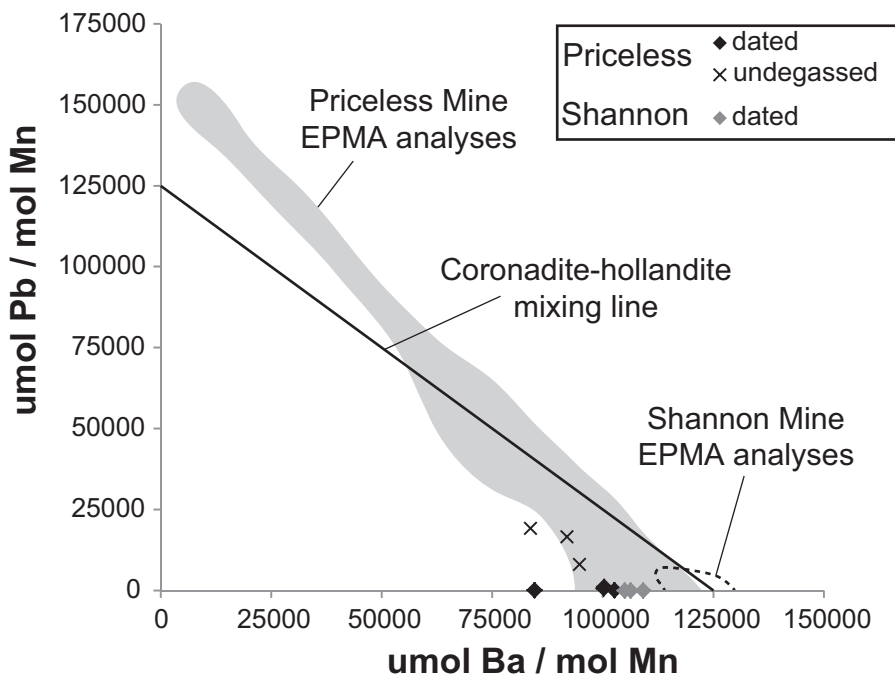


Fig. 10. EPMA point chemistry and ICPMS analyses of dated and undegassed aliquots of Mn oxide samples. Dated aliquots from each sample shown as solid diamonds, undegassed Priceless Mine aliquots as "X" symbols. Compositions of most dated and undegassed aliquots from the Priceless Mine sample overlap with EPMA analyses, compositions from both groups fall beneath pure hollandite-coronadite mixing line. Dated Priceless Mine aliquots contain less Pb than undegassed aliquots. Shannon Mine samples display slightly lower Ba contents than measured in EPMA analyses, which plot as pure hollandite.

mixing line (fig. 10) between hollandite ($\text{Ba}(\text{Mn}_6^{4+}\text{Mn}_2^{3+})\text{O}_{16}$) and coronadite ($\text{Pb}(\text{Mn}_6^{4+}\text{Mn}_2^{3+})\text{O}_{16}$; Post, 1999). EPMA analyses from several pieces of Shannon Mine sample material yield a pure hollandite composition, a result consistent with the lack of any apparent variation in composition in this sample (table A3, fig. 9B). Representative EPMA analyses of each phase present in Mn oxide samples are provided in table 9.

(U-Th)/He analyses and bulk-aliquot chemical compositions.—The Priceless Mine sample, taken from the Chapin Wash Formation, yields dates of 15.7 to 11.8 Ma (table 4). The Shannon Mine sample, taken from the overlying Sandtrap Conglomerate, yields dates of 8.5 to 7.6 Ma. Dated Priceless Mine sample aliquots yielded eU molar ratios greater than or equal to those measured in undegassed aliquots (table A2). On a plot of Pb/Mn versus Ba/Mn ratios (fig. 10), compositions of most dated and undegassed aliquots of Mn oxide overlap with those obtained from EPMA analysis.

DISCUSSION

Helium Diffusion in Analyzed Phases

Hematite He diffusion kinetics.—As in most minerals, the lengthscale of the He diffusion domain in hematite appears to scale with the physical crystal or grain size (Bahr and others, 1994; Farley and Flowers, 2012). In polycrystalline hematite samples analyzed in this study, the size of hematite crystals varies by one to two orders of magnitude within each sample. The bulk He retentivity of these samples may be best

TABLE 9
Representative electron microprobe analyses of Mn oxide minerals

	Priceless Mine		Shannon Mine
	hollandite	coronadite	hollandite
	wt%	wt%	wt%
Mn	48.11	41.74	49.04
K	0.08	0.02	0.08
Pb	0.69	24.09	0.04
Ca	0.16	0.15	0.22
Ba	13.81	0.73	14.83
Cu	0.08	0.27	0.08
Zn	0.94	1.77	0.23
As	0.30	0.39	0.35
Sr	0.85	0.03	0.63
O	30.26	26.95	30.70
Total	95.28	96.14	96.20

described by a “poly-domain” model. We use the term “poly-domain” when referring to He diffusion from polycrystalline aggregates. In such samples where a range of crystal sizes are present, it may be expected that multiple domains inferred from diffusion data may correspond to diffusion from crystals of different sizes (Farley and Flowers, 2012). We use “poly-domain” instead of “multi-domain” with the rationale that the latter would describe diffusion from multiple domains contained within what appears to be a single crystal or crystal fragment. He diffusion is typically modeled using the Arrhenius equation (eq. 1):

$$\frac{D}{a^2} = \frac{D_0}{a^2} e^{\left(\frac{E_a}{RT}\right)} \quad (1)$$

where D = diffusivity, a = the diffusion domain lengthscale (which we often refer to as domain size), T = temperature, R = the gas constant, E_a = activation energy, and D_0 = frequency factor. Bahr and others (1994) first proposed the idea that the size of diffusion domains scaled with physical crystal or grain size in hematite, so that crystal or grain size may be an important control on the effective bulk He retentivity of hematite samples. Farley and Flowers (2012) showed that results of step-heating ^3He diffusion experiments on a polycrystalline hematite sample were consistent with the presence of multiple diffusion domains that display constant E_a , but with D_0/a^2 values that vary over 20 to 30 natural log units. Based on comparisons between their step heating diffusion results and crystal size variation observed in SEM images of their sample, Farley and Flowers (2012) speculated that crystallite sizes (r values, in μm) observed in a sample may correspond directly to diffusion domain sizes (a values), while D_0 and E_a are constant across these domains. If this is correct and applies to all hematite, then we can substitute D_0/r^2 for D_0/a^2 in equation 1. This substitution and natural log transformation yields equation 2:

$$\ln\left(\frac{D}{a^2}\right) = \ln\left(\frac{1}{r^2}\right) + \ln(D_0) - \frac{E_a}{RT} \quad (2)$$

For a dataset containing D/a^2 values taken at one temperature from multiple hematite samples, the $(-E_a/RT)$ and $\ln(D_0)$ terms in equation 2 are constants. A plot of the

natural log of these apparent diffusivity values versus the natural log of the inverse square of the physical crystal or grain size ($1/r^2$) that each diffusivity value corresponds to should yield a linear relationship.

To test this idea, we compiled apparent He diffusivities (D/a^2 values) at 350 °C and estimates of corresponding crystal size data (r values, equal to half widths or radii of crystals or crystal fragments) from hematite diffusion experiments in several previous studies (table 10). In datasets where no pronounced poly-domain or multi-domain diffusion behavior was evident, we calculated D/a^2 values by interpolating the Arrhenius trend between two data points or by extrapolating the trend (whichever was necessary to obtain a D/a^2 value at 350 °C). In datasets from samples described by other authors as polycrystalline aggregates where He diffusion from multiple domains was apparent (poly-domain diffusion), we obtained D/a^2 values by extrapolating single-domain lines fit to sub-linear segments of the Arrhenius trend in the early, low-T part of the dataset, and used the smallest crystal size identified in the sample when assigning r values to these D/a^2 values. We obtain data points from ^3He diffusion data of Farley and Flowers (2012) as explained in figure A4. Figure 11 shows the data from table 10 in a plot of $\ln(D/a^2)$ at 350 °C versus $\ln(1/r^2)$. A line fit to the linear array that these data form has a slope of 0.817 ± 0.10 ($R^2 = 0.90$, 1σ error). Broadly speaking, this relationship is consistent with correspondence of diffusion domain size and crystal size, and a restricted range of E_a and D_0 for He in hematite. Similar relationships have been observed in the titanite and apatite (U-Th)/He systems (Reiners and Farley, 1999; Farley, 2000). This is consistent with the findings of Farley and Flowers (2012).

If the value of E_a for He diffusion in hematite is known or estimated, then we can use this value and the y-axis intercept of the linear relationship in figure 11 to calculate an estimate of D_0 (eq. 2). Published E_a values for He diffusion in hematite range from ~120 to 180 kJ/mol (Lippolt and others, 1993; Wernicke and Lippolt, 1994; Bahr and others, 1994; Farley and Flowers, 2012). Farley and Flowers (2012) used ^3He diffusion data to obtain $E_a = 157 \pm 6$ kJ/mol. We suspect that many of the smaller values of E_a from ^4He data in earlier studies (Lippolt and others, 1993; Wernicke and Lippolt, 1994; Bahr and others, 1994) may be a result of the contribution of He from multiple domains to early steps of the diffusion experiments from which E_a estimates are calculated (Lovera and others, 1997). Examples of this can be seen in the convex-up shapes formed by low-temperature steps in some Arrhenius trends from Bahr and others (1994). Sub-linear segments of the ^3He Arrhenius trend from sample FW2-12-85-8 yield $E_a = 160$ to 180 kJ/mol (fig. 8A), slightly higher than those obtained by Farley and Flowers (2012). We note that this sample is texturally distinct from other samples analyzed in this study and the sample that Farley and Flowers (2012) examined in that it comprises an apparent single crystal fragment. Therefore, this sample may yield somewhat different kinetic parameters (fig. 2A). Sub-linear segments of low-T portions of the Arrhenius trend from sample FW11-29-11-1 in this study yield $E_a = 147$ and 148 kJ/mol (fig. 7). Because these values are similar to the value obtained by Farley and Flowers (2012), and are derived from a sample that is texturally similar to most other samples examined in this study, we shall proceed using the average of these two values as our assumed E_a value ($E_a = 147.5$ kJ/mol).

Using this E_a value, the fixed T value for the dataset (350 °C), and the intercept of the best-fit line (dashed, fig. 11), we calculate a $\ln(D_0) = -5.3 \pm 2.0$ (1σ error estimate from uncertainty on intercept; eq. 2). This yields a D_0 value of 5.2×10^{-3} cm²/s ($+3.3 \times 10^{-2}/-4.5 \times 10^{-3}$ cm²/s). We note that the line used to calculate this value has a slope of less than the expected value of one (eq. 2), therefore, we fit another line with a fixed slope of one to the data (solid line, fig. 11). This line is only a slightly poorer fit to the data than the best fit line ($R^2 = 0.85$, best fit $R^2 = 0.90$). Following the above calculation, the intercept of this slope = 1 line yields a D_0 value of 2.2×10^{-4}

TABLE 10
D/a² and r values compiled from previous studies He diffusion in hematite

Reference	D/a^2 (s ⁻¹) at 350 °C	Crystal radius (<i>r</i> , μm)	Notes about D/a^2 , crystal radius values	$\ln(D/a^2)$	$\ln(1/r^2)$
Lippolt and others, 1993	1.2×10^{-11}	60	Sample is crushed/sieved fragments of larger crystals. D/a^2 extrapolated between two nearest-T steps of a single set of step heating results.	-25.1	10.2
Lippolt and others, 1993	8.7×10^{-13}	200	Sample is crushed/sieved fragments of larger crystals. D/a^2 extrapolated between two nearest-T steps of a single set of step heating results.	-27.8	7.8
This study	4.2×10^{-9}	0.5	D/a^2 taken from sublinear segment of Arrhenius plot of data from FW11-29-11-1. Calculated assuming plane sheet domain geometry. Assigned minimum observed crystal half-width.	-19.3	19.8
This study	1.4×10^{-11}	80	D/a^2 extrapolated from linear regression of sublinear segment on Arrhenius plot of data from FW2-12-85-5 (steps 25-31, table 8).	-25.0	9.7
Farley and Flowers, 2012	1.7×10^{-10}	3	Mean D/a^2 for largest domain represented in ³ He data from step heating of several aliquots of subsample A1, see figure A4 below. Assigned upper end of observed crystal radius range.	-22.5	16.2
Farley and Flowers, 2012	3.4×10^{-2}	0.0015	Mean D/a^2 for smallest domain represented in ³ He data from step heating of several aliquots of subsample A1, see figure A4 below. Assigned lower end of observed crystal radius range.	-3.4	31.4
Bahr and others, 1994	2.0×10^{-6}	0.01	D/a^2 value taken from single domain line fit to data from low-T steps from all botryoidal hematite samples examined in Bahr and others (1994, their fig. 9). Assigned <i>r</i> value based on SEM image of crystals in botryoidal hematite sample.	-13.1	27.6
Bahr and others, 1994	1.0×10^{-7}	0.05	D/a^2 value taken from single-domain line fit to low-T steps of a single step heating trial run on an aliquot of <10 μm size fraction crushed Rimbach specular hematite. Assigned half of smallest "grain size" identified in this sample, <0.1 μm.	-16.1	24.4
Bahr and others, 1994	5.6×10^{-11}	110	D/a^2 taken from single-domain line fit to Arrhenius plot of data from the Schneisenschlag specular hematite.	-23.6	9.0

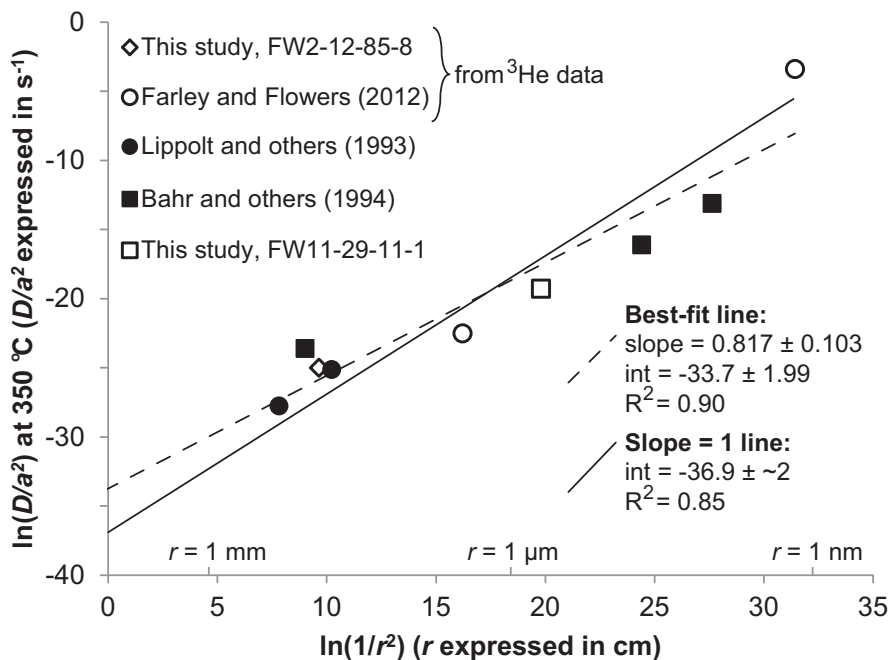


Fig. 11. Plot of natural log-transformed apparent diffusivity at 350 °C versus natural log-transformed inverse square of observed hematite crystal or grain radius or half-width. The inner part of the x-axis shows the equivalent crystal or fragment radii for several $\ln(1/r^2)$ values. Lower values of $\ln(1/r^2)$ correspond to larger crystal or grain radii. Points on this plot were taken from data in this study and other studies, references and data shown on the plot and in table 10. Open symbols represent data taken from this study and Farley and Flowers (2012), filled symbols are from older studies. Several of the open data points are derived from ^3He diffusion data, as shown on the plot. This figure shows that there is a direct relationship between D/a^2 and $1/r^2$, which supports the argument that crystal or grain size corresponds to diffusion domain size, and diffusion domain size is the primary control on D/a^2 variation at a given temperature. The best-fit line for these data has a slope slightly lower than expected, and its intercept implies a D_0 value of $5.2 \times 10^{-3} \text{ cm}^2/\text{s}$ (1σ error: $+3.3 \times 10^{-2}/-4.5 \times 10^{-3} \text{ cm}^2/\text{s}$). A line with the expected slope of one (see eq. 2 in text) provides a similarly good fit to these data, and implies a lower D_0 value of $2.2 \times 10^{-4} \text{ cm}^2/\text{s}$ (1σ error: $+1.6 \times 10^{-3}/-1.9 \times 10^{-4}$). We note the large uncertainty on these values, but consider the latter value as our best estimate of D_0 in hematite.

cm^2/s ($+1.6 \times 10^{-3}/-1.9 \times 10^{-4}$). As this value is calculated from a line that is fit to the data while also matching the form expected from equation 2, we favor it over the higher value obtained from the best fit line. We recognize that this value of D_0 bears a large uncertainty, but for the purposes of this study, we suggest that it is the best available estimate.

Hematite He diffusion data from this study.—The size of the smallest domain calculated from the FW11-29-11-1 diffusion experiment using hematite E_a and D_0 values determined in this study and an assumed plane sheet domain geometry ($r = 1.3 \mu\text{m}$, from P1 segment in fig. 7B) is consistent with the smallest observed crystal size in this sample (table 1, fig. 2D). This match between calculated diffusion domain size and physical crystal size observations is consistent with the findings of the compilation of diffusion data described above, and with the hypothesis that crystal size is a primary factor controlling He diffusivity in hematite (Farley and Flowers, 2012).

$^4\text{He}/^3\text{He}$ diffusion data from sample FW2-12-85-8 indicate that domains smaller than the observed sample chip size may be present within the sample. Because there are no clearly visible internal structures within the aliquot itself, or other crystals of this

sample examined in SEM, we hypothesized that this sample held all He that it contained in a single large diffusion domain, with an a value approximately equal to $r = 80 \mu\text{m}$ (the observed minimum half width of the sample chip).

The results of MDD modeling of diffusion data from sample FW2-12-85-8 (using kinetic values discussed above) suggest that >99 percent of the ^3He in the sample was released from domains with a values of ~ 1 to $34 \mu\text{m}$, with about 80 percent from domains with a values of ~ 14 to $34 \mu\text{m}$ (figs. A3A-A3B). These inferred a values are lower than the observed half width (r value), but given the uncertainties on E_a and particularly D_0 , a difference between the a values obtained from MDD models and the measured crystal fragment radius of less than one order of magnitude is not unreasonable, and thus these data could be cited in support of the inferred relationship between observed crystal size and diffusion domain size (Farley and Flowers, 2012).

To summarize the ^3He diffusion results, our interpretations from sample FW2-12-85-8 suggest that He diffusion occurs from domains similar to but slightly smaller than the observed crystal size. Although in detail this contradicts the findings of our compilation of diffusion data, and of Farley and Flowers (2012), we note that the ^3He diffusion results imply that the majority of the ^3He resides in a domain with a size that is of the same order of magnitude as the bulk crystal fragment size (fig. A3). Thus, if the observed crystal or grain size/s and diffusion domain size/s inferred from diffusion data are not identical, they may scale to first order.

The ^4He diffusion data from sample FW2-12-85-8 suggest that radiogenic ^4He has a significantly lower bulk retentivity than ^3He in this sample. If this arises entirely from effective diffusion domain size differences, then our modeling suggests that significantly more of the radiogenic ^4He than ^3He is held in the small domains; more specifically, about 35 to 40 percent of the ^4He is in domains with $a < 1 \mu\text{m}$ (figs. 8 and A3C-A3D). We hypothesize that this difference between the ^4He and ^3He diffusion behavior arises from a spatial correlation between the source of ^4He (U and Th) and locations of the small domains, such that ^4He is preferentially implanted into smaller domains. We suggest that smaller domains of hematite and other phases that are eU-rich relative to surrounding hematite clustered together, perhaps surrounding cracks, inclusions, or other defects in the sample (fig. 12). These clusters will have a higher “domain surface area” per unit of sample volume and thus a potentially higher eU concentration than parts of the sample made up of larger diffusion domains of low-eU hematite (figs. 4A and 12B-C). In order for these clusters of smaller domains to capture a large fraction of the ^4He produced by the decay of U and Th that they contain, the half-width of the clusters must be greater than or equal to the alpha stopping distance in hematite (13-18 μm , Ketchum and others, 2011).

The $^4\text{He}/^3\text{He}$ diffusion data from sample FW2-12-85-8 may also be explained by models other than the one presented above. Radiation damage provides an alternative, though perhaps less likely explanation for the presence of very small, ^4He -rich diffusion domains in hematite. It is possible that alpha-recoil-induced radiation damage contributes to the reduction of effective diffusion domain size in parts of the sample where eU is concentrated.

Without additional data that replicate the kind of inconsistency observed between ^4He and ^3He diffusion data from FW2-12-85-8, we conclude that, for most hematite samples, crystal size is a primary control on He diffusivity in hematite. Therefore, the findings of the compilation of diffusion data obtained above (including the estimated value for D_0 in hematite) are also considered valid. Additional studies of He diffusion in hematite, which include a careful examination of hematite crystal structure in analyzed samples, are necessary to better understand this process.

In order to compare hematite (U-Th)/He dates obtained in this study with cooling dates from other studies of lower-plate cooling in the Buckskin-Rawhide

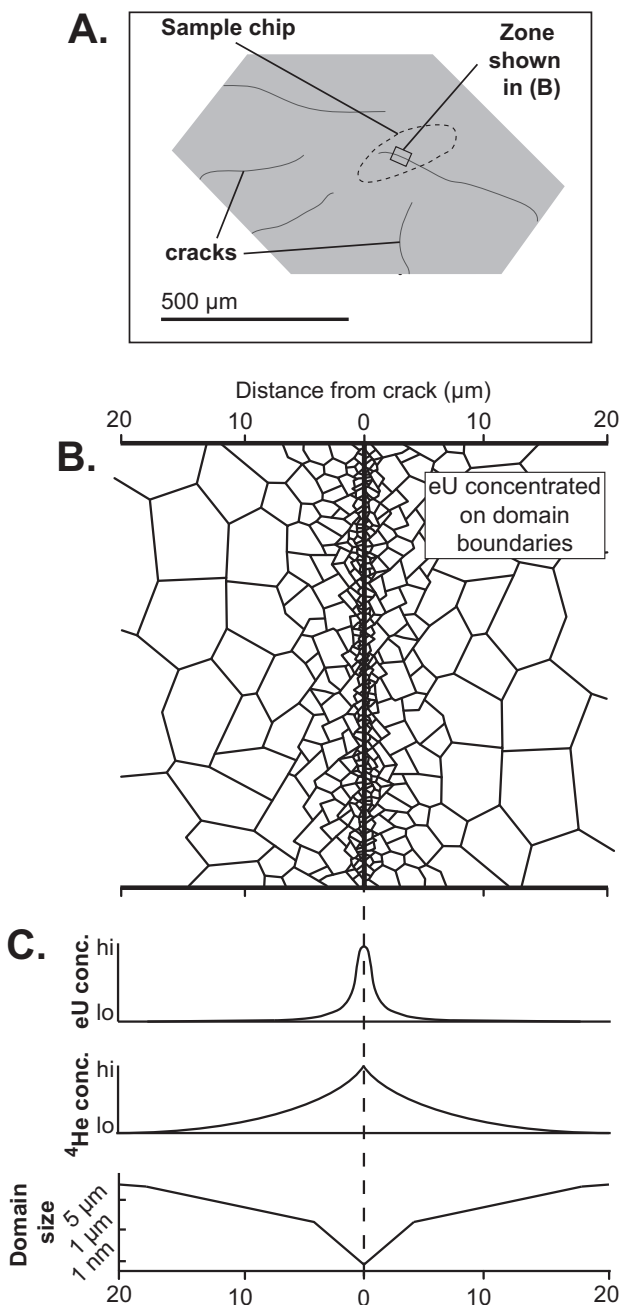


Fig. 12. Schematic illustration of the aliquot of hematite from sample FW2-12-85-8 analyzed in $^4\text{He}/^3\text{He}$ experiment. (A) Cross-section through a euhedral crystal showing the internal location of the analyzed sample chip, and the outline of the part of the chip that is illustrated in (B). (B) Cross-section through portion of analyzed hematite sample chip showing a hypothetical distribution of diffusion domains surrounding a central crack or other defect. (C) Curves showing hypothetical spatial distribution of eU, ^4He , and diffusion domain sizes within the cross-section shown in (B). The clustering of smaller domains of hematite and perhaps other, eU-rich phases along the crack results in a higher eU concentration in this zone. Ejection of some of the ^4He produced by decay of this eU into domains farther from the crack widens the zone of elevated ^4He concentration, but ^4He concentration is highest in the small domains surrounding the crack.

detachment system, we need to estimate the He closure temperature (T_c) of hematite samples. We use observed crystal half-width values as an estimate of diffusion domain radii (a values, see table 1), various domain geometries and cooling rates, and assumed diffusion kinetic values stated earlier in this subsection to calculate effective closure temperatures for the smallest and largest crystals observed in each hematite sample (Dodson, 1973; table 11). The cooling rate (80 °C/Myr) that we have applied above in calculating closure temperatures from He diffusion data (figs. 7 and 8) is taken from Scott and others (1998). Their study suggests that this rate was applicable to lower-plate cooling for much of the ~300 to 150 °C temperature window, the range in which previous estimates of He T_c in coarsely crystalline hematite fall (Lippolt and others, 1993; Bahr and others, 1994). We also include T_c estimates that incorporate the highest cooling rate cited by Scott and others (1998, 280 °C/Myr). Due to the plate-like or tabular shape of hematite crystals in most samples, we suggest that T_c ranges that assume plane sheet domain geometry provide better estimates. Closure temperature ranges that assume an 80 °C/Myr cooling rate and plane sheet domain geometry fall largely between 140 to 240 °C. Given the uncertainty in the E_a and D_0 values used to calculate these estimated T_c ranges, we do not attempt to calculate more precise bulk closure temperatures.

Results of the FW2-12-85-8 ⁴He/³He step-heating experiment suggest that the true closure temperature of this sample may be <180 °C. MDD models of ⁴He diffusion data from this sample imply a bulk closure temperature of ~150 to 180 °C (calculated for 80 °C/Myr cooling rate, spherical domain geometry, figs. 8B, A3C-A3D), much lower than closure temperature estimates based on crystal size (table 11). We have no clear evidence that the mismatch between observed crystal size and ⁴He diffusion domain size inferred from MDD models (fig. 8) of data from this sample extends to other hematite samples, which are made up of crystals that are much smaller, contain fewer inclusions, and are plate-shaped rather than rhombohedral (fig. 2).

He diffusion in Mn oxide.—Using kinetic parameters from previous studies of He diffusion in Mn oxide and estimates of crystal size from SEM images, we estimate that Mn oxide samples dated in this study have closure temperatures of ~36 to 57 °C. Lippolt and Hautmann (1995) performed a step-heating experiment on a microcrystalline sample of cryptomelane-hollandite composition. These phases have the same crystal structure as Mn oxide minerals identified in Shannon and Priceless Mine samples in this study (2×2 tunnel structure; Post, 1999), leading us to apply the He diffusion kinetic parameters from Lippolt and Hautmann (1995). Following the reasoning we applied to hematite samples, we assume that crystal size (in μm) is approximately equal to the diffusion domain lengthscale (a), and estimate $a = 0.1$ μm (a lower-end estimate of a , fig. 9; Farley and Flowers, 2012). Using the E_a and D_0 values calculated from the low temperature (<500 °C) steps of the diffusion experiment in Lippolt and Hautmann (1995; 134 kJ/mol and 3.981×10^{-3} cm²/s, respectively) and an assumption of spherical diffusion domain geometry, we calculate closure temperatures of 36, 49, and 57 °C for cooling rates of 10, 80, and 280 °C/Myr. These closure temperatures are consistent with the findings of Reiners and others (2014), who suggest that fine-grained Mn oxide of a similar composition and apparent crystal size will retain most of its He when exposed to temperatures of up to ~55 °C for several million years.

Assessment of Hematite (U-Th)/He and Compositional Data

(U-Th)/He dating of hematite samples in this study yields results that are consistent with estimates of the timing of active extension and mineralization in the Buckskin-Rawhide detachment system (Scott and others, 1998; Singleton and Stockli, 2013; Spencer and others, 2013).

TABLE 11
Estimated hematite sample closure temperature ranges (°C)

Cooling rate	Spherical domains		Plane-sheet domains	
	80 °C/Myr	280 °C/Myr	80 °C/Myr	280 °C/Myr
FW2-12-85-8*	296-321*	319-345*	330-357*	355-385*
FW3-23-85-8	128-231	139-249	144-258	156-277
FW3-21-85-12	116-196	126-212	132-219	143-236
FW11-29-11-1	128-196	139-212	144-219	156-236
HW1-16-12-1	128-213	139-230	144-238	156-256
HW11-30-11-3	116-221	126-237	132-246	143-264

* $^4\text{He}/^3\text{He}$ diffusion data suggest that closure temperatures for this sample may be well below those listed here, with a bulk T_c of <250 °C.

All closure temperatures calculated from minimum and maximum crystal half-widths observed in each sample, assuming $E_a = 147.5$ kJ/mol and $D_0 = 2.2 \times 10^{-4}$ cm²/s.

Possible causes of date dispersion in hematite samples.—Systematic relationships among (U-Th)/He date, aliquot type, pre-treatment, and the molar ratios of eU and other elements (noted in the Results section above) lead us to a discussion of the causes of date dispersion in these samples. Thermal histories obtained by Scott and others (1998) suggest that lower-plate rocks in the Buckskin Mountains cooled through the estimated range of He closure temperatures in hematite (140-240 °C, table 11) over a relatively short period of time (~ 1 Myr). This period of time is less than the variation in (U-Th)/He dates observed in aliquots from each hematite sample (fig. 3). The textural homogeneity of hematite crystals in most samples (euhedral, formed early in the paragenetic sequence—see table 1, fig. 2) leads us to infer that hematite formation, like cooling, occurred over less than 2 Myr. If these inferences are correct, then variations in the formation age or closure temperature of hematite crystals within a single sample are not likely to be the causes of (U-Th)/He date dispersion observed in some samples.

In several hematite samples, cleaned aliquots, particularly those made up of hematite crystals alone (PO aliquots), yielded lower molar ratios of Mg, Mn, and eU (figs. 4C-4E and fig. 5). We interpret the difference between cleaned and NC aliquot compositions in these samples to reflect disaggregation and removal of interstitial phases from hematite-rich parts of the sample material during ultrasonic cleaning. EPMA analyses of common interstitial phases yield higher molar ratios of Mg and Mn than hematite crystals, supporting this assertion (tables 2 and 3). Analyses of chrysocolla from sample FW3-23-85-8 indicate that this phase contains a large amount of U (table 5); we note that aliquots of the two hematite samples that contain chrysocolla (samples FW3-23-85-8 and FW3-21-85-12, figs. A1 and A2) also yield the highest eU molar ratios observed among all samples (fig. 4). While we did not obtain direct measurements of the U and Th contents of other common interstitial phases, it is plausible that some of these phases (chlorite, calcite) also display a high molar ratio of U and/or Th relative to hematite.

Removal of parent nuclides during ultrasonic cleaning has a clear effect on the (U-Th)/He dates obtained from cleaned aliquots. As a result of the long stopping distance of radiogenic ^4He atoms (13-18 μm in hematite, ~ 20 -25 μm in less dense interstitial phases; Ketchum and others, 2011), much of the ^4He produced by decay of U and Th in interstitial phases is likely to be implanted in neighboring hematite crystals and retained over geologic time. The loss of parent nuclides contained in these interstitial phases following a long (several Myr) period of He implantation will result in an increase in the (U-Th)/He dates obtained from the surrounding sample

material. If this removed parent material was added to a sample at a near-zero date, it is possible that the resulting apparent (U-Th)/He dates obtained from the sample will be approximately equal to its true He closure age. We find little geologic or textural evidence for late addition of U or Th (via uptake on mineral surfaces or incorporation into growing interstitial phases) to hematite samples. We therefore interpret the observation that cleaned aliquots tend to yield older ages than NC aliquots (fig. 3) as an artifact of interstitial phase removal and accompanying parent nuclide loss. Under this interpretation, cleaned aliquots yield apparent (U-Th)/He dates that are older than the true He closure age, and NC aliquots (which contain a greater fraction of 'initial' U and Th) provide the best estimate of He closure age. The inverse relationships observed between (U-Th)/He date and the molar ratios of eU and other elements in some samples (figs. 4C-4E and fig. 5) can also be attributed in part to parent nuclide loss.

In cases where large accumulations of eU-rich interstitial phases are present in analyzed sample material, ^4He loss from these phases may also contribute to the observed inverse relationships between date and eU or other elements. The fraction of ^4He produced in a given body of interstitial material that is implanted in neighboring hematite crystals is inversely related to the width of the space between hematite crystals, and directly related to the alpha stopping distance in interstitial phases. Working under the simplifying assumptions of parallel orientation of hematite crystals and a uniform alpha stopping distance of 25 μm in interstitial phases, we estimate that >10 percent of ^4He produced in interstitial phases that fill large spaces (>10 μm wide) between platy hematite crystals will not be implanted into hematite (fig. A5). This fraction increases rapidly as the spacing of neighboring hematite crystals rises. Given the high He diffusivities of common interstitial phases such as calcite (Cros and others, 2014), quartz (Shuster and Farley, 2005b), and chrysocolla (which displays an amorphous structure analogous to glass and is therefore unlikely to retain He; Shelby, 1972; Jambon and Shelby, 1980; Frost and Yi, 2013), it is likely that most ^4He that is not implanted in hematite will be lost over million-year timescales. Among all samples, four aliquots yield apparent (U-Th)/He dates younger than the cessation of extension along the detachment fault (estimated at ~ 8 Ma, see Geologic Setting). Of these aliquots, two from sample FW3-23-85-8 yield high molar ratios of eU (fig. 4B), Mg (fig. 5A), and Ca (table A2) and low Th/U ratios (table 4), all characteristics that support the presence of a relatively high volume fraction of chrysocolla in these aliquots (tables 3, 5). The 5.8 Ma aliquot from sample FW11-29-11-1 displays similar characteristics relative to other aliquots in that sample. We suggest that young dates obtained from these aliquots result from the loss of large fractions (30-50%) of ^4He produced in 10 to 50 μm -scale pockets of highly eU-enriched chrysocolla and/or chlorite, that was not implanted in neighboring hematite crystals (fig. A1). We exclude the dates of these <8 Ma aliquots from further consideration (noted as 'discarded' in table 4).

In the two preceding paragraphs, we discussed ways that interstitial phases (and the removal thereof) can contribute to inverse relationships between date and the molar ratio of eU and other elements. It is possible that volatilization of parent nuclides during He extraction may also contribute to these relationships. During high temperature He extraction, parent nuclides and other elements may be volatilized and lost from the sample. The difference in the molar ratios of Cu and Pb between undegassed (not heated to high temperatures) and dated hematite aliquots indicate that these elements are volatilized during He extraction (fig. 6). In contrast, the molar ratios of Mg (figs. 5A-5B) and Ca (table A2) measured in most dated aliquots are consistent with those measured in undegassed aliquots and greater than or equal to those measured in hematite alone (table A1), which suggests that these elements are typically retained through the degassing process. These observations are consistent

with relative volatilities of these elements (Larimer and Anders, 1967; Lamoreaux and others, 1987; Lodders, 2003). In these studies, both Th and U are found to be nearly as refractory as Mg and Ca. Based on this information and the data presented above, we suggest that U volatilization does not have a large effect on most dated aliquots, and that the effects of cleaning on (U-Th)/He dates of aliquots (as manifested in inverse relationships between date and element molar ratio) are typically of a greater magnitude than volatilization.

A few aliquots display characteristics that we interpret as signs of the loss of large fractions of parent nuclides. Three aliquots (from samples FW3-23-85-8 and FW2-12-85-8) yield dates that are older than the earliest radiometric date of detachment activity (26 Ma; Lucchitta and Suneson, 1993), along with low molar ratios of eU (figs. 4B-4C) and Mg (below the minimum molar ratio in hematite crystals; tables 2 and 4) and high Th/U ratios (a sign of U volatilization identified by Danišik and others, 2013 and Vasconcelos and others, 2013, table 4). It is difficult to determine the extent to which these aliquots were affected by volatilization; however, the low Mg molar ratio in these aliquots might imply that refractory elements (including U and/or Th) have been lost. Evidence of inclusions was observed in sample FW2-12-85-8 (fig. 2A, table 1). Inclusions in analyzed aliquots of this sample may have contained ^4He present at the time of sample formation, which would result in older (U-Th)/He ages. Whether physical removal of interstitial phases, volatilization, or the presence of ^4He in inclusions has had a larger effect on the measured dates of these aliquots, it seems that some parent material has been lost. We use the characteristics that these too-old aliquots display to identify several other aliquots that, despite yielding geologically reasonable ages (<26 Ma), are also believed to have also been affected by parent nuclide loss (induced by either cleaning or volatilization) to a large extent. We exclude the dates obtained from these aliquots (six in total) from consideration when interpreting the significance of hematite dates, and mark them as discarded in table 4.

This discussion has implications for future studies that utilize hematite (U-Th)/He dating. Results from cleaned hematite aliquots analyzed in this study illustrate how the use of ultrasonic cleaning or any other pre-treatment meant to remove U and Th sited outside of the hematite crystal lattice (for example, dissolution of phases other than the target phase, Fanale and Kulp, 1962) will produce the desired result (a date closer to the age of He closure/mineral formation) only in cases where removed U and Th was added very recently. It is more probable that cleaned samples will yield too-old ages that contribute to age dispersion (see Orme, ms, 2011 and Murray and others, 2014 for an exploration of an analogous problem in the apatite (U-Th)/He system). Such an outcome is especially likely in cases where the fraction of eU in phases vulnerable to removal is greater than that contained in hematite. In future studies, pre-treatments that aim to remove extra-hematite-lattice parent nuclides should be used carefully, and several aliquots from each dated sample should be excluded from cleaning and/or other pre-treatments to control for their effects.

Two hematite samples analyzed in this study do not display date-element relationships, and yield overlapping cleaned and NC dates (figs. 3 and 4A-4B). We attribute these characteristics to the relative scarcity of interstitial phases in these samples (figs. 2A and 2D), which may in turn indicate that eU is held within hematite crystals in these samples, where it is not easily removed by ultrasonic cleaning or other physical processes. As a result, there is less potential for eU loss during cleaning or other sample preparation procedures, and a higher likelihood that He produced by decay of eU within each aliquot is implanted into He-retentive hematite crystals.

Assessment of Mn oxide (U-Th)/He and compositional data.—(U-Th)/He dates from Mn oxide samples are compatible with the inferred ages of sedimentary units that are cross-cut by host veins. The oldest (U-Th)/He date from the Priceless Mine sample

(15.7 Ma) is younger than the maximum depositional age of the host Chapin Wash Formation (~18.5–16.2 Ma). The oldest of the Shannon Mine aliquots (8.5 Ma) is younger than the 9.6 to 9.5 Ma Manganese Mesa basalt, which underlies the sampled part of the Sandtrap Conglomerate at the Shannon Mine locality (Shafiqullah and others, 1980; Shackelford, 1980).

Comparisons of undegassed and dated aliquot compositions suggest that He-extraction-induced eU loss has not affected dates obtained from Mn oxide samples. eU molar ratios measured in dated aliquots from the Priceless Mine sample are approximately equal to or greater than those obtained from undegassed aliquots. This comparison provides no evidence for loss of U or Th from dated aliquots of this sample. No undegassed aliquots from the Shannon Mine sample were analyzed; in lieu of these data, we extend our conclusion regarding an absence of eU loss from the Priceless Mine sample to this sample.

EPMA-measured compositions of Priceless Mine Mn oxide overlap with the ICPMS-measured compositions of dated and undegassed aliquots of this sample, but neither group of analyses plots precisely on the hollandite-coronadite mixing line (fig. 10). Volatilization of Pb during He extraction (as observed in hematite, fig. 6) might explain why most dated aliquots contain little or no Pb, and thus plot below the mixing line near the horizontal axis of figure 10. In the case of undegassed aliquots (which were never heated to high temperature prior to dissolution) and EPMA analyses, low Ba and Pb contents might be explained in part by the substitution of other elements for Ba and/or Pb (see table 9; Post, 1999), or the presence of phases other than Mn oxide in sample material. One such phase may be an Fe oxide (fig. 9A), the presence of which is supported by Fe/Mn molar ratios of 0.05 to 0.11 in Mn oxide from the Priceless Mine sample (table A2). The closure temperatures calculated for Mn oxide samples in the previous sub-section do not account for the presence of phases other than 2×2 tunnel-structure Mn oxides (Post, 1999). Given the similarity of closure temperatures calculated for fine-grained Mn and Fe oxides by Reiners and others (2014), we suggest that the T_c values calculated for Mn oxides in this study (~36–57 °C) remain a reasonable approximation of the actual T_c .

Comparison of hematite and Mn oxide (U-Th)/He dates to other radioisotopic dates of Buckskin-Rawhide detachment system activity.—Apart from the westernmost sample (FW3-23-85-8), mean dates of NC aliquots of hematite samples decrease from SW to NE (table 12, fig. 13). This is consistent with data from a number of other studies of footwall cooling in the study area (Foster and others, 1993; Scott and others, 1998; Brady, 2002). As discussed above, NC aliquots from FW3-23-85-8 appear to be prone to He loss from eU-rich interstitial phases with high He diffusivities, which may result in a shift to a younger mean sample date (fig. 13).

We interpret evidence from fluid inclusions to suggest that hematite samples record cooling. Textural evidence from this and other studies suggests that the timing of quartz formation immediately preceded or overlapped with hematite formation in hematite-bearing mineral deposits in the Buckskin Mountains and other nearby detachment-hosted ore deposits (Halfkenny and others, 1989; Schuiling, ms, 1978). Fluid inclusion data indicate that quartz in Buckskin-Rawhide hematite-bearing deposits formed at temperatures >225 to 325 °C (Wilkins and others, 1986). These temperatures fall at the upper end of the estimated hematite T_c range (140–240 °C, table 11). We interpret this evidence to indicate that hematite formed at a temperature greater than its closure temperature, and therefore, hematite (U-Th)/He dates should record cooling.

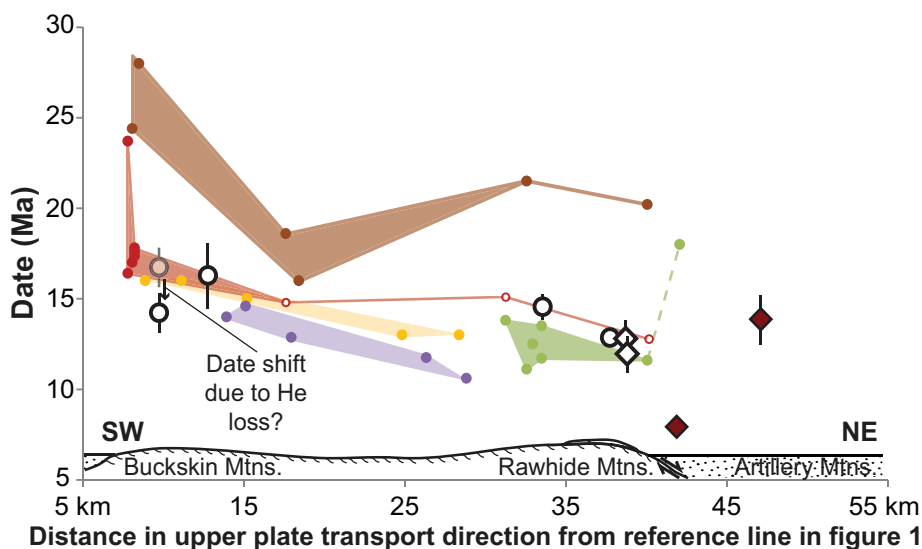
Hematite (U-Th)/He dates overlap with dates obtained from various thermochronometers in other studies of lower plate cooling in the Buckskin-Rawhide detachment system. In figure 13, hematite dates are plotted with dates from samples mapped in

TABLE 12
 Mean hematite and Mn oxide sample (U-Th)/He dates

Sample	Mean date $\pm 1\sigma$	
	Not cleaned	Cleaned
FW2-12-85-8	16.22 \pm 1.81	17.17 \pm 1.81
FW3-23-85-8	14.15 \pm 2.43	18.49 \pm 2.10
FW3-21-85-12	14.68 \pm 0.59	16.87 \pm 0.86
FW11-29-11-1	12.83 \pm 0.34	12.91 \pm 0.48
HW1-16-12-1	12.83 \pm 1.03	15.07 \pm 0.89
HW11-30-11-3	11.88 \pm 1.01	13.28 \pm 3.28
Priceless Mine	13.79 \pm 1.57	---
Shannon Mine	7.97 \pm 0.46	---

figure 1. In the western end of the study area, the mean date from sample FW2-12-85-8 (sample FW3-23-85-8 is excluded from consideration for reasons outlined in the first paragraph of this subsection) overlaps with biotite $^{40}\text{Ar}/^{39}\text{Ar}$ and $^{40}\text{K}/^{39}\text{Ar}$ dates [$T_c \approx 325\text{--}375$ °C, Harrison and others (1985); fig. 13], as well as apatite fission-track dates from nearby samples. The average dates from the group of hematite samples located near the eastern end of the study area fall more clearly below biotite K-Ar dates and overlap within analytical uncertainty with ZFT dates from nearby samples (ZFT 1 σ errors = 10-15%). While it is encouraging that hematite (U-Th)/He dates can replicate dates obtained from other studies of footwall cooling, the large amount of uncertainty on the hematite closure temperature and the small range of dates obtained from other thermochronometers make it difficult to use these data to test whether hematite dates record cooling or mineral formation.

Regardless of which process hematite dates record, we suggest that the decrease in mean hematite sample dates in the direction of upper-plate transport reflects the migration of isostatic uplift and exhumation of lower-plate rocks (fig. 14, see models presented in Spencer, 1984; Spencer and Reynolds, 1991). Our estimate of the depth of hematite formation is ~ 3 to 7 km, based on a >225 to 325 °C formation temperature estimate (Wilkins and others, 1986), and an elevated geothermal gradient in the upper crust during active extension (perhaps as high as ~ 50 to 100 °C/km, Scott and others, 1998). Following hematite (\pm quartz) formation, interstitial phases crystallized at shallower depths and lower temperatures (similar to the findings of, Schuiling, ms, 1978). Owing to rapid rates of exhumation evidenced by cooling rates documented in previous studies of the Buckskin-Rawhide detachment (Scott and others, 1998), lower-plate rocks were advected from depths of hematite formation to shallower depths in a short period of time (relative to the ages of hematite obtained in this study), and very little time elapsed between the formation at depth and the cooling of hematite samples through the estimated closure temperature range. Therefore, while it is difficult to be certain whether hematite dates from this system record cooling or formation (as noted in the previous paragraph), we suggest that the difference between hematite formation ages and the hematite cooling ages is very small (less than 2 million years, based on a cooling rate of 80 °C/Myr; Scott and others, 1998). Northeastward migration of the locus of isostatic uplift resulted in rocks that are now exposed in the Buckskin Mountains passing through the zones of hematite formation and cooling prior to those now exposed in the Rawhide Mountains, yielding the observed age-distance trend in hematite dates and in other thermochronometers (figs. 13 and 14B-14D). Hematite samples from the upper-plate yielded mean dates similar to those obtained from nearby lower-plate samples (table 12). We interpret this to



SYMBOLS		
Dates from this study:		
Hematite (U-Th)/He mean date $\pm 1\sigma$		lower plate
		upper plate
Mn oxide (U-Th)/He mean date $\pm 1\sigma$		upper plate
Dates from other studies (all from lower plate rocks):		
	sample date	polygon including all dates
Apatite (U-Th)/He		70-80 °C (Farley, 2000)
Apatite fission track		~110 °C (Gallagher and others, 1998)
Zircon fission track		250-300 °C (Rahn and others, 2004)
Biotite K-Ar		325-375 °C (Harrison and others, 1985)
Biotite Ar-Ar		
K-feldspar Ar-Ar age		Variable, likely >300° C

Fig. 13. Hematite (U-Th)/He dates and dates from other studies of lower-plate cooling, plotted against distance in slip direction. Sample locations and references for dates from other studies are shown in figure 1. The horizontal axis shows the distance of the sample location northeast of the dashed reference line on figure 1, measured in the upper-plate transport direction (N50E). A schematic cross section that shows the present day configuration of lower and upper-plate rocks is shown along the x-axis. Hematite and Mn oxide dates plotted here are mean NC aliquot dates from each sample (table 12). We estimate that the closure temperatures (T_c) of hematite samples analyzed in this study fall between 140–240 °C (table 11). The closure/annealing temperatures of the other thermochronometers in the plot (calculated for elevated cooling rates appropriate for lower-plate rocks) are shown below the plot. Error bars on dates from other studies excluded to reduce visual clutter. 1σ uncertainties on most of these dates are ~10–15% of date, except for AFT uncertainties, which are ~25% of date. All hematite dates (except for the westernmost, FW3-23-85-8) overlap with biotite $^{40}\text{Ar}/^{39}\text{Ar}$ / $^{40}\text{K}/^{39}\text{Ar}$ and ZFT dates from nearby samples, though these systems typically have higher T_c values than those estimated for hematite. The faded hematite data point above the westernmost hematite sample data point shows a hypothetical age for this sample if inferred He loss had not occurred.

indicate that the host rocks of these samples were transferred from the upper-plate to the lower-plate and were mineralized at the same time as nearby lower-plate samples.

The model of hematite mineralization presented in figure 14 is compatible with geologic constraints on the evolution of the Buckskin-Rawhide core complex established by previous studies. The timing of uplift and initial exposure of footwall rocks in the Buckskin Mountains implied by the presence of mylonitic debris in the upper Chapin Wash Formation (max depositional age = 18.5–16.2 Ma, minimum age uncertain, probably between ~14 and ~12 Ma, fig. 14C) is consistent with hematite dates on mineralization and rapid cooling that occurred during related lower-plate uplift (16–15 Ma, Spencer and Reynolds, 1989; Singleton and Stockli, 2013). Exposures of the Sandtrap Conglomerate northeast of the Rawhide Mountains contain abundant, locally derived clasts of lower-plate rocks (fig. 14D). This observation signals lower-plate exposure and the development of significant relief in the Rawhide Mountains prior to deposition of the Sandtrap Conglomerate (Spencer and others, 1989b; Yarnold, 1994). The depositional age of the Sandtrap Conglomerate (max depositional age uncertain), as implied by interbedding with 10 to 9 Ma Manganese Mesa basalt (Shafiqullah and others, 1980; Shackelford, 1980), is compatible with dates from hematite samples from lower-plate rocks in the Rawhide Mountains (14.5–12.8 Ma) that imply earlier lower plate uplift and mineralization in this area.

We speculate that Mn oxide dates represent the timing of vein formation in shallow hydrothermal settings. The relatively low closure temperature range (~36–57 °C, see *He diffusion in Mn Oxide* above for T_c estimation) estimated for these samples indicates that they are susceptible to resetting by heat from overlying volcanic rocks or hydrothermal sources. The thickness of younger Neogene and Quaternary sediments is negligible, thus, reheating related to reburial is not probable (Spencer and others, 1989b). Some younger dates obtained from the Priceless Mine sample may have been affected by partial resetting, possibly due to a heating pulse related to the Manganese Mesa basalt. Mn oxide from the Shannon Mine sample postdates the flows of this basalt unit (age ~9.5 Ma, Shafiqullah and others, 1980; Shackelford, 1980; Suneson and Lucchitta, 1983), therefore, we suggest that thermal resetting of the Shannon Mine sample is not likely, and that dates from this sample record Mn oxide formation.

These Mn oxide (U-Th)/He formation ages may provide a record of hydrothermal circulation through supra-detachment basin sediments driven by heat from buried portions of the detachment. Salinities and homogenization temperatures obtained from fluid inclusions in accessory phases in Mn oxide vein deposits (0–3 wt% NaCl equivalent, 165–170 °C; Spencer and others, 1989b; Spencer, 1991) are low relative to those observed in Fe oxide deposits (Wilkins and others, 1986). Based on this evidence, we speculate that the parent fluids of Mn oxide vein deposits are a mixture of deep-sourced, saline, hot fluids that transported heat from the detachment zone and shallow, cooler ground waters, which may have been enriched in Mn by interaction with detrital Mn deposits in the Chapin Wash Formation. If this proposed model is accurate, then the dates obtained from Mn oxide samples, particularly the younger sample from the Shannon Mine, provide evidence that buried lower-plate rocks continued to feed heat into the upper-plate hydrothermal system as extension along the detachment slowed, and perhaps after extension ceased at ~10 to 8 Ma.

CONCLUSIONS

A compilation of hematite He diffusion data from previous studies, along with ^4He diffusion data from a polycrystalline hematite aliquot, indicate that in general crystal size is a primary control on the He diffusivity of hematite (a finding consistent with Farley and Flowers, 2012). $^4\text{He}/^3\text{He}$ diffusion data from a large (~80 μm radius) fragment of a single hematite crystal are interpreted to indicate that about 80 percent of the ^3He in this aliquot is held within domains with a size of the same order of

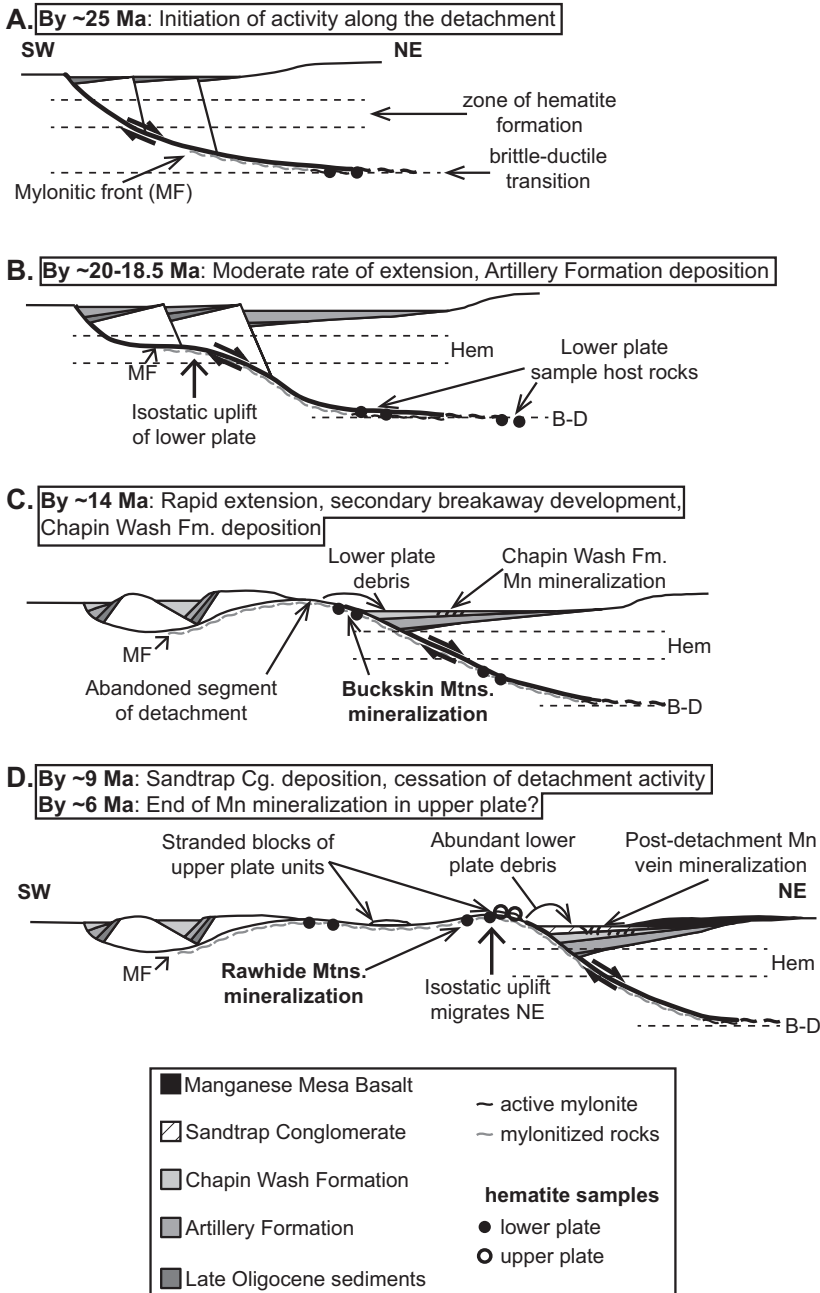


Fig. 14. Evolution of the Buckskin-Rawhide core complex and associated mineral deposits, shown in schematic cross-sections (modeled after Spencer and Reynolds, 1989). The approximate location of these sections is shown in figure 1. The approximate depth range of hematite formation in the detachment zone ("Hem", ~3–7 km) and the brittle-ductile transition ("B-D", ~12–15 km) are shown as dashed horizontal lines. Approximate locations of hematite sample host rocks are shown as filled and open circles. (A) Extension and supra-detachment basin development in the Buckskin-Rawhide detachment system began as early as ~26 Ma (Lucchitta and Suneson, 1993). (B) Before ~19 Ma, the rate of extension along the detachment was moderate. During this time, isostatic uplift of the footwall began. Deposition of the Artillery Formation and other age-equivalent strata occurred from ~26 Ma until ~18.5 Ma. (C) At ~19–18 Ma, the rate of extension increased

magnitude as the bulk crystal fragment. However, about 35 to 40 percent of ^4He in this sample is held in domains that are one to three orders of magnitude smaller than the bulk crystal. We hypothesize that this arises from an inverse spatial correlation between domain size and U concentration within the crystal.

Measurement of trace- and minor-element molar ratios in dated aliquots allows us to better understand the effects of the ultrasonic cleaning and other sample treatments, and to assess the possible effects that phases other than hematite may have on (U-Th)/He dates. In some hematite samples analyzed in this study, a large fraction of the total U and Th present is hosted in phases other than hematite, which fill interstitial spaces between hematite crystals. In samples where such phases are present, treatments such as ultrasonic cleaning may increase, rather than reduce, the amount of dispersion observed among hematite (U-Th)/He dates.

(U-Th)/He dates obtained from hematite samples taken from lower and upper-plate rocks in the Buckskin-Rawhide detachment system overlap with previous estimates of the timing of detachment fault activity. Using textural observations and He diffusion kinetic values obtained from this and other studies, we estimate a bulk closure temperature range of 140 to 240 °C for hematite samples analyzed in this study. Comparisons of these dates and closure temperatures with data from other studies that constrain the thermal history of lower-plate rocks suggest that hematite (U-Th)/He dates record the timing of rapid tectonic exhumation and cooling that followed mineral formation at depth. Hematite (U-Th)/He dates obtained in this study are interpreted to be cooling dates that closely approximate the time of hematite formation from hydrothermal fluids at depth within the detachment zone. (U-Th)/He dates from Mn oxide samples are consistent with the ages of syn-extensional host strata, and may provide evidence for ongoing hydrothermal circulation through parts of the upper-plate at the time when extension along the detachment fault ended.

Overall, we find that hematite and Mn oxide (U-Th)/He dates are reproducible and yield sample ages that are consistent with the timing of rapid exhumation along the host Buckskin-Rawhide detachment fault. Our results suggest that, with additional study of He diffusion in hematite and Mn oxide, and of the distribution of parent nuclides in hematite samples, these methods will be widely applicable to dating of these common minerals.

ACKNOWLEDGMENTS

We acknowledge support from NSF grant EAR-1219653 to Reiners, and GSA Graduate Research and University of Arizona College of Science Galileo Scholarship grants to Evenson. We are grateful for analytical support from Uttam Chowdhury, Erin Abel, Clayton Loehn (Arizona Laserchron Center), and Kenneth Domanik (Drake Electron Microprobe Lab). We also appreciate helpful discussions with Alexis Ault, and constructive comments from Paul Kapp and Jay Quade. We acknowledge reviews from Peter Copeland, Peter Zeitler, and an anonymous reviewer, which significantly improved this manuscript.

Fig. 14 (continued). (Nielson and Beratan, 1995). Lower plate rocks (now exposed in the western Buckskin Mountains) were rapidly exhumed to the surface. At ~16 Ma, the lower-plate rocks in this part of the system were uplifted through the depth of hematite mineralization, and hematite (U-Th)/He dates were set in these samples. The surface exposure of these lower-plate rocks provided a source for mylonitic debris in the Chapin Wash Formation. By ~16-15 Ma, Mn oxide vein mineralization in Chapin Wash strata had begun. (D) The locus of isostatic uplift migrated NE as extension progressed. The uplift of lower-plate rocks now exposed in the Rawhide Mountains was recorded by hematite mineralization in upper and lower-plate rocks at 14.5-12.8 Ma. The surface exposure and development of relief in these rocks provided a sediment source that fed coarse mylonitic debris into the Sandtrap Conglomerate between ~12 and ~9 Ma. After extension along the detachment ceased at ~10-8 Ma, Mn mineralization in the upper-plate continued until at least 7 Ma.

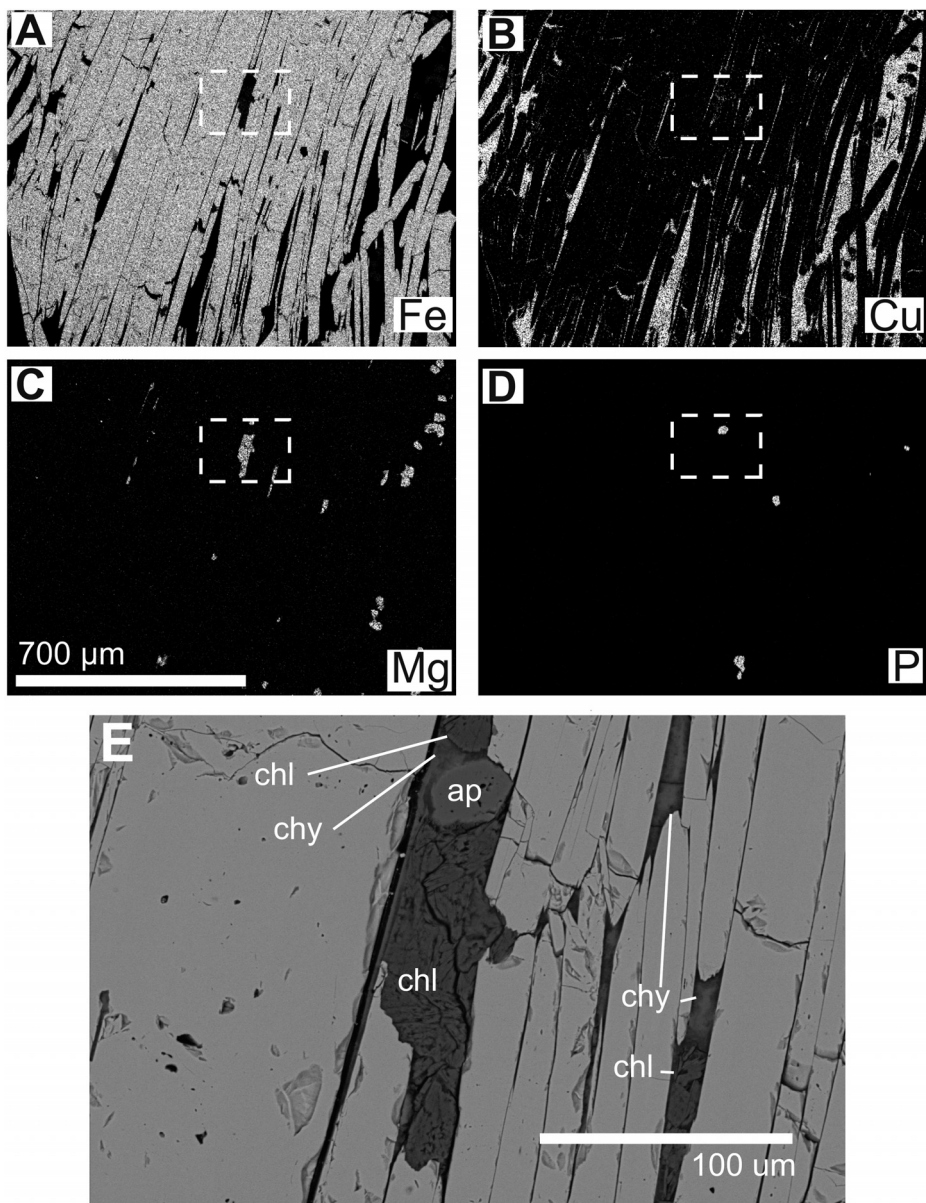


Fig. A1. SEM images and element maps of hematite sample FW3-23-85-8. Area shown in (A)–(D) is the same as that shown in figure 2A. Scale in (C) applies to panels (A)–(D). (A) Fe EDS map showing hematite crystals. (B) Cu EDS showing space-filling chrysocolla. (C) Mg EDS map showing Mg-rich chlorite. (D) P EDS map showing locations of small apatite crystals. (E) BSE image showing region of sample shown in (A)–(D) in greater detail (delineated in (A)–(D) by white dashed line). Chrysocolla (chy) fills space around clumps of chlorite (chl) crystals and an anhedronal apatite (ap) crystal. We interpret the relationships in these images to indicate that hematite and apatite were the first phases to crystallize in this sample, followed by chlorite and finally chrysocolla.

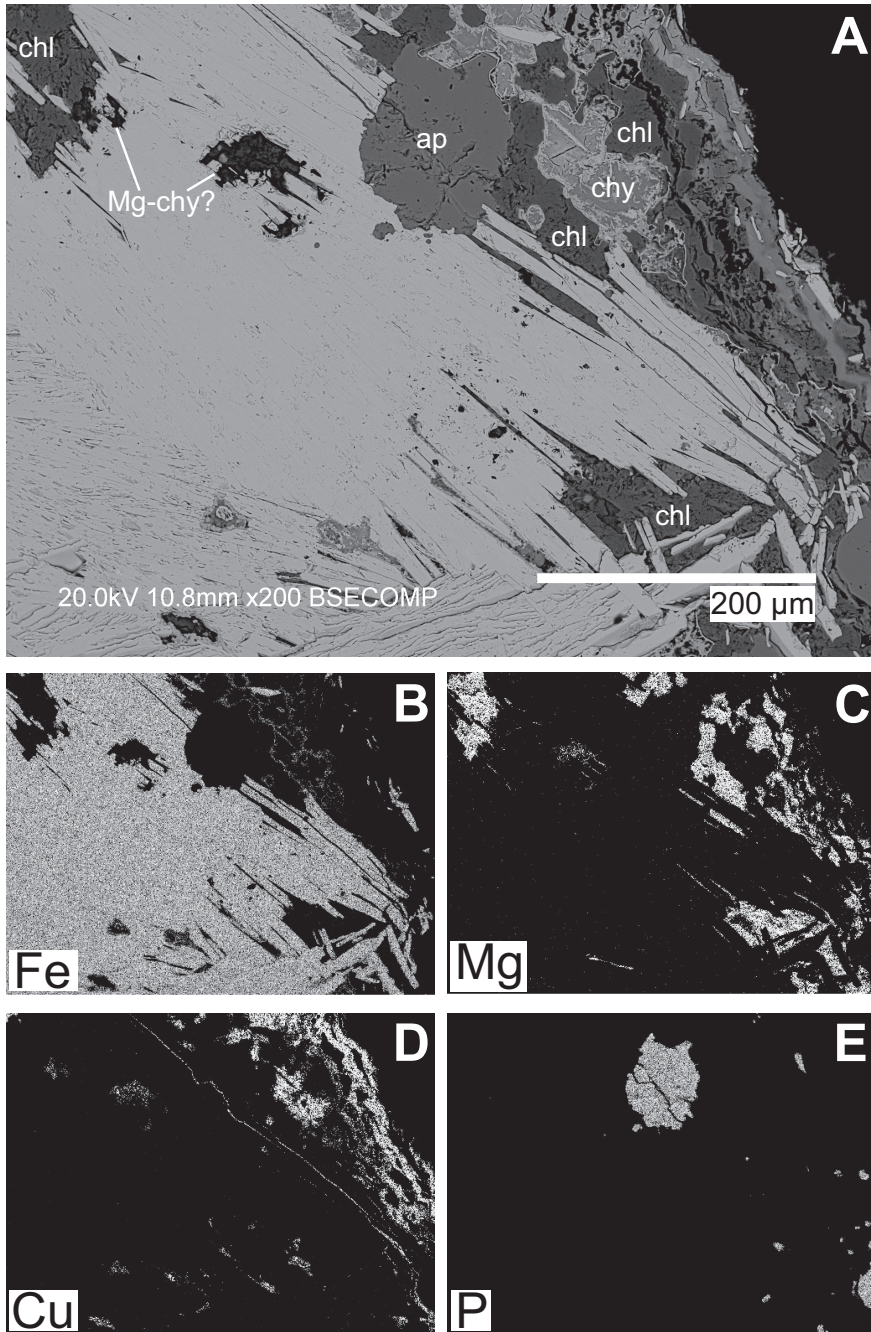


Fig. A2. BSE images and EDS maps of hematite sample FW3-21-85-12. (A) BSE image of FW3-21-85-12, showing relationships between hematite crystals, apatite (ap), Mg-rich chlorite (chl), Cu-rich chrysocolla (chy), and what may be Mg-bearing chrysocolla or amphibole (Mg-chy?). (B)–(E) are EDS element maps of the area shown in this BSE image. A large apatite crystal and smaller accumulations of other phases are observed among hematite crystals, but most other non-hematite phases are located in an external seam.

TABLE A1
Hematite electron microprobe analyses

Spot	Fe		Si		Al		Mn		Mg		Ca		Ti	
	wt%	1 σ	ppm	DL	ppm	DL	ppm	DL	ppm	DL	ppm	DL	ppm	DL
FW2-12-85-8														
1	70.09	0.349	110	164	182	20	82	28	16	26	54	13	5	21
2	70.05	0.350	173	164	39	20	73	28	6	27	24	13	N/A	N/A
3	70.03	0.350	75	164	359	20	46	28	5	26	2	13	N/A	N/A
4	69.92	0.350	116	160	104	20	77	28	N/A	N/A	42	13	16	21
5	69.50	0.349	198	164	278	20	77	28	7	27	75	13	1	21
6	69.72	0.349	21	163	158	20	68	28	0	0	34	13	N/A	N/A
7	69.78	0.349	51	165	277	20	51	28	1	26	10	13	N/A	N/A
8	69.74	0.349	30	167	147	20	73	28	1	27	3	13	15	21
9	69.13	0.347	64	159	26	20	47	28	2	27	9	13	64	21
10	69.07	0.347	87	162	241	20	63	27	7	26	N/A	N/A	N/A	N/A
FW3-23-85-8														
1	69.63	0.349	124	171	2711	19	68	26	9	25	N/A	N/A	N/A	N/A
2	69.87	0.349	107	159	409	19	56	27	1	26	77	12	N/A	N/A
3	69.13	0.347	64	167	3691	20	73	28	43	26	33	13	93	21
4	70.00	0.349	N/A	N/A	1754	20	47	27	N/A	N/A	N/A	N/A	N/A	N/A
5	70.13	0.350	58	160	597	20	60	28	4	26	N/A	N/A	N/A	N/A
6	70.12	0.351	417	173	613	20	102	28	33	27	37	13	N/A	N/A
7	70.01	0.350	N/A	N/A	573	20	57	28	3	27	1	13	N/A	N/A
8	70.08	0.350	67	160	135	20	74	28	N/A	N/A	5	13	N/A	N/A
9	70.00	0.350	N/A	N/A	866	20	60	28	2	26	9	13	3	21
FW3-21-85-12														
1	69.47	0.348	682	195	3099	20	142	28	133	27	221	13	32	21
2	69.17	0.347	1016	186	3164	20	183	28	120	27	250	13	41	21
3	69.17	0.347	817	176	3247	20	124	28	224	27	236	13	28	21
4	69.50	0.348	654	186	2957	20	127	28	171	27	307	13	326	21
5	69.59	0.349	865	184	4522	20	124	28	89	26	160	13	118	21
6	70.29	0.351	196	159	471	20	99	28	16	26	282	13	48	21
7	69.50	0.348	1299	169	4863	20	122	28	107	26	190	13	174	21
8	69.64	0.349	1429	168	3200	20	176	28	408	27	553	13	453	21
9	69.47	0.348	1831	166	2996	20	153	28	286	26	440	13	185	21
10	69.12	0.347	449	166	5504	20	174	28	117	26	372	13	247	21
FW11-29-11-1														
1	69.22	0.348	488	169	2819	20	97	28	9	26	31	13	22	21
2	68.65	0.346	N/A	N/A	4038	20	135	28	10	26	10	13	73	21
3	68.76	0.346	115	175	5537	20	135	28	1	27	13	13	896	21
4	68.66	0.345	347	159	3490	20	107	28	13	26	18	13	9	21
5	69.62	0.348	N/A	N/A	328	21	97	28	N/A	N/A	N/A	N/A	40	21
6	68.93	0.346	88	169	4118	21	108	28	14	26	10	13	N/A	N/A
7	68.68	0.345	235	162	6008	20	124	28	23	26	18	13	233	21
8	69.01	0.347	N/A	N/A	2677	20	104	28	28	26	6	13	48	21
9	70.04	0.350	N/A	N/A	2265	20	101	28	3	26	9	13	44	21
10	69.67	0.349	8	170	3419	20	73	28	6	26	4	13	4	21
11	69.19	0.348	N/A	N/A	1040	20	71	28	N/A	N/A	15	13	N/A	N/A
12	69.06	0.348	380	170	4143	20	130	28	15	27	119	13	4	21
13	68.49	0.346	237	166	6692	20	100	28	9	26	3	13	10	21
HW11-30-11-3														
1	69.67	0.348	N/A	N/A	433	20	104	28	1	26	9	13	71	21
2	69.38	0.349	N/A	N/A	604	20	120	28	1	27	37	13	36	21
3	69.24	0.348	294	173	716	20	109	28	N/A	N/A	92	13	252	21
4	69.53	0.349	N/A	N/A	689	20	109	28	N/A	N/A	18	13	187	21
5	69.48	0.349	N/A	N/A	800	20	93	28	7	26	25	13	53	21
6	69.03	0.347	175	170	898	20	84	28	7	26	7	13	1014	21
7	69.60	0.348	405	167	501	20	100	28	5	27	274	13	13	21
8	69.42	0.349	125	169	1088	20	80	28	2	26	10	13	15	21
9	69.50	0.349	155	161	1553	20	82	28	2	26	N/A	N/A	N/A	N/A
10	68.96	0.347	18	166	416	20	86	28	N/A	N/A	16	13	1623	22
HW1-16-12-1														
1	69.85	0.349	153	159	1624	18	68	26	26	24	22	12	203	20
2	69.85	0.349	165	159	1616	20	61	28	N/A	N/A	84	13	8	21
3	70.14	0.350	36	165	270	20	104	28	N/A	N/A	7	13	48	21
4	70.01	0.350	151	162	804	20	88	28	9	27	34	13	805	22
5	69.83	0.350	114	162	365	20	80	28	9	26	891	13	3993	22
6	70.12	0.350	152	162	950	20	105	28	N/A	N/A	416	13	109	21
7	69.94	0.350	51	161	224	20	85	28	N/A	N/A	11	13	1356	21
8	70.25	0.350	7	164	178	20	83	28	6	27	N/A	N/A	629	21
9	69.77	0.349	14	163	1189	20	88	28	7	26	2	13	33	22
10	69.76	0.349	N/A	N/A	1201	20	88	28	9	27	1	13	45	21
11	69.49	0.348	54	163	341	19	94	27	N/A	N/A	627	13	969	21
12	69.68	0.349	124	161	3044	20	78	28	4	26	56	13	93	21

“N/A” indicates that the measured peak intensity was too low to estimate either an element abundance or a detection limit for this analysis. For the purposes of calculating “fraction <DL” for table 2, we consider such results equivalent to those in which the reported element abundance is less than the given detection limit.

TABLE A2-Part 1
Compositions of dated and undegassed hematite aliquots

Aliquot*	(U-Th)/He Date	Fe (umol)	Mn (umol)	[Mn]	U (umol)	[U]	Th (umol)	[Th]	[eU]	Mg (umol)	[Mg]
FW2-12-85-8											
NC1	15.57	1.978	4.65E-05	23.51	8.96E-07	0.453	2.60E-08	0.013	0.456	6.57E-03	3322.7
NC2	15.83	1.722	2.03E-05	11.77	3.08E-07	0.179	2.45E-08	0.014	0.182	1.01E-03	585.0
NC3	15.48	0.789	1.94E-05	24.61	4.72E-07	0.599	2.82E-08	0.036	0.607	2.23E-03	2819.9
NC4	23.56	2.056	1.42E-04	69.10	2.89E-07	0.141	5.70E-08	0.028	0.147	7.62E-04	370.5
NC5	16.69	0.892	1.24E-04	138.88	4.59E-07	0.514	1.16E-08	0.013	0.517	9.42E-04	1056.4
NC6	14.23	1.558	7.35E-05	47.20	6.47E-07	0.415	6.13E-08	0.039	0.425	3.33E-03	2135.0
NC7	19.54	1.323	6.29E-05	47.52	1.05E-06	0.795	1.21E-07	0.092	0.816	2.04E-03	1540.0
C1	16.63	1.093	3.24E-05	29.68	3.97E-07	0.363	2.24E-08	0.021	0.368	6.01E-03	5500.6
C2	19.82	1.435	4.31E-05	30.02	7.96E-07	0.555	2.13E-08	0.015	0.558	8.06E-04	561.7
C3	15.70	0.616	1.45E-05	23.60	1.40E-07	0.227	2.83E-08	0.046	0.238	2.43E-03	3949.5
C4	16.53	1.505	3.46E-05	23.02	1.06E-06	0.708	3.36E-08	0.022	0.713	5.33E-03	3540.7
C5	49.19	0.714	1.23E-05	17.27	5.13E-08	0.072	2.59E-08	0.036	0.080	2.61E-04	366.1
UD1	---	0.784	6.59E-05	84.05	6.55E-07	0.835	2.82E-08	0.036	0.843	2.49E-04	317.4
UD2	---	0.527	5.95E-05	113.02	3.72E-07	0.705	2.34E-08	0.044	0.716	5.52E-04	1047.1
UD3	---	0.425	5.33E-05	125.37	1.50E-07	0.354	1.67E-08	0.039	0.363	9.64E-05	227.0
FW3-23-85-8											
NC1	14.68	0.787	7.91E-05	100.52	1.85E-06	2.355	2.22E-08	0.028	2.362	4.77E-04	605.4
NC2	9.98	0.601	9.06E-05	150.78	1.31E-06	2.188	1.01E-08	0.017	2.192	3.49E-03	5806.3
NC3	15.51	0.719	5.90E-05	82.08	7.92E-06	11.012	1.06E-07	0.147	11.047	2.76E-03	3843.7
NC4	33.77	1.356	3.52E-05	25.97	1.38E-06	1.018	3.41E-08	0.025	1.024	0.00E+00	0.0
NC5	16.16	0.900	7.22E-05	80.24	3.14E-06	3.484	4.92E-08	0.055	3.497	8.94E-04	993.9
NC6	6.60	0.570	4.86E-04	852.57	1.31E-05	22.985	2.07E-08	0.036	22.993	1.99E-03	3482.7
NC7	7.50	0.972	1.11E-03	1136.13	3.41E-05	35.011	5.68E-08	0.058	35.025	2.53E-03	2605.5
NC8	14.39	0.580	1.41E-04	243.71	4.37E-06	7.536	1.82E-08	0.031	7.543	1.13E-03	1944.2
C1	17.97	1.978	1.09E-04	55.09	4.85E-06	2.454	2.22E-07	0.112	2.480	1.52E-03	770.8
C2	16.59	0.961	5.80E-05	60.32	1.99E-06	2.068	3.10E-08	0.032	2.076	4.45E-04	462.8
C3	22.07	0.856	2.17E-05	25.39	2.57E-07	0.301	1.39E-08	0.016	0.304	4.92E-04	575.4
C4	45.76	0.646	1.12E-05	17.26	2.16E-07	0.334	1.27E-08	0.020	0.339	3.98E-06	6.2
C5	17.51	1.827	6.60E-04	361.39	5.99E-06	3.276	2.33E-08	0.013	3.279	1.48E-03	807.4
C6	18.31	1.368	2.96E-04	216.34	3.74E-06	2.733	2.69E-08	0.020	2.738	1.31E-03	955.9
UD1	---	1.015	7.07E-05	69.67	3.85E-07	0.379	4.10E-08	0.040	0.389	1.77E-04	174.5
UD2	---	0.297	7.72E-05	260.13	7.05E-07	2.375	2.92E-08	0.098	2.398	1.37E-04	462.4
UD3	---	0.410	1.04E-04	253.75	6.01E-07	1.466	1.80E-08	0.044	1.476	3.20E-04	780.7
FW3-21-85-12											
NC1	14.98	1.196	2.26E-04	188.68	2.11E-06	1.766	1.33E-07	0.111	1.792	3.68E-03	3072.8
NC2	14.87	1.516	2.44E-04	161.25	2.23E-06	1.473	1.29E-07	0.085	1.493	3.86E-03	2544.8
NC3	15.11	0.793	6.65E-05	83.81	1.37E-06	1.729	1.58E-07	0.199	1.776	3.19E-03	4023.9
NC4	14.97	1.003	1.91E-04	190.81	1.11E-06	1.103	2.23E-07	0.222	1.155	5.07E-03	5055.8
NC5	14.29	1.459	3.33E-04	228.04	3.03E-06	2.078	2.50E-07	0.172	2.118	5.12E-03	3511.4
NC6	14.02	0.714	1.86E-04	260.87	1.90E-06	2.665	2.65E-07	0.370	2.752	4.29E-03	6003.1
NC7	15.09	1.234	3.83E-04	310.09	3.73E-06	3.024	3.62E-07	0.293	3.093	7.60E-03	6159.1
NC8	13.44	0.263	8.36E-05	317.77	1.06E-06	4.014	8.07E-08	0.307	4.086	2.13E-03	8089.1
C1	16.10	0.521	2.46E-05	47.27	1.03E-06	1.969	5.65E-08	0.108	1.995	1.24E-03	2372.6
C2	16.18	0.336	9.99E-06	29.77	6.08E-07	1.811	3.89E-08	0.116	1.838	3.30E-04	984.7
C3	17.80	0.755	1.64E-05	21.79	1.22E-06	1.612	3.12E-07	0.414	1.710	1.92E-03	2542.5
C4	17.40	1.288	3.22E-04	249.72	1.49E-06	1.155	4.38E-07	0.340	1.235	9.65E-03	7495.7
L-NC1	15.54	0.639	1.89E-04	295.95	6.89E-07	1.079	1.01E-07	0.159	1.116	4.40E-03	6896.7
L-NC2	14.56	0.920	2.26E-04	245.60	1.34E-06	1.461	1.43E-07	0.155	1.498	3.01E-03	3272.3
L-NC3	7.86	0.843	9.57E-05	113.49	1.27E-06	1.503	9.82E-08	0.117	1.531	1.82E-03	2156.3
L-NC4	14.58	1.216	2.03E-04	167.06	1.72E-06	1.417	1.33E-07	0.110	1.442	5.76E-03	4740.4
UD1	---	1.470	3.11E-04	211.70	1.78E-06	1.212	1.90E-07	0.129	1.242	2.43E-03	1651.7
UD2	---	1.230	2.85E-04	231.26	1.85E-06	1.501	1.13E-07	0.092	1.523	3.47E-03	2823.0
UD3	---	0.743	2.69E-04	361.85	1.03E-06	1.388	7.66E-08	0.103	1.412	8.06E-03	10844.4
FW11-29-11-1											
NC1	5.84	1.154	1.40E-04	121.06	3.63E-06	3.149	4.33E-07	0.375	3.237	2.68E-03	2322.9
NC2	12.84	0.603	4.74E-05	78.55	1.62E-07	0.269	4.86E-08	0.081	0.288	1.12E-04	185.9
NC3	12.62	1.351	1.23E-04	90.81	4.75E-07	0.351	1.32E-07	0.098	0.374	1.43E-03	1055.4
NC4	13.21	1.865	2.01E-04	107.54	1.14E-06	0.614	3.12E-08	0.017	0.618	1.64E-03	879.2
NC5	12.39	1.407	1.37E-04	97.20	5.89E-07	0.419	1.67E-07	0.119	0.446	1.12E-03	798.6
NC6	13.12	1.064	9.43E-05	88.63	5.90E-07	0.555	4.05E-08	0.038	0.564	3.11E-04	292.5
C1	13.38	0.559	3.35E-05	59.85	2.86E-07	0.511	1.66E-08	0.030	0.518	1.75E-04	313.3
C2	12.34	1.148	1.30E-04	113.02	5.60E-07	0.488	1.23E-07	0.107	0.513	4.03E-04	351.4
C3	12.96	1.707	1.90E-04	111.07	9.32E-07	0.546	9.57E-08	0.056	0.559	8.35E-04	489.0
C4	12.51	1.523	1.20E-04	79.02	6.08E-07	0.399	4.92E-08	0.032	0.407	<DL	1.0
C5	15.84	0.893	3.76E-05	42.08	2.80E-07	0.314	4.86E-08	0.054	0.327	<DL	1.0
C6	13.38	1.190	1.26E-04	105.57	4.65E-07	0.391	5.29E-08	0.044	0.401	2.08E-04	175.1

TABLE A2—Part 1
(continued)

Aliquot*	(U-Th)/He Date	Fe (umol)	Mn (umol)	[Mn]	U (umol)	[U]	Th (umol)	[Th]	[eU]	Mg (umol)	[Mg]
HW1-16-12-1											
NC1	15.57	1.978	4.65E-05	23.51	8.96E-07	0.453	2.60E-08	0.013	0.456	6.57E-03	3322.7
NC1	12.71	1.040	2.96E-04	284.18	1.07E-06	1.027	1.79E-07	0.172	1.068	2.47E-03	2374.0
NC2	10.89	0.087	2.13E-05	244.99	3.07E-08	0.353	2.96E-08	0.341	0.434	1.75E-03	20183.1
NC3	12.02	0.070	1.37E-05	194.52	3.59E-08	0.511	2.61E-08	0.372	0.599	3.62E-04	5155.0
NC4	10.80	0.065	1.29E-05	200.53	3.02E-08	0.469	1.64E-08	0.254	0.528	2.82E-04	4364.0
NC5	12.98	0.080	4.91E-06	61.19	3.82E-08	0.475	1.98E-08	0.247	0.533	2.25E-04	2796.7
C1	15.47	0.803	2.37E-04	294.54	3.67E-07	0.456	1.69E-07	0.211	0.506	1.75E-03	2176.2
C2	13.68	1.027	2.22E-04	216.01	3.83E-07	0.373	3.32E-07	0.323	0.448	9.87E-04	961.2
C3	14.91	1.162	1.27E-04	109.65	1.01E-06	0.866	1.83E-07	0.157	0.903	3.76E-03	3235.8
C4	14.96	2.413	7.44E-04	308.10	8.89E-07	0.368	3.40E-07	0.141	0.401	1.42E-02	5884.7
C5	14.49	0.645	1.58E-04	244.76	2.55E-07	0.395	1.11E-07	0.172	0.435	1.12E-03	1740.3
C6	15.47	0.358	3.93E-05	109.78	1.39E-07	0.388	6.34E-08	0.177	0.430	<DL	<DL
C7	16.52	0.349	2.88E-05	82.34	2.21E-07	0.634	7.44E-08	0.213	0.684	<DL	<DL
NC-UD1	---	0.983	1.04E-03	1051.67	6.04E-07	0.614	3.10E-07	0.315	0.688	4.01E-02	40800.6
NC-UD2	---	0.166	6.94E-05	417.03	7.32E-08	0.440	5.63E-08	0.339	0.520	3.55E-04	2137.8
NC-UD3	---	0.298	1.80E-04	604.89	1.04E-07	0.348	7.27E-08	0.244	0.405	7.07E-03	23720.9
C-UD1	---	1.128	3.40E-04	301.19	8.22E-07	0.729	2.04E-07	0.181	0.771	3.76E-03	3335.3
C-UD2	---	0.542	3.20E-04	590.66	1.17E-07	0.216	5.06E-08	0.093	0.238	8.50E-04	1567.2
HW11-30-11-3											
NC1	12.71	1.040	2.96E-04	284.18	1.07E-06	1.027	1.79E-07	0.172	1.068	2.47E-03	2374.0
NC2	10.89	0.087	2.13E-05	244.99	3.07E-08	0.353	2.96E-08	0.341	0.434	1.75E-03	20183.1
NC3	12.02	0.070	1.37E-05	194.52	3.59E-08	0.511	2.61E-08	0.372	0.599	3.62E-04	5155.0
NC4	10.80	0.065	1.29E-05	200.53	3.02E-08	0.469	1.64E-08	0.254	0.528	2.82E-04	4364.0
NC5	12.98	0.080	4.91E-06	61.19	3.82E-08	0.475	1.98E-08	0.247	0.533	2.25E-04	2796.7
C1	12.62	0.982	3.50E-04	356.18	1.32E-06	1.347	4.64E-07	0.473	1.458	4.55E-03	4634.5
C2	11.35	1.117	3.82E-04	341.89	7.05E-07	0.631	2.59E-07	0.231	0.685	5.04E-03	4514.3
C3	10.88	0.438	1.21E-04	276.15	7.46E-07	1.703	4.91E-07	1.121	1.967	1.88E-03	4297.5
C4	8.92	0.271	5.81E-05	214.38	2.33E-07	0.859	6.42E-08	0.237	0.915	1.11E-03	4092.5
C5	14.80	0.329	2.23E-05	67.80	2.93E-07	0.892	2.46E-07	0.746	1.068	4.55E-04	1383.4
C6	18.36	0.244	3.46E-05	141.79	2.63E-07	1.079	1.24E-07	0.508	1.198	1.49E-04	608.4
C7	16.00	0.846	1.56E-04	184.48	5.63E-07	0.665	2.69E-07	0.318	0.740	1.33E-03	1574.1
Priceless (Mn oxide)											
NC1	15.57	0.053	0.880	9.43E+05	1.02E-06	1.163	1.11E-08	0.013	1.166	8.93E-04	1014.4
NC2	13.91	0.036	0.466	9.28E+05	1.23E-06	2.640	8.77E-09	0.019	2.644	3.89E-04	834.2
NC3	11.74	0.031	0.495	9.40E+05	1.28E-06	2.594	1.24E-08	0.025	2.600	5.31E-04	1073.6
NC4	13.96	0.045	0.559	9.26E+05	7.02E-07	1.255	1.39E-08	0.025	1.261	7.18E-04	1284.3
UD1	---	0.054	0.478	8.98E+05	4.07E-07	0.851	2.57E-08	0.054	0.863	4.52E-04	943.8
UD2	---	0.068	0.629	9.02E+05	5.08E-07	0.807	1.94E-08	0.031	0.814	5.66E-04	898.9
UD3	---	0.047	0.382	8.91E+05	3.50E-07	0.917	2.44E-08	0.064	0.932	4.54E-04	1188.6
Shannon (Mn oxide)											
NC1	8.48	0.049	0.514	9.13E+05	2.12E-06	4.125	2.80E-08	0.055	4.138	3.34E-04	649.4
NC2	7.82	0.053	0.672	9.27E+05	3.09E-06	4.602	1.17E-08	0.017	4.606	6.00E-04	893.7
NC3	7.62	0.053	0.540	9.10E+05	2.56E-06	4.745	2.99E-08	0.055	4.758	4.60E-04	851.5

TABLE A2-Part 2

Composition of dated and undegassed hematite aliquots

Aliquot*	Ca (umol)	[Ca]	Cu (umol)	[Cu]	Pb (umol)	[Pb]	Ba (umol)	[Ba]
FW2-12-85-8								
NC1	3.70E-04	187.1	1.91E-04	96.8	2.32E-07	0.12	7.23E-06	3.65
NC2	6.25E-04	362.8	5.09E-05	29.6	1.24E-06	0.72	4.38E-06	2.54
NC3	4.52E-04	572.5	6.37E-05	80.7	7.65E-07	0.97	4.97E-06	6.29
NC4	2.95E-04	143.7	9.85E-05	47.9	2.85E-07	0.14	2.82E-06	1.37
NC5	1.26E-04	140.8	3.20E-05	35.9	5.06E-07	0.57	1.64E-06	1.84
NC6	1.06E-03	678.5	---	---	<DL	<DL	6.05E-06	3.89
NC7	6.67E-04	504.3	---	---	<DL	<DL	2.55E-06	1.92
C1	2.00E-03	1827.6	3.75E-05	34.3	3.13E-07	0.29	3.66E-06	3.35
C2	1.42E-04	98.9	6.49E-05	45.2	9.61E-07	0.67	2.62E-06	1.83
C3	3.90E-04	633.2	4.40E-05	71.3	7.87E-07	1.28	2.15E-06	3.48
C4	7.15E-04	475.4	8.12E-05	54.0	1.38E-06	0.91	1.41E-06	0.94
C5	7.84E-04	1097.8	7.51E-05	105.2	5.06E-07	0.71	8.69E-06	12.17
UD1	3.96E-04	504.4	1.79E-03	2284.8	3.06E-06	3.90	5.59E-06	7.13
UD2	9.43E-04	1789.9	1.77E-03	3361.6	3.07E-06	5.82	3.59E-06	6.81
UD3	1.16E-04	272.8	1.51E-03	3557.0	2.91E-06	6.85	4.06E-06	9.56
FW3-23-85-8								
NC1	1.52E-04	192.5	7.62E-04	968.1	2.61E-06	3.32	2.84E-06	3.61
NC2	4.24E-04	705.7	1.36E-04	226.1	1.48E-06	2.47	2.38E-06	3.96
NC3	7.88E-04	1095.7	1.65E-04	229.7	1.53E-06	2.13	4.68E-06	6.51
NC4	2.23E-04	164.4	1.60E-03	1179.7	3.48E-07	0.26	1.88E-06	1.39
NC5	3.15E-04	349.6	5.85E-04	649.7	3.16E-08	0.04	2.35E-06	2.61
NC6	8.52E-04	1493.4	---	---	1.30E-06	2.28	4.60E-06	8.07
NC7	1.17E-03	1207.5	---	---	<DL	<DL	9.80E-06	10.08
NC8	4.71E-04	812.0	---	---	<DL	<DL	2.73E-06	4.71
C1	1.55E-03	785.7	1.21E-03	610.9	7.44E-07	0.38	3.46E-06	1.75
C2	1.24E-04	129.3	9.60E-04	998.1	3.69E-07	0.38	2.28E-06	2.37
C3	7.70E-04	900.1	3.91E-05	45.7	3.16E-07	0.37	1.41E-06	1.65
C4	1.93E-04	298.9	5.33E-05	82.5	3.16E-07	0.49	2.11E-06	3.27
C5	4.93E-04	269.9	3.08E-03	1684.3	4.63E-07	0.25	7.62E-06	4.17
C6	2.01E-04	146.9	6.47E-04	472.9	2.31E-07	0.17	4.41E-06	3.22
UD1	4.51E-04	444.4	1.97E-03	1936.7	4.75E-06	4.68	4.64E-06	4.58
UD2	1.71E-04	575.2	2.68E-03	9031.3	3.98E-06	13.40	3.58E-06	12.05
UD3	2.27E-04	552.5	2.78E-03	6790.4	4.34E-06	10.59	6.04E-06	14.73
FW3-21-85-12								
NC1	5.56E-03	4650.0	4.93E-04	412.0	2.48E-07	0.21	4.18E-06	3.49
NC2	1.23E-03	811.6	1.97E-03	1301.4	5.36E-07	0.35	4.27E-06	2.82
NC3	1.77E-03	2230.7	1.40E-04	176.3	5.71E-07	0.72	3.55E-06	4.47
NC4	3.07E-03	3056.4	2.98E-04	297.6	4.90E-07	0.49	1.64E-06	1.64
NC5	4.34E-03	2974.2	3.09E-04	211.8	9.64E-07	0.66	1.03E-05	7.08
NC6	1.03E-03	1439.4	---	---	1.22E-06	1.71	2.87E-06	4.02
NC7	3.46E-03	2805.8	---	---	1.40E-06	1.13	5.25E-06	4.25
NC8	1.92E-03	7313.0	---	---	1.38E-07	0.52	2.18E-06	8.29
C1	1.08E-03	2073.3	3.24E-04	622.1	1.01E-06	1.93	2.96E-06	5.68
C2	4.95E-04	1474.3	1.44E-04	428.9	4.62E-07	1.38	2.06E-06	6.13
C3	1.90E-03	2516.5	4.71E-04	624.5	7.03E-07	0.93	4.25E-06	5.63
C4	4.27E-03	3316.2	8.19E-04	636.0	4.58E-07	0.36	4.70E-06	3.65
L-NC1	9.98E-04	1562.6	5.68E-05	89.0	2.06E-07	0.32	2.11E-06	3.31
L-NC2	6.56E-04	712.8	3.81E-05	41.4	6.32E-07	0.69	1.17E-06	1.28
L-NC3	1.16E-03	1374.5	4.06E-05	48.2	1.09E-06	1.29	2.58E-06	3.06
L-NC4	7.81E-04	642.1	5.18E-05	42.6	5.06E-07	0.42	1.88E-06	1.55
UD1	3.05E-03	2076.9	2.00E-03	1360.1	7.99E-06	5.43	1.12E-05	7.63
UD2	2.54E-03	2064.5	2.13E-03	1733.6	3.98E-06	3.24	2.05E-05	16.63
UD3	1.12E-03	1512.5	2.52E-03	3395.9	3.15E-06	4.23	5.75E-06	7.74
FW11-29-11-1								
NC1	7.42E-03	6434.0	1.61E-04	139.9	3.68E-07	0.32	4.01E-06	3.47
NC2	2.97E-04	493.1	3.65E-05	60.5	5.29E-07	0.88	5.33E-06	8.84
NC3	2.70E-03	1999.2	3.94E-04	291.4	2.79E-07	0.21	3.28E-06	2.43
NC4	3.33E-04	178.7	8.94E-05	47.9	7.88E-07	0.42	8.12E-06	4.35
NC5	1.65E-03	1169.5	7.77E-04	552.0	6.43E-07	0.46	4.58E-05	32.53
NC6	2.24E-04	210.3	9.44E-05	88.7	4.38E-07	0.41	8.52E-06	8.01
C1	4.05E-04	724.0	<DL	<DL	4.58E-07	0.82	2.58E-06	4.62
C2	4.40E-04	383.5	9.08E-05	79.1	1.66E-06	1.45	7.98E-06	6.96
C4	1.03E-04	67.6	3.65E-05	24.0	6.48E-07	0.43	5.17E-06	3.39
C5	9.17E-05	102.8	4.52E-05	50.6	2.06E-07	0.23	3.05E-06	3.42
C6	8.69E-04	730.4	1.12E-04	93.8	1.28E-06	1.08	4.23E-06	3.55

TABLE A2—Part 2
(continued)

Aliquot*	Ca (umol)	[Ca]	Cu (umol)	[Cu]	Pb (umol)	[Pb]	Ba (umol)	[Ba]
HW1-16-12-1								
NC1	1.21E-03	1536.9	8.62E-05	109.2	2.45E-07	0.31	8.15E-06	10.32
NC2	6.04E-04	1091.5	5.96E-05	107.8	8.27E-08	0.15	3.81E-06	6.88
NC3	1.81E-03	5545.5	4.79E-05	146.8	1.32E-07	0.40	4.36E-06	13.35
NC4	2.43E-02	19520.8	3.36E-04	269.1	6.16E-08	0.05	8.72E-05	69.91
NC5	1.25E-02	10092.5	1.30E-04	105.5	9.96E-08	0.08	1.22E-05	9.89
NC6	2.96E-03	1542.6	1.40E-04	72.8	9.08E-07	0.47	1.52E-05	7.90
NC7	1.50E-03	898.2	1.44E-04	86.7	4.77E-07	0.29	2.31E-05	13.90
C1	6.68E-03	8314.2	6.60E-05	82.2	6.96E-07	0.87	5.17E-06	6.43
C2	1.90E-03	1846.6	8.48E-05	82.5	1.12E-06	1.09	4.93E-06	4.80
C3	7.64E-04	657.3	1.98E-04	170.4	2.12E-06	1.82	1.27E-05	10.92
C4	2.41E-02	10005.1	2.71E-04	112.3	1.30E-06	0.54	1.22E-05	5.06
C5	4.14E-03	6425.7	4.82E-05	74.7	2.36E-06	3.65	1.03E-05	16.02
C6	1.11E-03	3111.0	9.14E-05	255.0	1.57E-06	4.37	3.99E-06	11.14
C7	1.70E-04	486.1	9.64E-06	27.6	2.81E-06	8.06	1.00E+00	12.14
NC-UD1	1.31E-03	1327.9	1.51E-03	1531.4	5.87E-06	5.97	5.23E-05	53.20
NC-UD2	3.86E-04	2321.5	2.26E-03	13602.4	2.65E-06	15.95	5.10E-06	30.64
HW1-16-12-1								
NC-UD3	2.08E-04	698.4	2.22E-03	7447.0	3.53E-06	11.84	6.45E-06	21.64
C-UD1	1.70E-03	1510.3	1.57E-03	1387.0	6.48E-06	5.75	1.55E-05	13.70
C-UD2	4.74E-03	8735.9	2.13E-03	3927.4	3.62E-06	6.67	9.05E-06	16.69
HW11-30-11-3								
NC1	7.34E-04	705.5	3.70E-05	35.5	1.56E-07	0.15	9.72E-06	9.34
NC2	7.55E-04	8696.1	1.09E-04	1257.8	4.41E-06	50.79	1.26E-05	145.39
NC3	6.03E-04	8581.1	2.16E-05	308.0	4.48E-06	63.81	9.88E-07	14.06
NC4	1.75E-03	27134.1	1.12E-04	1737.4	1.27E-06	19.71	6.48E-06	100.43
NC5	4.22E-04	5261.1	3.75E-05	466.8	3.94E-07	4.91	1.13E-06	14.14
C1	7.42E-04	755.5	1.11E-04	112.7	5.85E-07	0.60	4.70E-06	4.78
C2	6.52E-04	583.3	5.28E-05	47.2	1.66E-06	1.49	9.16E-06	8.20
C3	3.42E-04	781.1	9.90E-05	226.0	6.17E-07	1.41	2.07E-05	47.20
C4	1.70E-04	626.4	4.57E-05	168.5	3.48E-07	1.28	3.05E-06	11.26
C5	1.64E-03	4980.1	4.52E-05	137.3	1.98E-06	6.01	9.39E-07	2.86
C6	1.76E-04	721.5	6.64E-04	2717.8	2.69E-07	1.10	9.39E-07	3.85
C7	3.84E-04	453.5	<DL	<DL	4.11E-07	0.49	3.52E-06	4.16
Priceless (Mn oxide)								
NC1	1.30E-02	14826.7	3.71E-04	421.9	1.08E-04	122.2	9.04E-02	1.03E+05
NC2	4.88E-03	10470.8	1.38E-04	295.5	5.22E-04	1121.9	4.67E-02	1.00E+05
NC3	5.73E-03	11578.4	6.33E-05	127.9	4.17E-05	84.3	4.19E-02	8.46E+04
NC4	8.33E-03	14905.1	2.23E-04	399.6	3.79E-04	677.2	5.60E-02	1.00E+05
UD1	5.62E-03	11745.9	1.59E-03	3318.4	9.16E-03	19145.1	4.00E-02	8.36E+04
UD2	7.87E-03	12498.5	2.50E-03	3971.9	1.04E-02	16509.4	5.79E-02	9.20E+04
UD3	5.18E-03	13565.6	1.90E-03	4972.8	3.07E-03	8028.3	3.62E-02	9.47E+04
Shannon (Mn oxide)								
NC1	4.62E-03	8999.6	3.48E-04	677.5	8.59E-07	1.67	5.61E-02	1.09E+05
NC2	6.94E-03	10330.3	1.10E-03	1640.6	1.46E-06	2.18	7.05E-02	1.05E+05
NC3	5.55E-03	10267.9	3.67E-04	679.3	1.20E-07	0.22	5.75E-02	1.06E+05

The concentration of an element in $\mu\text{mol}/(\text{mol Fe} + \text{Mn})$ is noted as the element symbol inside of brackets. Example: [Ca].

* "Aliquot" provides information about aliquot treatment: C is ultrasonically cleaned, NC is not cleaned, UD is undegassed (not heated with laser), L is leached. Unless otherwise specified, UD aliquots are not cleaned.

"—" indicates that this quantity was not measured in the case of this sample. "<DL" indicates that the measured quantity was below the element detection limit.

TABLE A3
Mn oxide electron microprobe analyses

Spot	Mn	K	Pb	Ca	Ba	Cu	Zn	As	Sr	O	Total
Priceless											
1	49.14	0.14	0.10	0.22	12.82	0.01	1.07	0.22	1.15	30.78	95.65
2	48.11	0.08	0.69	0.16	13.81	0.08	0.94	0.30	0.85	30.26	95.28
3	47.72	0.11	3.11	0.19	11.91	0.13	1.04	0.32	0.86	30.06	95.44
4	46.72	0.11	5.24	0.26	9.97	0.25	1.22	0.29	0.74	29.49	94.29
5	41.74	0.02	24.09	0.15	0.73	0.27	1.77	0.39	0.03	26.95	96.14
6	46.73	0.16	7.94	0.31	7.77	0.08	1.39	0.38	0.74	29.51	95.03
7	46.61	0.11	7.84	0.17	9.48	0.10	1.33	0.33	0.50	29.50	95.97
8	48.15	0.09	1.67	0.14	13.35	0.05	1.00	0.37	0.86	30.33	96.01
9	47.95	0.08	1.85	0.13	13.19	0.03	1.02	0.30	0.67	30.15	95.36
10	47.69	0.06	0.71	0.12	14.28	0.05	0.96	0.26	0.71	30.01	94.86
11	45.88	0.06	11.78	0.10	7.88	0.02	1.31	0.25	0.28	29.06	96.62
12	49.15	0.13	0.27	0.19	12.80	0.02	1.10	0.25	1.05	30.79	95.75
13	46.29	0.09	9.61	0.14	8.98	0.00	0.96	0.15	0.30	29.17	95.69
14	50.25	0.10	0.82	0.22	12.20	0.07	1.15	0.17	0.57	31.32	96.85
15	43.96	0.02	24.50	0.02	0.69	0.01	0.07	0.07	0.06	27.64	97.04
16	47.58	0.09	4.74	0.19	12.21	0.06	0.92	0.17	0.39	29.96	96.30
17	47.61	0.09	5.18	0.10	11.96	0.03	0.70	0.15	0.36	29.88	96.07
18	49.99	0.10	0.83	0.27	11.93	0.07	1.36	0.30	0.67	31.27	96.80
19	46.03	0.13	10.05	0.16	8.68	0.11	0.85	0.39	0.32	29.11	95.83
20	46.80	0.13	9.30	0.19	9.17	0.08	0.72	0.37	0.53	29.56	96.87
21	47.25	0.14	7.77	0.19	9.56	0.07	0.67	0.36	0.68	29.76	96.44
22	47.39	0.16	5.79	0.22	10.17	0.05	0.72	0.41	0.77	29.82	95.50
23	47.90	0.19	5.49	0.24	9.94	0.08	0.78	0.37	0.85	30.10	95.93
24	47.06	0.18	6.92	0.26	9.47	0.12	0.81	0.37	0.79	29.68	95.66
25	44.32	0.07	15.00	0.16	5.40	0.14	0.84	0.30	0.13	28.05	94.43
26	42.85	0.03	23.32	0.13	1.61	0.15	1.03	0.55	0.03	27.48	97.19
27	43.57	0.06	19.08	0.14	3.63	0.08	0.81	0.38	0.05	27.69	95.48
28	42.30	0.03	23.94	0.17	1.26	0.14	1.13	0.57	0.03	27.20	96.76
29	42.99	0.06	18.35	0.15	3.71	0.12	0.71	0.27	0.05	27.26	93.67
Shannon											
1	49.05	0.08	0.00	0.17	15.13	0.08	0.16	0.23	0.53	30.65	96.09
2	49.38	0.09	0.00	0.14	15.29	0.08	0.18	0.29	0.51	30.87	96.84
3	49.47	0.09	0.00	0.17	15.11	0.08	0.20	0.27	0.53	30.91	96.82
4	49.18	0.08	0.00	0.18	15.20	0.08	0.18	0.25	0.50	30.74	96.37
5	49.04	0.08	0.04	0.22	14.83	0.08	0.23	0.35	0.63	30.70	96.20
6	49.04	0.10	0.01	0.24	14.57	0.05	0.22	0.46	0.75	30.73	96.16
7	48.91	0.09	0.04	0.22	14.64	0.05	0.25	0.35	0.70	30.61	95.85
8	49.10	0.09	0.00	0.18	15.20	0.07	0.17	0.29	0.68	30.74	96.51
9	48.86	0.09	0.00	0.20	14.96	0.06	0.15	0.30	0.64	30.57	95.83
10	48.92	0.08	0.00	0.20	15.01	0.08	0.26	0.44	0.69	30.69	96.38
11	48.98	0.08	0.02	0.12	15.41	0.03	0.13	0.16	0.46	30.56	95.94
12	48.66	0.08	0.01	0.19	14.95	0.07	0.20	0.29	0.52	30.43	95.38
13	47.61	0.14	0.53	0.46	13.76	0.45	0.45	0.36	0.31	29.98	94.05
14	48.46	0.09	0.03	0.29	14.92	0.06	0.24	0.35	0.52	30.38	95.34
15	48.69	0.08	0.00	0.20	14.88	0.07	0.23	0.37	0.58	30.49	95.60
16	47.27	0.08	0.00	0.17	14.83	0.08	0.17	0.20	0.41	29.55	92.76
17	48.32	0.08	0.00	0.20	14.92	0.06	0.22	0.29	0.55	30.25	94.88
18	49.04	0.07	0.01	0.14	15.64	0.03	0.13	0.17	0.39	30.62	96.23
19	47.38	0.07	0.01	0.13	14.67	0.06	0.14	0.15	0.49	29.56	92.65
20	49.11	0.08	0.00	0.11	15.30	0.03	0.11	0.11	0.49	30.61	95.96
21	48.96	0.07	0.00	0.16	15.32	0.04	0.16	0.22	0.55	30.60	96.08
22	49.24	0.08	0.05	0.12	15.63	0.04	0.10	0.14	0.47	30.74	96.62
23	48.61	0.09	0.05	0.21	14.85	0.04	0.21	0.31	0.62	30.43	95.42
24	48.37	0.09	0.00	0.18	14.74	0.05	0.18	0.30	0.59	30.24	94.75
25	49.01	0.08	0.00	0.20	14.97	0.06	0.16	0.20	0.61	30.62	95.90
26	46.15	0.08	0.03	0.21	14.38	0.06	0.19	0.24	0.54	28.89	90.76
27	49.28	0.07	0.00	0.15	15.35	0.04	0.18	0.25	0.53	30.80	96.65

All abundances provided in wt%.

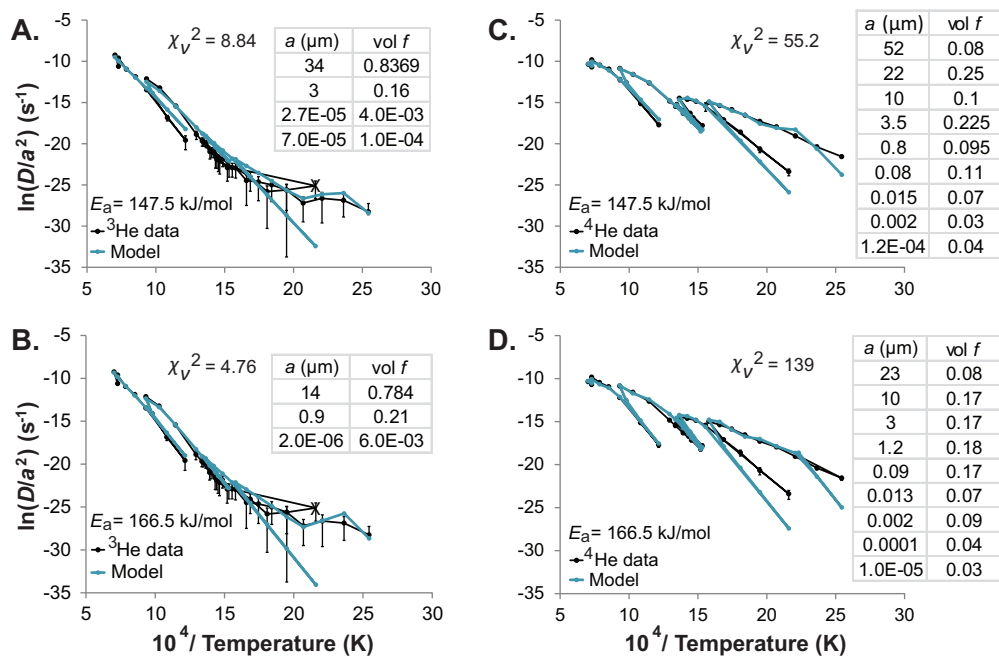


Fig. A3. Results of multiple diffusion domain (MDD) modeling of ^3He and ^4He step heating data from hematite sample FW2-12-85-8 (table 8). Models were constructed using $D_0 = 2.2 \times 10^{-4} \text{ cm}^2/\text{s}$ and the given E_a value and distribution of domain sizes. Error bars are 2σ uncertainty. Reduced chi-squared (χ_v^2) values provide a measure of model fit. (A) and (B) show MDD models of ^3He data that use different E_a values. The data point indicated by an X in each of these plots could not be reproduced by the models, and is excluded from assessments of fit. A better fit is obtained using the higher E_a value ($=166.5$ kJ/mol) in (B); this model yields lower a values than the model in (A). Both models of ^3He data indicate that a very small volume ($<1\%$) of the sample comprises a material with high He diffusivity. (C) and (D) show MDD models of ^4He data. A greater number of domains are required to obtain acceptable fits to ^4He data. In contrast to ^3He data, a better fit to ^4He data is obtained by using a lower value of E_a , however, even domains constructed using this lower E_a value cannot reproduce low-T segments of the trend where some prograde and retrograde steps overlap. This fact, along with lower $\ln(D/a^2)$ uncertainties than in ^3He data, results in relatively high χ_v^2 values. These low-T segments may correspond to the high-diffusivity material inferred from ^3He data; if so, these domains contain a much higher fraction of the total ^4He than expected. These models assume a hematite E_a and D_0 for all domains, but we speculate that phases with lower activation energies than hematite might contribute a fraction of the He produced in these low-T steps, rather than hematite with $a < 1$ nm. The distributions of ^3He and ^4He among domains of different sizes implied by models in (A)–(C) are shown in figure 8B.

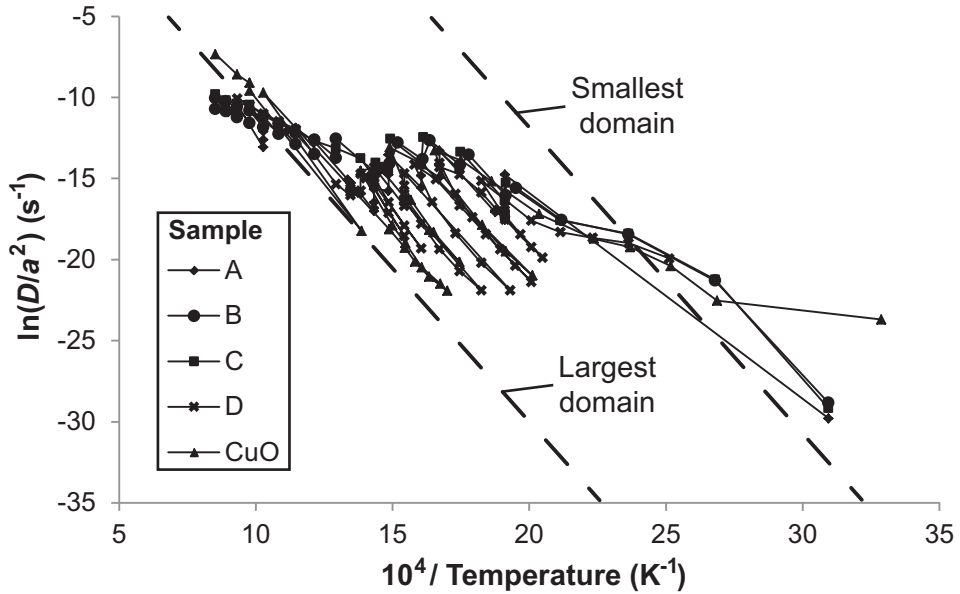


Fig. A4. Plot of hematite ^3He diffusion data from Farley and Flowers (2012). To obtain the two data points from this study shown in figure 11 and listed in table 10, we identified the steps in each set of step heating data for which the cumulative fraction of ^3He released was 1–2% and 98–99%, which we suggest drew He largely from the smallest and largest domains in the sample, respectively. We plotted a line with a slope corresponding to $E_a = 157 \text{ kJ/mol}$ [the value identified by Farley and Flowers (2012)] that fit the data point for each of these steps. The dashed lines plotted in the figure were plotted using the mean of the y-intercepts of the lines fit to the small and large domain data points in each sample. We used these mean lines to obtain a D/a^2 value at 350 °C for the smallest and largest domains.

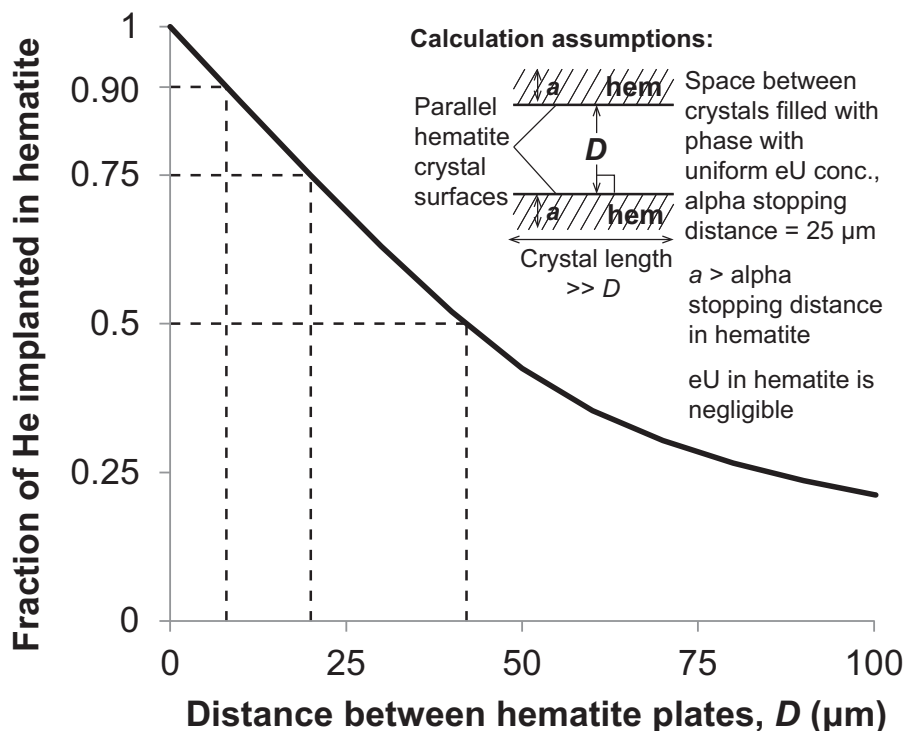


Fig. A5. Plot showing the effects of ^4He loss from interstitial phases in hematite samples. The curve shows the fraction of ^4He ejected from a body of interstitial phase that is implanted in two neighboring hematite crystals as a function of the distance between the neighboring plate-shaped hematite crystals (that is, the width of the interstitial phase, D). In calculating this curve, we assume that the hematite plates are perfectly parallel and of a lateral extent much greater than the distance between plate surfaces (that is, that ^4He atoms will not pass through the hematite crystals). We assume that the space between these plate crystals is filled with interstitial phases of uniform eU concentration, and that the alpha stopping distance within this phase is 25 μm (a reasonable distance given the lower densities of common interstitial phases encountered in analyzed samples). Under these assumptions, when the distance between plates is as small as 8–10 μm , $\sim 10\%$ of the total ^4He produced in the interstitial phase is not implanted into hematite, and will therefore be lost by diffusion (see Discussion). If the molar ratio of eU in interstitial phases is much greater than that observed in hematite crystals, then just a few large ($D = 25\text{--}40 \mu\text{m}$) bodies of interstitial phase will represent a large fraction of the total eU in a given polycrystalline aliquot, and much of the ^4He produced from the eU in these bodies will not be retained. This can lead to single-aliquot (U-Th)/He dates significantly younger than the He closure age of the sample.

REFERENCES

- Arnold, T., Zorn, T., Bernhard, G., and Nitsche, H., 1998, Sorption of uranium(VI) onto phyllite: *Chemical Geology*, v. 151, n. 1–4, p. 129–141, [http://dx.doi.org/10.1016/S0009-2541\(98\)00075-8](http://dx.doi.org/10.1016/S0009-2541(98)00075-8)
- Arnold, T., Zorn, T., Zänker, H., Bernhard, G., and Nitsche, H., 2001, Sorption behavior of U(VI) on phyllite: experiments and modeling: *Journal of Contaminant Hydrology*, v. 47, n. 2–4, p. 219–231, [http://dx.doi.org/10.1016/S0169-7722\(00\)00151-0](http://dx.doi.org/10.1016/S0169-7722(00)00151-0)
- Ault, A. K., Reiners, P. W., Prante, M. R., Evans, J. P., and Janecke, S. U., 2013, Dating brittle deformation and botryoidal hematite: A ^4He retentivity study: *Journal of Geophysical Research-Solid Earth*, v. 99, n. B9, p. 17695–17707, <http://dx.doi.org/10.1029/94JB01055>
- Barton, M. D., and Johnson, D. A., 1996, Evaporitic-source model for igneous-related Fe oxide-(REE-Cu-Au-U) mineralization: *Geology*, v. 24, n. 3, p. 259–262, [http://dx.doi.org/10.1130/0091-7613\(1996\)024<0259:ESMFIR>2.3.CO;2](http://dx.doi.org/10.1130/0091-7613(1996)024<0259:ESMFIR>2.3.CO;2)
- Bähr, R., Lippolt, H. J., and Wernicke, R. S., 1994, Temperature-induced ^4He degassing of specularite and botryoidal hematite: A ^4He retentivity study: *Journal of Geophysical Research-Solid Earth*, v. 99, n. B9, p. 17695–17707, <http://dx.doi.org/10.1029/94JB01055>
- Beratan, K. K., 1999, Miocene potassium metasomatism, Whipple Mountains, southeastern California: A datable tracer of extension-related fluid transport: *Geology*, v. 27, n. 3, p. 259–262, [http://dx.doi.org/10.1130/0091-7613\(1999\)027<0259:MPMWS>2.3.CO;2](http://dx.doi.org/10.1130/0091-7613(1999)027<0259:MPMWS>2.3.CO;2)
- Brady, R. J., 2002, Very high slip rates on continental extensional faults: new evidence from (U-Th)/He thermochronometry of the Buckskin Mountains, Arizona: *Earth and Planetary Science Letters*, v. 197, n. 1–2, p. 95–104, [http://dx.doi.org/10.1016/S0012-821X\(02\)00460-0](http://dx.doi.org/10.1016/S0012-821X(02)00460-0)
- Bryant, B., 1995, Geologic map, cross sections, isotopic dates, and mineral deposits of the Alamo Lake 30' x 60' quadrangle, west-central Arizona: U.S. Geological Survey Miscellaneous Investigations Series Map I-2489, scale 1:100,000.
- Bryant, B., and Wooden, J. L., 2008, Geology of the northern part of the Harcuvar complex, west-central Arizona: United States Geological Survey Professional Paper 1752, 52 p.
- Bryant, B., Naeser, C. W., and Fryxell, J. E., 1991, Implications of low-temperature cooling history on a transect across the Colorado Plateau-Basin and Range Boundary, west central Arizona: *Journal of Geophysical Research-Solid Earth*, v. 96, n. B7, p. 12375–12388, <http://dx.doi.org/10.1029/90JB02027>
- Cros, A., Gautheron, C., Pagel, M., Berthet, P., Tassan-Got, L., Douville, E., Pinna-Jamme, R., and Sarda, P., 2014, ^4He behavior in calcite filling viewed by (U-Th)/He dating, ^4He diffusion and crystallographic studies: *Geochimica et Cosmochimica Acta*, v. 125, p. 414–432, <http://dx.doi.org/10.1016/j.gca.2013.09.038>
- Danišik, M., Evans, N. J., Ramanaidou, E. R., McDonald, B. J., Mayers, C., and McInnes, B. I. A., 2013, (U-Th)/He chronology of the Robe River channel iron deposits, Hamersley Province, Western Australia: *Chemical Geology*, v. 354, p. 150–162, <http://dx.doi.org/10.1016/j.chemgeo.2013.06.012>
- Derby, S., ms, 2012, Depositional modes of manganese oxides at Artillery Peak, Mohave County, Arizona: Reno, Nevada, University of Nevada, M. S. thesis, 66 p.
- Dill, H. G., Hansen, B., Keck, E., and Weber, B., 2010, Cryptomelane: A tool to determine the age and the physical-chemical regime of a Plio-Pleistocene weathering zone in a granitic terrain (Hagendorf, SE Germany): *Geomorphology*, v. 121, n. 3–4, p. 370–377, <http://dx.doi.org/10.1016/j.geomorph.2010.05.004>
- Dodson, M. H., 1973, Closure temperature in cooling geochronological and petrological systems: Contributions to Mineralogy and Petrology, v. 40, n. 3, p. 259–274, <http://dx.doi.org/10.1007/BF00373790>
- Fanale, F. P., and Kulp, J. L., 1962, The helium method and the age of the Cornwall, Pennsylvania magnetite ore: *Economic Geology*, v. 57, n. 5, p. 735–746, <http://dx.doi.org/10.2113/gsecongeo.57.5.735>
- Farley, K. A., 2000, Helium diffusion from apatite: General behavior as illustrated by Durango fluorapatite: *Journal of Geophysical Research-Solid Earth*, v. 105, n. B2, p. 2903–2914, <http://dx.doi.org/10.1029/1999JB900348>
- Farley, K. A., and Flowers, R. M., 2012, (U-Th)/Ne and multidomain (U-Th)/He systematics of a hydrothermal hematite from eastern Grand Canyon: *Earth and Planetary Science Letters*, v. 359–360, p. 131–140, <http://dx.doi.org/10.1016/j.epsl.2012.10.010>
- Farley, K. A., Reiners, P. W., and Nenow, V., 1999, An apparatus for high-precision helium diffusion measurements from minerals: *Analytical Chemistry*, v. 71, n. 10, p. 2059–2061, <http://dx.doi.org/10.1021/ac9813078>
- Fechtig, H., and Kalbitzer, S., 1966, The Diffusion of Argon in Potassium-Bearing Solids, in Schaeffer, O. A., and Zahringer, J., editors, Potassium Argon Dating: Berlin, Springer, p. 68–107, http://dx.doi.org/10.1007/978-3-642-87895-4_4
- Flowers, R. M., Ketcham, R. A., Shuster, D. L., and Farley, K. A., 2009, Apatite (U-Th)/He thermochronometry using a radiation damage accumulation and annealing model: *Geochimica et Cosmochimica Acta*, v. 73, n. 8, p. 2347–2366, <http://dx.doi.org/10.1016/j.gca.2009.01.015>
- Foster, D. A., and John, B. E., 1999, Quantifying tectonic exhumation in an extensional orogen with thermochronology: examples from the southern Basin and Range Province in Ring, U., Brandon, M. T., Lister, G. S., and Willett, S. D., editors, Exhumation processes: normal faulting, ductile flow, and erosion: Geological Society, London, Special Publications, v. 154, p. 343–364, <http://dx.doi.org/10.1144/GSL.SP.1999.154.01.16>
- Foster, D. A., Gleadow, A. J. W., Reynolds, S. J., and Fitzgerald, P. G., 1993, Denudation of metamorphic core complexes and the reconstruction of the transition zone, west central Arizona: constraints from apatite fission track thermochronology: *Journal of Geophysical Research-Solid Earth*, v. 98, n. B2, p. 2167–2185, <http://dx.doi.org/10.1029/92JB02407>

- Frost, R. L., and Xi, Y., 2013, Is chrysocolla (Cu,Al)₂H₂Si₂O₅(OH)₄nH₂O related to spertiniite Cu(OH)₂?—A vibrational spectroscopic study: *Vibrational Spectroscopy*, v. 64, p. 33–38, <http://dx.doi.org/10.1016/j.vibspec.2012.10.001>
- Gallagher, K., Brown, R., and Johnson, C., 1998, Fission track analysis and its applications to geological problems: *Annual Reviews in Earth and Planetary Sciences*, v. 26, p. 519–572, <http://dx.doi.org/10.1146/annurev.earth.26.1.519>
- Giblin, A. M., Batts, B. D., and Swaine, D. J., 1981, Laboratory simulation studies of uranium mobility in natural waters: *Geochimica et Cosmochimica Acta*, v. 45, n. 5, p. 699–709, [http://dx.doi.org/10.1016/0016-7037\(81\)90043-0](http://dx.doi.org/10.1016/0016-7037(81)90043-0)
- Gourbet, L., Shuster, D. L., Balco, G., Cassata, W. S., Renne, P. R., and Rood, D., 2012, Neon diffusion kinetics in olivine, pyroxene, and feldspar: Retentivity of cosmogenic and nucleogenic neon: *Geochimica et Cosmochimica Acta*, v. 86, p. 21–36, <http://dx.doi.org/10.1016/j.gca.2012.03.002>
- Halfkenny, R. D., Kerrich, R., and Rehrig, W. A., 1989, Fluid regimes and geochemical mass transport in the development of mylonites and chloritic breccias at Copper Penny, Buckskin Mountains, in Spencer, J. E., and Reynolds, S. J., editors, *Geology and mineral resources of the Buckskin and Rawhide Mountains, west-central Arizona*: Arizona Geological Survey Bulletin 198, p. 190–212.
- Harrison, T. M., Duncan, I., and McDougall, I., 1985, Diffusion of ⁴⁰Ar in biotite: Temperature, pressure, and compositional effects: *Geochimica et Cosmochimica Acta*, v. 49, n. 11, p. 2461–2468, [http://dx.doi.org/10.1016/0016-7037\(85\)90246-7](http://dx.doi.org/10.1016/0016-7037(85)90246-7)
- Hautmann, S., and Lippolt, H. J., 2000, ⁴⁰Ar/³⁹Ar dating of central European K–Mn oxides—a chronological framework of supergene alteration processes during the Neogene: *Chemical Geology*, v. 170, n. 1–4, p. 37–80, [http://dx.doi.org/10.1016/S0009-2541\(99\)00241-7](http://dx.doi.org/10.1016/S0009-2541(99)00241-7)
- Heim, J. A., Vasconcelos, P. M., Shuster, D. L., Farley, K. A., and Broadbent, G., 2006, Dating paleochannel iron ore by (U-Th)/He analysis of supergene goethite, Hamersley province, Australia: *Geology*, v. 34, n. 3, p. 173–176, <http://dx.doi.org/10.1130/G22003.1>
- Hitzman, M. W., Oreskes, N., and Einaudi, M. T., 1992, Geological characteristics and tectonic setting of Proterozoic iron oxide (Cu-U-Au-REE) deposits: *Precambrian Research*, v. 58, n. 1–4, p. 241–287, [http://dx.doi.org/10.1016/0301-9268\(92\)90121-4](http://dx.doi.org/10.1016/0301-9268(92)90121-4)
- Hollocher, K., Spencer, J., and Ruiz, J., 1994, Composition changes in an ash-flow cooling unit during K metasomatism, west-central Arizona: *Economic Geology*, v. 89, n. 4, p. 877–888, <http://dx.doi.org/10.2113/gsecongeo.89.4.877>
- Howard, K. A., and John, B. E., 1987, Crustal extension along a rooted system of imbricate low-angle faults: Colorado River extensional corridor, California and Arizona, in Coward, M. P., Dewey, J. F., and Hancock, P. L., editors, *Continental Extension Tectonics*: Geological Society, London, Special Publications, v. 28, p. 299–311, <http://dx.doi.org/10.1144/GSL.SP.1987.028.01.19>
- Hsi, C-K. D., and Langmuir, D., 1985, Adsorption of uranyl onto ferric oxyhydroxides: Application of the surface complexation site-binding model: *Geochimica et Cosmochimica Acta*, v. 49, n. 9, p. 1931–1941, [http://dx.doi.org/10.1016/0016-7037\(85\)90088-2](http://dx.doi.org/10.1016/0016-7037(85)90088-2)
- Jambon, A., and Shelby, J. S., 1980, Helium diffusion and solubility in obsidians and basaltic glass in the range 200–300 °C: *Earth and Planetary Science Letters*, v. 51, n. 1, p. 206–214, [http://dx.doi.org/10.1016/0012-821X\(80\)90268-X](http://dx.doi.org/10.1016/0012-821X(80)90268-X)
- Ketcham, R. A., Gautheron, C., and Tassan-Got, L., 2011, Accounting for long alpha-particle stopping distances in (U-Th-Sm)/He geochronology: Refinement of the baseline case: *Geochimica et Cosmochimica Acta*, v. 75, n. 24, p. 7779–7791, <http://dx.doi.org/10.1016/j.gca.2011.10.011>
- Lamoreaux, R. H., Hildenbrand, D. L., and Brewer, L., 1987, High-Temperature Vaporization Behavior of Oxides II. Oxides of Be, Mg, Ca, Sr, Ba, B, Al, Ga, In, Tl, Si, Ge, Sn, Pb, Zn, Cd, and Hg: *Journal of Physical and Chemical Reference Data*, v. 16, n. 3, p. 419–443, <http://dx.doi.org/10.1063/1.555799>
- Larimer, J. W., and Anders, E., 1967, Chemical fractionations in meteorites—II. Abundance patterns and their interpretation: *Geochimica et Cosmochimica Acta*, v. 31, n. 8, p. 1239–1270, [http://dx.doi.org/10.1016/S0016-7037\(67\)80014-0](http://dx.doi.org/10.1016/S0016-7037(67)80014-0)
- Lasky, S. G., and Webber, B. N., 1944, Manganese deposits in the Artillery Mountains region, Mohave County, Arizona: *United States Geological Survey Bulletin* 936-R, p. 417–448
- 1949, Manganese resources of the Artillery Mountains region, Mohave County, Arizona: *United States Geological Survey Bulletin* 961, 86 p.
- Lehmann, N. E., and Spencer, J. E., 1989, Mineralization in the central part of the Planet mineral district, northwestern Buckskin Mountains, in Spencer, J. E., and Reynolds, S. J., editors, *Geology and mineral resources of the Buckskin and Rawhide Mountains, west-central Arizona*: Arizona Geological Survey Bulletin 198, p. 215–222.
- Lippolt, H. J., and Hautmann, S., 1995, ⁴⁰Ar/³⁹Ar ages of Precambrian manganese ore minerals from Sweden, India and Morocco: *Mineralium Deposita*, v. 30, n. 3–4, p. 246–256, <http://dx.doi.org/10.1007/BF00196360>
- Lippolt, H. J., Wernicke, R. S., and Boschmann, W., 1993, ⁴He diffusion in specular hematite: Physics and Chemistry of Minerals, v. 20, n. 6, p. 415–418, <http://dx.doi.org/10.1007/BF00203111>
- Lippolt, H. J., Wernicke, R. S., and Bahr, R., 1995, Paragenetic specularite and adularia (Elba, Italy): Concordant (U + Th)-He and K-Ar ages: *Earth and Planetary Science Letters*, v. 132, n. 1–4, p. 43–51, [http://dx.doi.org/10.1016/0012-821X\(95\)00046-F](http://dx.doi.org/10.1016/0012-821X(95)00046-F)
- Lodders, K., 2003, Solar system abundances and condensation temperatures of the elements: *Astrophysical Journal*, v. 591, n. 2, p. 1220–1247, <http://dx.doi.org/10.1086/375492>
- Lovera, O. M., Grove, M., Harrison, T. M., and Mahon, K. I., 1997, Systematic analysis of K-feldspar step heating results: I. Significance of activation energy determinations: *Geochimica et Cosmochimica Acta*, v. 61, n. 15, p. 3171–3192, [http://dx.doi.org/10.1016/S0016-7037\(97\)00147-6](http://dx.doi.org/10.1016/S0016-7037(97)00147-6)

- Lucchitta, I., and Suneson, N. H., 1993, Stratigraphic section of the Castaneda Hills-Signal area, Arizona, in Sherrod, D. R., and Nielson, J. E., editors, Tertiary stratigraphy of highly extended terranes, California, Arizona, and Nevada: United States Geological Survey Bulletin 2053, p. 139–144.
- Michalski, J. R., Reynolds, S. J., Niles, P. B., Sharp, T. G., and Christensen, P. R., 2007, Alteration mineralogy in detachment zones: Insights from Swansea, Arizona: *Geosphere*, v. 3, n. 4, p. 184–198, <http://dx.doi.org/10.1130/GES00080.1>
- Mouat, M. M., 1962, Manganese oxides from the Artillery Mountains area, Arizona: *American Mineralogist*, v. 47, n. 5–6, p. 744–757.
- Murray, K. E., Orme, D. A., and Reiners, P. W., 2014, Effects of U-Th-rich grain boundary phases on apatite helium ages: *Chemical Geology*, v. 390, p. 135–151, <http://dx.doi.org/10.1016/j.chemgeo.2014.09.023>
- Nielson, J. E., and Beratan, K. K., 1995, Stratigraphic and structural synthesis of a Miocene extensional terrane, southeast California and west-central Arizona: *Geological Society of America Bulletin*, v. 107, n. 2, p. 241–252, [http://dx.doi.org/10.1130/0016-7606\(1995\)107<0241:SASSOA>2.3.CO;2](http://dx.doi.org/10.1130/0016-7606(1995)107<0241:SASSOA>2.3.CO;2)
- Orme, D. A., ms, 2011, Effects of external parent nuclides on apatite helium dates: Tucson, Arizona, University of Arizona, M. S. thesis, 39 p.
- Pidgeon, R. T., Brander, T., and Lippolt, H. J., 2004, Late Miocene (U+Th)-⁴He ages of ferruginous nodules from lateritic duricrust, Darling Range, Western Australia: *Australian Journal of Earth Sciences*, v. 51, n. 6, p. 901–909, <http://dx.doi.org/10.1111/j.1400-0952.2004.01094.x>
- Post, J. E., 1999, Manganese oxide minerals: Crystal structures and economic and environmental significance: *Proceedings of the National Academy of Sciences of the United States of America*, v. 96, n. 7, p. 3447–3454, <http://dx.doi.org/10.1073/pnas.96.7.3447>
- Rahn, M. K., Brandon, M. T., Batt, G. E., and Garver, J. I., 2004, A zero-damage model for fission-track annealing in zircon: *American Mineralogist*, v. 89, n. 4, p. 473–484.
- Reiners, P. W., 2005, Zircon (U-Th)/He thermochronometry, in Reiners, P. W., and Ehlers, T. A., editors, Low-temperature thermochronology: techniques, interpretations, and applications: *Reviews in Mineralogy and Geochemistry*, v. 58, p. 151–179, <http://dx.doi.org/10.2138/rmg.2005.58.6>
- Reiners, P. W., and Farley, K. A., 1999, Helium diffusion and (U-Th)/He thermochronometry of titanite: *Geochimica et Cosmochimica Acta*, v. 63, n. 22, p. 3845–3859, [http://dx.doi.org/10.1016/S0016-7037\(99\)00170-2](http://dx.doi.org/10.1016/S0016-7037(99)00170-2)
- Reiners, P. W., Chan, M. A., and Evenson, N. S., 2014, (U-Th)/He geochronology and Chemical compositions of diagenetic cement, concretions, and fracture-filling Oxide minerals in Mesozoic sandstones of the Colorado Plateau: *Geological Society of America Bulletin*, v. 126, n. 9–10, p. 1363–1383, <http://dx.doi.org/10.1130/B30983.1>
- Richard, S. M., Fryxell, J. E., and Sutter, J. F., 1990, Tertiary structure and thermal history of the Harquahala and Buckskin Mountains, west central Arizona: Implications for denudation by a major detachment fault system: *Journal of Geophysical Research-Solid Earth*, v. 95, n. B12, p. 19973–19987, <http://dx.doi.org/10.1029/JB095iB12p19973>
- Roddy, M. S., Reynolds, S. J., Smith, B. M., and Ruiz, J., 1988, K-metasomatism and detachment-related mineralization, Harcuvar Mountains, Arizona: *Geological Society of America Bulletin*, v. 100, n. 10, p. 1627–1639, [http://dx.doi.org/10.1130/0016-7606\(1988\)100<1627:KMADRM>2.3.CO;2](http://dx.doi.org/10.1130/0016-7606(1988)100<1627:KMADRM>2.3.CO;2)
- Schulling, W. T., ms, 1978, The environment of formation of Cu+Ag-bearing calcite veins, Sacramento Mountains, California: Tucson, Arizona, University of Arizona, M. S. thesis, 60 p.
- Scott, R. J., Foster, D. A., and Lister, G. S., 1998, Tectonic implications of rapid cooling of lower plate rocks from the Buckskin-Rawhide metamorphic core complex, west-central Arizona: *Geological Society of America Bulletin*, v. 110, n. 5, p. 588–614, [http://dx.doi.org/10.1130/0016-7606\(1998\)110<0588:TIORCO>2.3.CO;2](http://dx.doi.org/10.1130/0016-7606(1998)110<0588:TIORCO>2.3.CO;2)
- Shackelford, T. J., 1980, Tertiary tectonic denudation of a Mesozoic–early Tertiary(?) gneiss complex, Rawhide Mountains, western Arizona: *Geology*, v. 8, n. 4, p. 190–194, [http://dx.doi.org/10.1130/0091-7613\(1980\)8<190:TTDOAM>2.0.CO;2](http://dx.doi.org/10.1130/0091-7613(1980)8<190:TTDOAM>2.0.CO;2)
- Shafiqullah, M., Damon, P. E., Lynch, D. J., Reynolds, S. J., Rehrig, W. A., and Raymond, R. H., 1980, K-Ar geochronology and geologic history of southwestern Arizona and adjacent areas, in Jenney, J. P., and Stone, C., editors, *Studies in western Arizona*: Arizona Geological Society Bulletin, v. 12, p. 201–260.
- Shelby, J. E., 1972, Helium migration in glass-forming oxides: *Journal of Applied Physics*, v. 43, n. 7, p. 3068–3072, <http://dx.doi.org/10.1063/1.1661661>
- Shuibo, X., Chun, Z., Xinghuo, Z., Jing, Y., Xiaojian, Z., and Jingsong, W., 2009, Removal of uranium (VI) from aqueous solution by adsorption of hematite: *Journal of Environmental Radioactivity*, v. 100, n. 2, p. 162–166, <http://dx.doi.org/10.1016/j.jenvrad.2008.09.008>
- Shuster, D. L., and Farley, K. A., 2004, ⁴He/³He thermochronometry: Earth and Planetary Science Letters, v. 217, n. 1–2, p. 1–17, [http://dx.doi.org/10.1016/S0012-821X\(03\)00595-8](http://dx.doi.org/10.1016/S0012-821X(03)00595-8)
- 2005a, ⁴He/³He thermochronometry: Theory, practice, and potential complications, in Reiners, P. W., and Ehlers, T. A., editors, *Low-temperature Thermochronology: Techniques, Interpretations, and Applications: Reviews in Mineralogy and Geochemistry*, v. 58, p. 181–203, <http://dx.doi.org/10.2138/rmg.2005.58.7>
- 2005b, Diffusion kinetics of proton-induced ²¹Ne, ³He, and ⁴He in quartz: *Geochimica et Cosmochimica Acta*, v. 69, n. 9, p. 2349–2359, <http://dx.doi.org/10.1016/j.gca.2004.11.002>
- Shuster, D. L., Vasconcelos, P. M., Heim, J. A., and Farley, K. A., 2005, Weathering geochronology by (U-Th)/He dating of goethite: *Geochimica et Cosmochimica Acta*, v. 69, n. 3, p. 659–673, <http://dx.doi.org/10.1016/j.gca.2004.07.028>
- Singer, D. M., Maher, K., and Brown, G. E., Jr., 2009, Uranyl–chlorite sorption/desorption: Evaluation of different U(VI) sequestration processes: *Geochimica et Cosmochimica Acta*, v. 73, n. 20, p. 5989–6007, <http://dx.doi.org/10.1016/j.gca.2009.07.002>
- Singleton, J. S., and Mosher, S., 2012, Mylonitization in the lower plate of the Buckskin-Rawhide detachment

- fault, west-central Arizona: Implications for the geometric evolution of metamorphic core complexes: *Journal of Structural Geology*, v. 39, p. 180–198, <http://dx.doi.org/10.1016/j.jsg.2012.02.013>
- Singleton, J. S., and Stockli, D., 2013, Timing, rate, and magnitude of slip on the Buckskin-Rawhide detachment fault, west-central Arizona: *Geological Society of America Abstracts with Programs*, v. 45, n. 7, p. 224.
- Spencer, J. E., 1984, Role of tectonic denudation in warping and uplift of low-angle normal faults: *Geology*, v. 12, n. 2, p. 95–98, [http://dx.doi.org/10.1130/0091-7613\(1984\)12<95:ROTDIW>2.0.CO;2](http://dx.doi.org/10.1130/0091-7613(1984)12<95:ROTDIW>2.0.CO;2)
- 1991, The Artillery Manganese District in West-Central Arizona: *Arizona Geology*, v. 21, n. 3, p. 9–12.
- Spencer, J. E., and Reynolds, S. J., 1989, Tertiary structure, stratigraphy, and tectonics of the Buckskin Mountains, in Spencer, J. E., and Reynolds, S. J., editors, *Geology and mineral resources of the Buckskin and Rawhide Mountains, west-central Arizona*: *Arizona Geological Survey Bulletin* 198, p. 103–167.
- 1991, Tectonics of Mid-Tertiary extension along a transect through west central Arizona: *Tectonics*, v. 10, n. 6, p. 1204–1221, <http://dx.doi.org/10.1029/91TC01160>
- Spencer, J. E., and Welty, J. W., 1986, Possible controls of base- and precious-metal mineralization associated with Tertiary detachment faults in the lower Colorado River trough, Arizona and California: *Geology*, v. 14, n. 3, p. 195–198, [http://dx.doi.org/10.1130/0091-7613\(1986\)14<195:PCOBAP>2.0.CO;2](http://dx.doi.org/10.1130/0091-7613(1986)14<195:PCOBAP>2.0.CO;2)
- Spencer, J. E., and Welty, J. W., 1989, Geology of mineral deposits in the Buckskin and Rawhide Mountains, in Spencer, J. E., and Reynolds, S. J., editors, *Geology and mineral resources of the Buckskin and Rawhide Mountains, west-central Arizona*: *Arizona Geological Survey Bulletin* 198, p. 223–254.
- Spencer, J. E., Shafiqullah, M., Miller, R. J., and Pickthorn, L. G., 1989a, K-Ar geochronology of Miocene extension, volcanism and potassium metasomatism in the Buckskin and Rawhide Mountains, in Spencer, J. E., and Reynolds, S. J., editors, *Geology and mineral resources of the Buckskin and Rawhide Mountains, west-central Arizona*: *Arizona Geological Survey Bulletin* 198, p. 184–189.
- Spencer, J. E., Grubensky, M. J., Duncan, J. T., and Shenk, J. D., 1989b, Geology and mineral deposits of the central Artillery Mountains, in Spencer, J. E., and Reynolds, S. J., editors, *Geology and mineral resources of the Buckskin and Rawhide Mountains, west-central Arizona*: *Arizona Geological Survey Bulletin* 198, p. 168–183.
- Spencer, J. E., Richard, S. M., Reynolds, S. J., Miller, R. J., Shafiqullah, M., Grubensky, M. J., and Gilbert, W. G., 1995, Spatial and temporal relationships between mid-Tertiary magmatism and extension in southwestern Arizona: *Journal of Geophysical Research*, v. 100, n. B6, p. 10321–10351, <http://dx.doi.org/10.1029/94JB02817>
- Spencer, J. E., Richard, S. M., Johnson, B. J., Love, D. S., Pearthree, P. A., and Reynolds, S. J., 2013, Geologic map of the Artillery Peak and Rawhide Wash 7 ½' Quadrangles, Mohave and La Paz Counties, Arizona: *Arizona Geological Survey Digital Geologic Map DGM-100*, scale 1:24,000.
- Strutt, R. J., 1908, On the accumulation of helium in geological time: *Proceedings of the Royal Society of London A*, v. 80, n. 547, p. 272–277, <http://dx.doi.org/10.1098/rspa.1908.0079>
- Suneson, N. H., and Lucchitta, I., 1983, Origin of bimodal volcanism, southern Basin and Range province, west-central Arizona: *Geological Society of America Bulletin*, v. 94, n. 8, p. 1005–1019, [http://dx.doi.org/10.1130/0016-7606\(1983\)94<1005:OOBVSB>2.0.CO;2](http://dx.doi.org/10.1130/0016-7606(1983)94<1005:OOBVSB>2.0.CO;2)
- Vasconcelos, P. M., 1999, K-Ar and ⁴⁰Ar/³⁹Ar geochronology of weathering processes: *Annual Review of Earth and Planetary Sciences*, v. 27, p. 183–229, <http://dx.doi.org/10.1146/annurev.earth.27.1.183>
- Vasconcelos, P. M., Becker, T. A., Renne, P. R., and Brimhall, G. H., 1992, Age and Duration of Weathering by ⁴⁰K-⁴⁰Ar and ⁴⁰Ar/³⁹Ar Analysis of Potassium-Manganese Oxides: *Science*, v. 258, n. 5081, p. 451–454, <http://dx.doi.org/10.1126/science.258.5081.451>
- Vasconcelos, P. M., Heim, J. A., Farley, K. A., Monteiro, H., and Waltenberg, K., 2013, ⁴⁰Ar/³⁹Ar and (U-Th)/He – ⁴He/³He geochronology of landscape evolution and channel iron deposit genesis at Lynn Peak, Western Australia: *Geochimica et Cosmochimica Acta*, v. 117, p. 283–312, <http://dx.doi.org/10.1016/j.gca.2013.03.037>
- Waltenberg, K. M., ms, 2012, Mineral physics and crystal chemistry of minerals suitable for weathering geochronology: implications to ⁴⁰Ar/³⁹Ar and (U-Th)/He geochronology: Brisbane, Australia, University of Queensland, Ph. D. thesis, 164 p.
- Wernicke, R. S., and Lippolt, H. J., 1993, Botryoidal hematite from the Schwarzwald (Germany): heterogeneous uranium distributions and their bearing on the helium dating method: *Earth and Planetary Science Letters*, v. 114, n. 2–3, p. 287–300, [http://dx.doi.org/10.1016/0012-821X\(93\)90031-4](http://dx.doi.org/10.1016/0012-821X(93)90031-4)
- 1994a, Dating of vein specularite using internal (U+Th)/⁴He isochrons: *Geophysical Research Letters*, v. 21, n. 5, p. 345–347, <http://dx.doi.org/10.1029/94GL00014>
- 1994b, ⁴He age discordance and release behavior of a double shell botryoidal hematite from the Schwarzwald, Germany: *Geochimica et Cosmochimica Acta*, v. 58, n. 1, p. 421–429, [http://dx.doi.org/10.1016/0016-7037\(94\)90474-X](http://dx.doi.org/10.1016/0016-7037(94)90474-X)
- 1997a, Evidence of Mesozoic multiple hydrothermal activity in the basement at Nonnenmattweiher (southern Schwarzwald), Germany: *Mineralium Deposita*, v. 32, n. 2, p. 197–200, <http://dx.doi.org/10.1007/s001260050085>
- 1997b, (U+Th)-He evidence of Jurassic continuous hydrothermal activity in the Schwarzwald basement, Germany: *Chemical Geology*, v. 138, n. 3–4, p. 273–285, [http://dx.doi.org/10.1016/S0009-2541\(97\)00020-X](http://dx.doi.org/10.1016/S0009-2541(97)00020-X)
- Wilkins, J., and Heidrick, T. L., 1982, Base and precious metal mineralization related to low-angle tectonic features in the Whipple Mountains, California and Buckskin Mountains, Arizona, in Frost, E. G., and Martin, D. L., editors, *Mesozoic-Cenozoic tectonic evolution of the Colorado River region, California, Arizona, and Nevada*: San Diego, California, Cordilleran Publishers, p. 182–203.

- Wilkins, J., Beane, R. E., and Heidrick, T. L., 1986, Mineralization related to detachment faults: a model, *in* Beatty, B., and Wilkinson, P. A. K., editors, *Frontiers in geology and ore deposits of Arizona and the southwest: Arizona Geological Society Digest*, v. 16, p. 108–117.
- Yapp, C. J., and Shuster, D. L., 2011, Environmental memory and a possible seasonal bias in the stable isotope composition of (U–Th)/He-dated goethite from the Canadian Arctic: *Geochimica et Cosmochimica Acta*, v. 75, n. 15, p. 4194–4215, <http://dx.doi.org/10.1016/j.gca.2011.04.029>
- Yarnold, J. C., 1994, Tertiary sedimentary rocks associated with the Harcuvar core complex in Arizona (U.S.A.): insights into paleogeographic evolution during displacement along a major detachment fault system: *Sedimentary Geology*, v. 89, n. 1–2, p. 43–63, [http://dx.doi.org/10.1016/0037-0738\(94\)90083-3](http://dx.doi.org/10.1016/0037-0738(94)90083-3)